AN INVESTIGATION INTO THE DESIGN AND CONTROL OF TUNABLE PIEZOELECTRIC RESONATORS

by

Muturi G. Muriuki

BS, Hope College, 1997

MS, University of Pittsburgh, 2000

Submitted to the Graduate Faculty

of the School of Engineering

in partial fulfillment of

the requirements for the degree of

Doctor of Philosophy

University of Pittsburgh

2004

UNIVERSITY OF PITTSBURGH

SCHOOL OF ENGINEERING

This dissertation was presented

by

Muturi G. Muriuki

It was defended on

July 27, 2004

and approved by

Dr James T. Cain, Professor, Electrical Engineering

Dr Marlin H. Mickle, Professor, Electrical Engineering

Dr Qing-Ming Wang, Assistant Professor, Mechanical Engineering

Dr Jeffrey S. Vipperman, Assistant Professor, Mechanical Engineering

Dissertation Director: Dr William W. Clark, Associate Professor, Mechanical Engineering

AN INVESTIGATION INTO THE DESIGN AND CONTROL OF TUNABLE PIEZOELECTRIC RESONATORS

Muturi G. Muriuki, PhD

University of Pittsburgh, 2004

Piezoelectric resonators are used in electronic devices and electrical circuits as a frequency source. The most commonly used material for the piezoelectric resonators is quartz. The quartz resonator has a tunability of between 10 ppm (0.001%) and 100 ppm (0.01%) of the nominal frequency of operation. This work shows that greater tunability can be achieved using resonators made using piezoelectric materials other than quartz and a shunt-tuning technique. The tuning afforded by using lead zirconate titanate as the piezoelectric material in a cantilever type resonator is explored in detail from an analytical and experimental standpoint. It is shown that this tuning can be up to over 10,000 ppm (1%) of the nominal operational frequency in the configuration looked at, which was not optimized to maximize the tuning range. Questions of implementation of the resonator in a commonly used resonator circuit were also answered. The resonator was experimentally shown to be operable in a modified Pierce circuit with a tuning range that was analytically predicted.

TABLE OF CONTENTS

1.0 INTRODUCTION 1

1.1 RESONATORS 2

1.1.1 Resonator Techniques 4

1.2 OBJECTIVES OF THE WORK 7

2.0 PIEZOELECTRICITY 10

2.1 THE PIEZOELECTRIC EFFECT 10

2.2 PIEZOELECTRIC MATERIALS 10

2.2.1 Crystalline Piezoelectric Materials 10

2.2.1.1 Quartz 10

2.2.1.2 Rochelle Salt 13

2.2.1.3 Tourmaline 13

2.2.1.4 Gallium Orthophosphate 14

2.2.1.5 The CGG Group 15

2.2.1.6 Lithium Niobate and Lithium Tantalate 16

2.2.1.7 Other single crystal compounds 17

2.2.2 Non-crystalline Piezoelectric Materials 18

2.2.2.1 Barium Titanate 19

2.2.2.2 Bismuth Titanate family 19

2.2.2.3 Tungsten Bronze family 19

2.2.2.4 Perovskite Layer Structure Ferroelectrics 20

2.2.2.5 Lead Zirconate Titanate (PZT) 20

2.2.2.6 Aluminum Nitride 22

2.2.2.7 Zinc Oxide 22

2.2.2.8 PVDF 22

2.3 PIEZOELECTRIC SYSTEMS, CLASSES AND MATERIAL STRAINS 23

2.3.1 Piezoelectric Systems and Classes 23

2.3.1.1 Orthorhombic System 25

2.3.1.2 Tetragonal System 25

2.3.1.3 Trigonal System 26

2.3.1.4 Hexagonal System 27

2.3.1.5 Cubic System 27

2.3.2 Piezoelectric Strain Matrices and Induced Strains 27

3.0 RESONATORS AND OSCILLATORS AND THEIR CHARACTERISTICS 29

3.1 RESONATOR CHARACTERISTICS 29

3.1.1 Q 29

3.1.2 Stability 30

3.1.2.1 Jitter 30

3.1.2.2 Drift and Aging 30

3.1.2.3 Temperature Stability 31

3.2 TYPES OF RESONATORS AND OSCILLATORS 32

3.2.1 Crystal Resonators and Oscillators 32

3.2.2 Atomic Resonators and Oscillators 33

3.2.3 Microwave Resonators and Oscillators 34

3.2.4 Electrical Circuits 35

3.2.5 Mechanical and Electromechanical Resonators and Oscillators 35

3.3 MODES OF RESONANCE OR OSCILLATION 37

3.3.1 Bulk Acoustic Waves (BAW) 37

3.3.2 Surface Acoustic Waves (SAW) 38

3.3.3 Direct Electrical Coupling 38

3.3.3.1 Microwave Cavity Modes 39

3.3.3.2 Microstrip Lines 39

3.3.4 Mechanical Vibration 40

3.3.4.1 Transverse Vibration 40

3.3.4.2 Torsional Vibration 41

3.3.4.3 Axial Vibration 41

3.3.4.4 Membrane Vibration 42

3.3.4.5 Plate Vibration 42

4.0 DESIGN AND MODELING 43

4.1 DESIGN 44

4.2 MODELING OF THE DESIGNS 47

4.2.1 One Degree of Freedom Systems 47

4.2.1.1 Simple Model from the Beam Equation 47

4.2.1.2 Shape Functions applied to the Hamiltonian of the Electromechanical System 50

5.0 BENDING FREQUENCIES OF VIBRATION 55

5.1 ANALYTICAL MODEL 55

5.2 EXPERIMENTAL SETUP 57

5.3 COMPARISON OF ANALYTICAL AND EXPERIMENTAL RESULTS 58

5.4 SUMMARY 64

6.0 TUNING RANGE 65

6.1 ANALYTICAL MODEL 65

6.2 EXPERIMENTAL SETUP 70

6.3 COMPARISON OF ANALYTICAL AND EXPERIMENTAL RESULTS 71

6.4 SUMMARY 85

7.0 FEEDBACK GAIN 87

7.1 ANALYTICAL MODEL 87

7.2 RESULTS 90

7.3 SUMMARY 98

8.0 REACTANCE AND RESONATOR OPERATING FREQUENCIES 99

8.1 ANALYTICAL MODEL 100

8.2 EXPERIMENTAL SETUP 102

8.3 COMPARISON OF ANALYTICAL AND EXPERIMENTAL RESULTS 107

8.3.1 Resonator PS VIII 107

8.3.2 Resonator PS XII 113

8.3.3 Resonator PS XIII 118

8.3.4 Resonator PS XIV 122

8.3.5 Resonator PS XV 128

8.3.6 Resonator PS XVI 134

8.4 SUMMARY 144

9.0 CONCLUSIONS AND FUTURE WORK 145

9.1 CONCLUSIONS …………………………………………………………………….. 145

9.2 FUTURE WORK ..………………………………………………………………… 148

BIBLIOGRAPHY ……………..……………………………………………………………….. 150

LIST OF TABLES

Table 1 Piezoelectric Properties of some single crystals of the CGG group 16

Table 2. Applied charges and induced strains 16

Table 3. Table of material properties used in the model 59

Table 4. Frequency of vibration from MathCAD 59

Table 5. Experimental and analytical bending mode frequencies 61

Table 6. Theoretical tuning ranges from analytical model 71

Table 7. Comparison of tuning range from SigLab and analytical data 72

Table 8. Resonator PS VIII inverter driven tuning and operating frequencies in kHz 108

Table 9. Resonator PS XII inverter driven tuning and operating frequencies in kHz 113

Table 10. Resonator PS XIII inverter driven tuning and operating frequencies in kHz 119

Table 11. Resonator PS XIV inverter driven tuning and operating frequencies in kHz 123

Table 12. Resonator PS XV inverter driven tuning and operating frequencies in kHz 129

Table 13. Resonator PS XVI inverter driven tuning and operating frequencies in kHz, run 1 .. 135

Table 14. Resonator PS XVI inverter driven tuning and operating frequencies in kHz, run 2 .. 136

Table 15. Comparison of tuning range from Pierce circuit operation and analytical data 147

Table 16. Comparison of tuning range from operation with circuit with separate gain and phase adjustment, and analytical data 148

LIST OF FIGURES

Figure 1. Simplified quartz crystal circuit diagram ……………………………………………………... 5

Figure 2. Butterworth-VanDyke equivalent circuit for crystal resonators ……………………….. 6

Figure 3. Simplified piezoelectric resonator circuit ………………………………………………. 6

Figure 4. Crystal with crystallographic axes indicated …………………………………….…… 11

Figure 5. Q Factor ……………………………………………………………………………….…... 30

Figure 6. Examples of shear, flexure and extensional vibration modes ……………………..……. 33

Figure 7. The basic electrical resonant circuit ……………………………………..…………...… 35

Figure 8. Microstrip Line Oscillator - Ring Type ……………………………...………..…...…… 40

Figure 9. Plan view of the layout of the resonator ……….……………………………...……… 45

Figure 10. Side view of the layout of the resonator ……………………………………….……... 46

Figure 11. Width transformation in calculation of the centroid ………………………….…….. 49

Figure 12. Frequency response measurement experimental setup ……………………………..…. 57

Figure 13. First five displacement mode shapes ……………………………………………..…… 58

Figure 14. Frequency response for beams PS XII and PS XVI to 10kHz ……………………..…… 60

Figure 15. Frequency response to 10kHz for PS VIII, PS XII and PS XIII ………………….…….. 61

Figure 16. Frequency response from 10 to 20kHz for PS VIII, PS XII and PS XIII ………….……. 62

Figure 17. Frequency response to 10kHz for PS XIV, PS XV and PS XVI ……………………..….. 63

Figure 18. Frequency response from 10 to 20kHz for PS XIV, PS XV and PS XVI …………...…... 63

Figure 19. Parallel stiffnesses in the resonator …………………………………………………..... 66

Figure 20. Electrical shunting of the passive layer capacitance ... 67

Figure 21. Tuning range measurement experimental setup ... 70

Figure 22. Changes in frequency response near mode 1, PS XVI ... 73

Figure 23. Changes in frequency response near mode 2, PS XVI ... 73

Figure 24. Changes in frequency response near mode 3, PS XVI ... 74

Figure 25. Changes in frequency response near mode 4, PS XVI ... 75

Figure 26. Changes in frequency response near mode 5, PS XVI ... 75

Figure 27. Changes in frequency near modes 1 and 2, PS VIII ... 76

Figure 28. Changes in frequency near mode 3, PS VIII ... 77

Figure 29. Changes in frequency near modes 4 and 5, PS VIII ... 77

Figure 30. Changes in frequency near modes 1 and 2, PS XII ... 78

Figure 31. Changes in frequency near modes 3 and 4, PS XII ... 78

Figure 32. Changes in frequency near mode 5, PS XII ... 79

Figure 33. Changes in frequency near modes 1 and 2, PS XIII ... 80

Figure 34. Changes in frequency near modes 3 and 4, PS XIII ... 80

Figure 35. Changes in frequency near mode 5, PS XIII ... 81

Figure 36. Changes in frequency near modes 1 and 2, PS XIV ... 81

Figure 37. Changes in frequency near modes 3 and 4, PS XIV ... 82

Figure 38. Changes in frequency near mode 5, PS XIV ... 82

Figure 39. Changes in frequency near modes 1 and 2, PS XV ... 84

Figure 40. Changes in frequency near modes 3 and 4, PS XV ... 84

Figure 41. Changes in frequency near mode 5, PS XV ... 85

Figure 42. Changes in frequency near mode 2, PS VIII ... 86

Figure 43. Gain for bending mode 1 versus sensor and actuator dimensions ... 91

Figure 44. θ^A as a function of actuator length for bending mode 1 92

Figure 45. Gain for bending mode 2 versus sensor and actuator dimensions 93

Figure 46. θ^A as a function of actuator length for bending mode 2 94

Figure 47. Gain for bending mode 3 versus sensor and actuator dimensions 94

Figure 48. θ^A as a function of actuator length for bending mode 3 95

Figure 49. Gain for bending mode 4 versus sensor and actuator dimensions 95

Figure 50. θ^A as a function of actuator length for bending mode 4 96

Figure 51. Gain for bending mode 5 versus sensor and actuator dimensions 96

Figure 52. θ^A as a function of actuator length for bending mode 5 97

Figure 53. Pierce oscillator circuit configuration 101

Figure 54. Resonance and anti-resonance frequency points 102

Figure 55. Impedance analysis experimental setup 103

Figure 56. Operational frequency experimental setup 104

Figure 57. Electrical circuit with separate gain and phase adjustment 105

Figure 58. Circuit diagram of the gain and phase adjustable amplifier 105

Figure 59. The modified Pierce circuit 106

Figure 60. Circuit diagram of the variant of the Pierce circuit used in the experiments 106

Figure 61. Resistance and Reactance, resonator PS VIII with 4.7mH series inductor 109

Figure 62. Resistance and Reactance, resonator PS VIII with 9.4mH series inductor 109

Figure 63. Resistance and Reactance, resonator PS VIII with 82mH series inductor 110

Figure 64. R and X, full range, resonator PS VIII with 4.7mH series inductor 111

Figure 65. R and X, full range, resonator PS VIII with 9.4mH series inductor 111

Figure 66. R and X, full range, resonator PS VIII with 82mH series inductor 113

Figure 67. Resistance and Reactance, resonator PS XII with 1mH series inductor …………… 114

Figure 68. Resistance and Reactance, resonator PS XII with 2mH series inductor …………… 115

Figure 69. Resistance and Reactance, resonator PS XII with 4.7mH series inductor …………. 116

Figure 70. Resistance and Reactance, resonator PS XII with 9.4mH series inductor …………. 116

Figure 71. R and X, full range, resonator PS XII with 2mH series inductor …………………… 117

Figure 72. R and X, full range, resonator PS XII with 4.7mH series inductor …………………. 117

Figure 73. R and X, full range, resonator PS XII with 9.4mH series inductor …………………. 118

Figure 74. Resistance and Reactance, resonator PS XIII with 1mH series inductor …………... 120

Figure 75. Resistance and Reactance, resonator PS XIII with 2mH series inductor …………... 120

Figure 76. R and X, full range, resonator PS XIII with 1mH series inductor ………………….. 121

Figure 77. R and X, full range, resonator PS XIII with 2mH series inductor …………………... 122

Figure 78. Resistance and Reactance, resonator PS XIV with 1mH series inductor …………... 124

Figure 79. Resistance and Reactance, resonator PS XIV with 2mH series inductor …………... 124

Figure 80. Resistance and Reactance, resonator PS XIV with 4.7mH series inductor ………… 125

Figure 81. Resistance and Reactance, resonator PS XIV with 9.4mH series inductor ………… 125

Figure 82. R and X, full range, resonator PS XIV with 1mH series inductor ………………….. 126

Figure 83. R and X, full range, resonator PS XIV with 2mH series inductor ………………….. 127

Figure 84. R and X, full range, resonator PS XIV with 4.7mH series inductor ………………… 127

Figure 85. R and X, full range, resonator PS XIV with 9.4mH series inductor ………………… 128

Figure 86. Resistance and Reactance, resonator PS XV with 1mH series inductor ………….…… 130

Figure 87. Resistance and Reactance, resonator PS XV with 2mH series inductor ………….…… 130

Figure 88. Resistance and Reactance, resonator PS XV with 4.7mH series inductor ………….…. 131

Figure 89. Resistance and Reactance, resonator PS XV with 9.4mH series inductor ………….…. 131

Figure 90. R and X, 5kHz to 100kHz, resonator PS XV with a 1mH series inductor ………….…. 132

Figure 91. R and X, 100kHz to 320kHz, resonator PS XV with a 1mH series inductor ………. 132

Figure 92. R and X, full range, resonator PS XV with 2mH series inductor …………………… 133

Figure 93. R and X, full range, resonator PS XV with 4.7mH series inductor …………………. 133

Figure 94. R and X, full range, resonator PS XV with 9.4mH series inductor …………………. 134

Figure 95. Resistance and Reactance, resonator PS XVI with 1mH series inductor …………..….. 137

Figure 96. Resistance and Reactance, resonator PS XVI with 2mH series inductor …………... 137

Figure 97. Resistance and Reactance, resonator PS XVI with 4.7mH series inductor ………… 138

Figure 98. Resistance and Reactance, resonator PS XVI with 9.4mH series inductor ………… 139

Figure 99. Resistance and Reactance, resonator PS XVI with 14.1mH series inductor ……….. 140

Figure 100. Resistance and Reactance, resonator PS XVI with 82mH series inductor ……..…. 140

Figure 101. R and X, full range, resonator PS XVI with 1mH series inductor ……………...….. 141

Figure 102. R and X, full range, resonator PS XVI with 2mH series inductor …………………. 141

Figure 103. R and X, full range, resonator PS XVI with 4.7mH series inductor ……………..…. 142

Figure 104. R and X, full range, resonator PS XVI with 9.4mH series inductor ………..………. 142

Figure 105. R and X, full range, resonator PS XVI with 82mH series inductor ………….…….. 143

NOMENCLATURE

Matrices:

B_f	Force input matrix
B_q	Charge input matrix
c^E	Constant electric field mechanical stiffness
c^S	Constant mechanical strain mechanical stiffness
C_p	Piezoelectric capacitance
d	Piezoelectric strain-charge matrix
D	Electrical displacement
e	Piezoelectric stress-charge matrix
E	Electrical field matrix
K	Mechanical stiffness
M	Mass
S	Material strain
T	Material stress
ε_S	Dielectric constants measured at constant strain
θ	Piezoelectric electromechanical coupling

Vectors:

f	Applied force
N	Shape function
q	Applied charge

r	Variable in displacement potential that is dependent solely on time
u	Displacement
v	Variable in voltage potential that is dependent solely on time, voltage
ϕ	Electrical potential
ψ	Variable in potentials that is dependent solely on position

Scalars and Operators:

A	Area
C_{shunt}	Shunt capacitance
d	Centroidal distance from datum
E	Elastic modulus of elasticity
f	Frequency
G	Shear modulus of elastic, Feedback gain
h	Plate or layer thickness
I, I'	Mass moments of inertia
J	Polar moment of inertia
k	Stiffness
L	Length
L_u	Differential operator
L_ϕ	Gradient operator
m	Mass,
m_θ	Moment
n	Ratio of elastic moduli

p	Force
Q	Quality factor
t	Time, thickness
T	Tension, Kinetic energy
T_m	Melting temperature
u	Axial displacement
U	Potential energy
V	Volume
w	Displacement normal to the plane of plates or membranes
W	Work
W_e	Electrical energy
W_m	Magnetic energy
y	Transverse displacement
$\bar{y}, \bar{Y}$	Centroidal height
Δf_{3dB}	Bandwidth
$\beta_n l$	Constants from the solutions to the beam equation
θ	Rotation angle about crystallographic axis X, Angular displacement
λ	Wavelength
ν	Poisson ratio
ν_A	Acoustic wave velocity
ρ	Material density
ς	Damping constant
ϕ	Rotation angle about crystallographic axis Z, Scalar electrical potential

ω	Frequency of vibration
ω_d	Damped frequency of vibration
ω_n	Natural frequency of vibration

Superscripts:

A	Actuator portion of the piezoelectric layer
P	Passive portion of the piezoelectric layer
S	Sensor portion of the piezoelectric layer
T	Transpose

Subscripts:

P	Piezoelectric
Piezo	Piezoelectric layer in the coupled electromechanical system
r	Displacement
S	Substrate
Substrate	Substrate layer in the coupled electromechanical system
V	Voltage

ACKNOWLEDGEMENTS

An endeavor of this magnitude could not have been undertaken without a lot of support, and it would be remiss of me not to acknowledge those from whom I have received aid.

Firstly, I would like to thank my advisor, Dr William W. Clark for his supervision and guidance through the whole project. In addition, I would like to acknowledge the hard work and direction afforded to me by the members of my doctoral committee: Drs James T. Cain, Marlin H. Mickle, Jeffrey S. Vipperman and Qing-Ming Wang. I would also like to thank David J. Kenny of Saronix, LLC whose suggestions and insights into the operation of resonators proved to be invaluable.

Secondly, I would like to thank all the members of the Vibration and Control Laboratory, past and present, with whom I have interacted. Without your companionship and help as sounding boards this work would never have been completed.

Lastly, and by no means least, I would like to recognize the members of the Muriuki family, and especially my parents, for their love and support.

1.0 INTRODUCTION

Time has dictated the movement and behavior of humans for ages. From early times, the seasons have dictated when crops can be grown. Societies that depended on venison for sustenance had to follow the seasonal migrations of their prey. The advent of more modern farming practices has freed humans somewhat from the need to know when the seasons are about to change. However, time still rules the way in which societies are run. The passage of time has been divided into ever smaller pieces: years, months, weeks, days, hours, seconds, and now ever smaller fractions of seconds. Modern day living has been the driving force behind this division.

Time keeping itself has had to take major strides to keep pace with the needs of society. The sundial was once the best clock available. Water and sand clocks followed which used the potential energy of water or sand to fill or empty containers. Markings on the containers were used to keep track of the passage of time. More accurate measures of time became available with the advent of mechanical clocks that used some form of stored mechanical energy to drive hands around a clock face. Ingenious mechanisms made this type of clock the most accurate time keeping device into the early 20th Century.

In the 1920s, quartz crystal oscillators and clocks were introduced (Gerber, 1985). This was the dawn of a new era in clock accuracies. Quartz is the material used in the majority of resonators

that are found in devices today. Through the 20th Century higher and higher frequencies and greater clock accuracies have been achieved using precision frequency devices. Current precision frequency devices have a frequency source that uses quartz at the lower end of the precision spectrum and atomic vibrations at the higher end e.g. the second is defined as 9,192,631,770 periods of the radiation associated with the transition between the two hyperfine levels of the ground state of the Cesium atom, Cs^{133}.

This internationally accepted definition of the second is used in the systems of units that are the basis of the physical sciences. Within the framework defined by the base units, scientific data can be recorded, compared and reproduced since the definitions of all the units in the system are known.

The growth of the electronics industry worldwide has produced a ready market for accurate and cheap frequency sources. These frequency sources appear in such diverse places as engine management systems, wristwatches, cell phones, toasters, radios, cameras and satellites. The desired characteristics of the resonators differ from application to application. For example, an extremely stable frequency source is needed in satellites such as those used in the Global Positioning System (GPS), while secure radio communications may need a frequency source that can rapidly and accurately switch between various frequencies.

1.1 RESONATORS

Resonators can either be a mechanical or an electrical device. In the mechanical devices, a mechanical strain is produced in the material and the material properties define the frequency

of oscillation. To be useful in an electronic device, the mechanical strain has to be sensed, controlled and converted into an electrical signal.

Mechanical resonators in electronic devices are made in whole or in part of ferroelectric or ferroic materials. Ferroics have a material structure whose orientation can be changed either by the application of a magnetic or an electric field or an elastic deformation or some combination of these fields and deformations (Rosen, 1992). In piezoelectric materials this structure or domain change is what allows the coupling of mechanical strain and electrical signal through the piezoelectric effect. Piezoelectricity shall be covered in greater detail in the next chapter.

Mechanical resonators for electronic devices are well understood and have been the subject of research for almost a century. A case in point is the ubiquitous quartz resonator that has been the subject of study for about 80 years. There is little that is not known about the physical and electrical characteristics of the quartz resonator. For example, the effects of temperature on the frequency of operation of quartz have been characterized and zero-temperature coefficient quartz resonators developed.

As mentioned previously, electrical devices are the second type of resonator. Electrical resonators do not have to transform mechanical energy to electrical energy. This is an advantage since there are always energy losses when the energy is transformed from mechanical to electrical energy and back again. These energy losses are further compounded by the losses inherent to the devices; through damping found in mechanical components and the resistance of electrical components.

Current electronics need resonators that operate at higher frequencies. This need has developed concurrently with the shrinking size of electronic devices. The physical size of both the mechanical and electrical resonators is dictated by the frequency of oscillation and the properties of the material utilized in the resonator. A resonator small enough to fit on a chip would simplify manufacturing of devices as well as help in further reducing product size.

One of the current focal points of mechanical resonator research has been miniaturization of resonators. This research has been driven by the needs of the electronics industry and the burgeoning micro and nano-technology fields. The ultimate goal of this growing field of research is to develop miniature resonators that can be built in conjunction with the electronics using micromachining techniques. Miniature quartz resonators can be built, but quartz production steps are not compatible with the micromachining steps used in making electronics. Thus materials other than quartz will have to be used.

Using materials other than quartz introduces several issues that need to be addressed before these materials can be used in electronic devices. The frequency range of the resonators made from these materials need to be determined. In addition, the frequency stability, quality factor, temperature stability, brittleness, weight, price, availability, etc. of the materials will all need to be considered before commercial acceptance of resonators made from substitute materials is achieved.

1.1.1 Resonator Techniques

Mechanical resonators for electronic devices can be made using piezoelectric materials. As the piezoelectric material is strained this produces changes in the electric charges on the surface of

the material. If electrodes are deposited on the surfaces where these charges accumulate, the strain can be measured or sensed from the charge accumulated. Since applying a charge to the surface of the piezoelectric can produce a mechanical strain, the electrodes can also be used to actuate strains in the material. The sensor and actuator are used to induce mechanical vibration of the piezoelectric material at a particular frequency of oscillation.

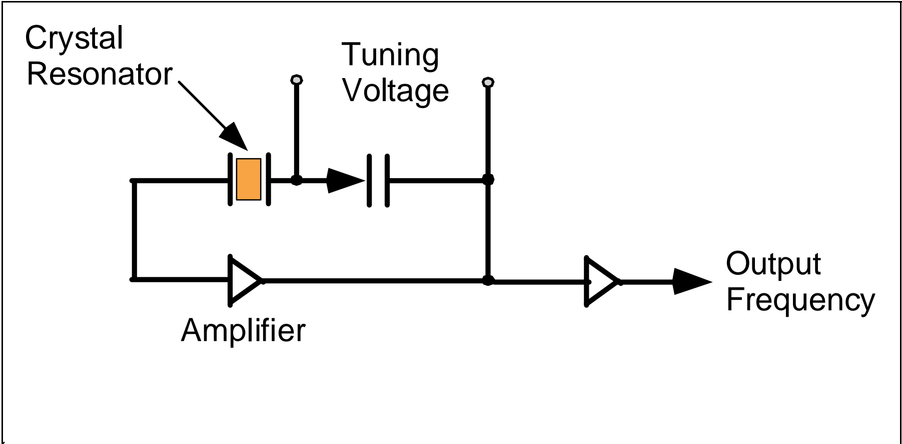

Figure 1. Simplified quartz crystal circuit diagram

A simplified quartz crystal oscillator is shown in Figure 1 (Vig, 2001). The electrode surfaces can be seen on either side of the crystal resonator. In quartz crystal oscillators the crystal appears in the feedback loop of the amplifier. Electrical circuit equivalents for the crystal resonator shown have been developed. One such equivalent circuit is the Butterworth-VanDyke equivalent circuit in Figure 2.

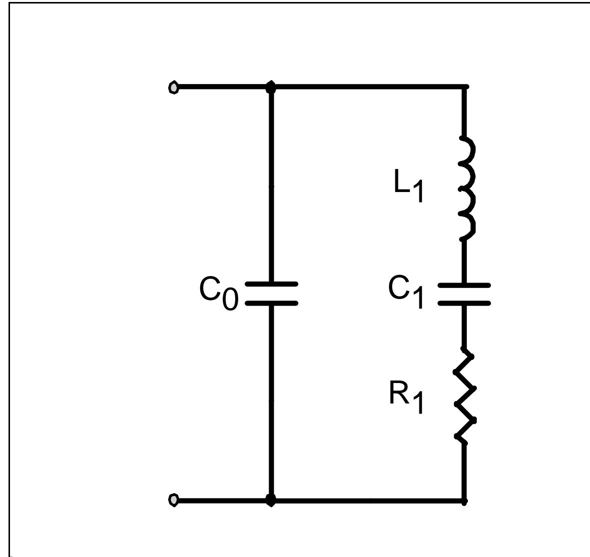

Figure 2. Butterworth-VanDyke equivalent circuit for crystal resonators

The equivalent circuit is a second order system with the values of the circuit elements obtained from the dimensions and characteristics of the crystal. These dimensions and characteristics determine the resonance frequency of the oscillator.

The frequency of oscillation can be changed by biasing the capacitor in Figure 1 with a voltage. The typical tuning range of a quartz crystal oscillator is less than ten thousandths of the operating frequency, i.e. less than 0.01% of the operating frequency.

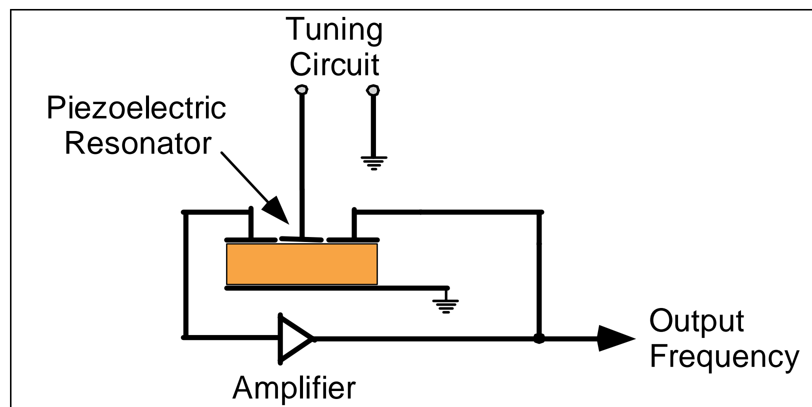

Figure 3. Simplified piezoelectric resonator circuit

In Figure 3 the piezoelectric resonator circuit used in this research is shown. The differences between the quartz crystal circuit shown and the piezoelectric resonator circuit are that there are extra electrodes added to the piezoelectric, a ground electrode and an electrode that is used for tuning the frequency of resonator. The shunt tuning technique either leaves the tuning circuit contacts open, shorts the electrode to ground or puts a capacitor between the electrode and ground. Depending on the piezoelectric material used, this tuning technique gives a theoretical tuning range over 1000 times larger than that afforded by the quartz crystal tuning technique.

1.2 OBJECTIVES OF THE WORK

This work investigates the suitability of one of the alternative piezoelectric materials (other than quartz) for making miniature, tunable mechanical resonators. The piezoelectric material to be investigated is lead zirconate titanate (PZT). This work will focus on the frequency of operation of the resonators, the amount of tuning achievable with the shunt tuning technique, and the feedback technique and amplifier gain required for resonator operation.

The frequency of vibration of the resonator is dependent on the type of vibration (bending, shear, etc) as well as the mode number of the vibration. The frequencies are also determined by the material properties of the resonator and the dimensions of the resonator. In general, the smaller the resonator the higher the frequencies of vibration will be. Miniaturization of the mechanical resonator, consequently, allows a higher frequency resonator to be made. Hence high frequency, miniature, tunable mechanical resonators (with possible on chip applications) are realizable.

An analytical model was developed to identify the frequencies of vibration of bending resonators. The frequencies of vibration predicted by the bending type model shall be verified using cantilever beam bending type resonators.

The effectiveness of the shunt tuning technique to be used is dependent on the type of vibration. The electrode placement has to be such that the mechanical vibration that is generated can be sensed. Piezoelectric materials have different degrees of electromechanical coupling to different types of mechanical strains. For some vibration, e.g. shear and longitudinal, the electromechanical coupling and ability to electrode the piezoelectric material limits tuning. Further, the size and placement of this electrode on the resonator surface determines the amount of tuning that can be achieved.

This work shall investigate applying the tuning technique to bending-type resonators. An analytical model was developed that predicts the tuning range available for a bending type resonator operating at different frequencies of vibration. Experimental verification was made with cantilever beam bending type resonators.

The gain that needs to be developed in the feedback loop, shown in Figure 1 and Figure 3, is a function of the voltage required to cause the vibration and the sensor voltage obtained. The placement and size of the actuator electrode will determine the actuator authority, i.e. how much voltage needs to be applied to the electrode to obtain the desired deflection. The voltage generated by the sensor is in turn a function of the sensor placement and size. Consequently, how the actuator and sensor electrode patterns and size affects this gain was determined with a

view to reducing the gain required for resonator operation (The ability to physically realize the system is a benefit of minimizing the feedback gain).

As discussed above, Quartz crystal resonator technology is well established. Quartz is also a piezoelectric material. Consequently, some of the circuits that are used in quartz crystal resonators were looked at with a view to adapting the circuit architecture to the, tunable, mechanical resonator. To achieve this the more well-known circuit types, Pierce, Colpitts, Clapp, etc., were studied and similarities and differences with the current amplifier setup used investigated.

2.0 PIEZOELECTRICITY

2.1 THE PIEZOELECTRIC EFFECT

The piezoelectric effect is exhibited in materials (crystal or non-crystalline) that do not have a center of symmetry. When such a piezoelectric material is mechanically loaded, a change occurs in the polarization of the material, i.e. an electrical charge is generated on opposite faces of the material. This phenomenon is called the direct piezoelectric effect. The converse piezoelectric effect occurs when an electrical charge applied to the material causes a mechanical stress in the material (Gautschi, 2002).

2.2 PIEZOELECTRIC MATERIALS

The materials that exhibit the piezoelectric effect can be catalogued into two broad categories based on their structure. These two categories are those piezoelectric materials that are crystalline and the materials that are non-crystalline.

2.2.1 Crystalline Piezoelectric Materials

2.2.1.1 *Quartz.* Quartz is the most commonly used piezoelectric material. As such, other materials and the properties that they have are customarily compared to those of quartz.

The form of Quartz (SiO_2) that is used for its piezoelectric properties has the α-quartz structure. In this form it consists of repeated tetrahedra of SiO_4. Each of the corners of the

tetrahedron is shared with another tetrahedron. α-quartz can be either natural or artificial. The artificial or cultured α-quartz can be grown from nutrient (a solution of dissolved natural crystals) in an autoclave using seed crystals as the catalyst for crystallization (Gerber, 1985). In this manner, large single crystal quartz can be grown from lots of small natural crystals. Defects in the material are minimized by careful control of the autoclave temperature and temperature gradient, careful selection of the material for the nutrient, ensuring slow growth of the crystals and inclusion of additives such as Lithium to the nutrient.

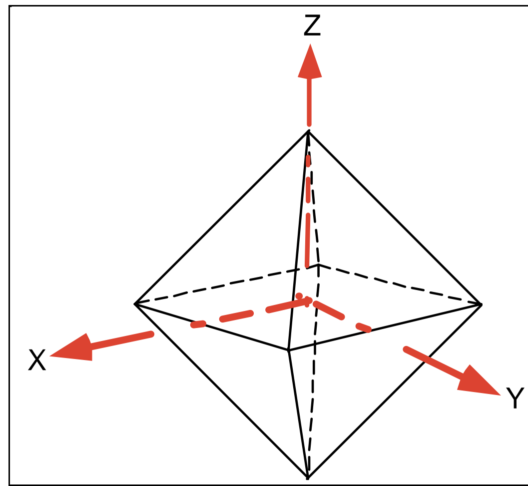

Figure 4. Crystal with crystallographic axes indicated

In quartz, it has been shown that different cuts exhibit different material property stabilities, especially in relation to changes in temperature. The cuts are defined based on the crystallographic axes. An example crystal with crystallographic axes is shown in Figure 4. The quartz cuts can be either singly or doubly rotated cuts. In the singly rotated cuts the crystal is rotated about only one of the three crystallographic axes before it is cut. There are rotations about two axes of the quartz before slicing in the doubly rotated cut crystal. The cuts are given by rotations about the crystallographic X and Z axes with the angles given by θ and ϕ respectively.

The first cut found to have a zero temperature coefficient is the AT cut and the rotations about the axes are $32.25^\circ \le \theta \le 32.33^\circ$ and $\phi \approx 0$. The term zero temperature coefficient refers to the change in the frequency of vibration with respect to temperature at a specified temperature (usually room temperature). Some other quartz crystal zero temperature coefficient cuts are the SC cut ($32.25^\circ \le \theta \le 32.33^\circ$ and $\phi = 22.0^\circ$), the BT cut ($\theta = 49.20^\circ$ and $\phi \approx 0$) and the RT cut ($\theta = -34.50^\circ$, $\phi \approx 0$). Other common zero temperature coefficient cuts are the FC cut ($\theta = 15^\circ$, $\phi = 34.33^\circ$), IT cut ($\theta = 19.10^\circ, \phi = 34.08^\circ$), and the SC cut ($\theta = 21.93^\circ$, $\phi = 33.93^\circ$). The LC cut ($\theta = 11.17^\circ, \phi = 9.39^\circ$) is a linear temperature coefficient cut and is used in crystal thermometers (Mason, 1977; Vig, 2001).

The density of Quartz is 2649 kg/m^3 and the crystal melts at 1710 $^\circ$ C. Compressive strength has been measured in the range between 2 and 3 GPa. Tensile strength is much lower, around 120 MPa (Gautschi, 2002). Quartz is a member of the trigonal class 32 and has a piezoelectric strain matrix that is populated as below.

$$d = \begin{bmatrix} d_{11} & -d_{11} & 0 & d_{14} & 0 & 0 \\ 0 & 0 & 0 & 0 & -d_{14} & -2d_{11} \\ 0 & 0 & 0 & 0 & 0 & 0 \end{bmatrix} \qquad (2.2\text{- }1)$$

In the piezoelectric strain matrix, the first three rows correspond to the crystallographic axes, X, Y and Z respectively. The first three columns are extensional strains in the three axis directions, ε_X, ε_Y and ε_Z, and the last three columns of the strain matrix are the three shear strains, ε_{YZ}, ε_{ZX} and ε_{XY}, respecctively. The constants d_{11} and d_{14} are 2.30×10^{-12} and $0.67 \times 10^{-12} CN^{-1}$ respectively, where C is charge in Coulombs and N is force in Newtons. The temperature

coefficients for the piezoelectric constants d_{11} and d_{14} of α-quartz are $-2.15\times10^{-4}K^{-1}$ and $12.9\times10^{-4}K^{-1}$, where *K* is temperature change in Kelvin.

2.2.1.2 *Rochelle Salt.* The work done in 1880 by Pierre and Paul-Jacques Curie on crystals, including Rochelle salt, identified the piezoelectric phenomenon. Single crystals of Rochelle salt ($NaKC_4H_40_6 \bullet 4H_20$) have high piezoelectric sensitivity and were used in the crystal pickups of phonographs (Gautschi, 2002). The Curie temperature of Rochelle salt is 23 $^\circ$C. The Curie temperature is the temperature above which a ferroelectric substance loses its ferroelectricity. Rochelle salt easily dehydrates in vacuum or dry air (Kingery, 1987).

2.2.1.3 *Tourmaline.* Tourmaline, $(Na,Ca)(Mg,Fe)_3B_3Al_6Si_6(O,OH,F)_{31}$, has high mechanical strength and, like quartz, is unaffected by most alkali and acids. It has a density of 3100 kg/m^3. Like quartz, tourmaline is a member of the trigonal system, though classified as 3m. The piezoelectric matrix for the 3m class is,

$$d = \begin{bmatrix} 0 & 0 & 0 & 0 & d_{15} & -2d_{22} \\ -2d_{22} & d_{22} & 0 & d_{15} & 0 & 0 \\ d_{31} & d_{31} & d_{33} & 0 & 0 & 0 \end{bmatrix} \qquad (2.2\text{- }2)$$

The constants d_{15}, d_{22}, d_{31} and d_{33} are $3.63\times10^{-12}, -0.33\times10^{-12}, 0.34\times10^{-12}$ and $1.83\times10^{-12}CN^{-1}$ respectively.

The piezoelectric constant, d_{33}, varies less than two percent over a temperature range from -192° to 19° C. Tourmaline also does not undergo a change of phase below a temperature of 900° C. However, the crystal is highly pyroelectric and, in its natural form, is brittle. Natural

sources of tourmaline do not yield the necessary quantities and quality of crystal for commercial utilization. Another disadvantage of tourmaline is that artificially grown crystals do not reach usable size. These properties make tourmaline expensive to work with since selection, working and finishing the crystals is difficult.

In comparison to quartz, tourmaline has a lower longitudinal thermal expansion coefficient over a temperature of 0° to 320°C. In the matrix of elastic moduli, the tourmaline c_{11} coefficient, which relates stress and extensional strain in the crystallographic X direction, is three times larger than the quartz c_{11} coefficient.

2.2.1.4 *Gallium Orthophosphate.* Crystalline gallium orthophosphate or gallium phosphate, $GaPO_4$, due to crystallographic symmetry has no pyroelectric effect and can be used in high temperature applications. The crystal structure is similar to that of α-quartz, i.e. trigonal class 32. The piezoelectric strain matrix of gallium phosphate is, therefore, given by Equation (2.2-1). Gallium phosphate has a material density of 3570 kg/m^3, which is slightly denser than tourmaline. The quartz homeotype $GaPO_4$ is grown hydrothermally from acidic solutions.

The piezoelectric strain matrix coefficients d_{11} and d_{14} are 4.5×10^{-12} and $1.9\times10^{-12}CN^{-1}$ respectively which are higher than the quartz coefficients which are 2.30×10^{-12} and $0.67\times10^{-12}CN^{-1}$ respectively (Gautschi, 2002). No significant changes are observed in the coefficients d_{11} and d_{14} to a temperature of 500°C and the deviation is within a few percentage points of the value at room temperature at 700°C. The structure of the low temperature crystal is stable to 950°C. Another benefit of the crystal is that due to the positive temperature

coefficients of the elastic constants c_{66} and c_{14}, temperature compensated bulk and surface wave devices can be constructed from cuts of gallium phosphate. Bending strength of Gallium phosphate has been found to be similar to that of quartz.

2.2.1.5 *The CGG Group.* The CGG ($Ca_3Ga_2Ge_4O_{14}$) group is a group that contains more than 40 single, synthetic crystal compounds (Gautschi, 2002). The group crystals are of the trigonal class 32, members of which include quartz and gallium phosphate. Like gallium phosphate the CGG group crystals are non-pyroelectric but piezoelectric data is available for only about a quarter of the crystals.

Some of the more important crystals from this group are CGG, $La_3Ga_5SiO_{14}$ (LGS or Langasite), $La_2Ga_{5.5}Ta_{0.5}O_{14}$ (LGT or Langatate), $La_3Ga_{5.5}Nb_{0.5}O_{14}$ (LGN), $La_3Ga_5GeO_{14}$ (LGG) and $Sr_3Ga_2Ge_4O_{14}$ (SGG). All the CGG group crystals show no phase transition below the crystal melt temperature and high electromechanical coupling. For example, SGG sensitivity is approximately four times that of quartz. Characterization of the materials is incomplete at elevated temperatures. Growth of the crystals of LGS is difficult due to evaporation of Ga_2O_3 and GeO_2 from solution. During the growth of SGG crystals, evaporation of GeO_2 complicates matters. Large crystals of SGG are prone to cracking and often have inclusions that reduce crystal quality.

The table below (Gautschi, 2002) summarizes some of the piezoelectric properties of some of the CGG group of crystals. The coefficients e_{ij} relate electrical displacement and strain and is the product obtained by multiplying the matrix of constants, *d*, by the matrix of elastic constants, *c*.

Table 1 Piezoelectric Properties of some single crystals of the CGG group

Material and Abbreviation		Melting Temp, T_m ($^\circ C$)	d_{11} ($pC \cdot N^{-1}$)	d_{14} ($pC \cdot N^{-1}$)	e_{11} ($GN \cdot C^{-1}$)	e_{14} ($GN \cdot C^{-1}$)
$Ca_3Ga_2Ge_4O_{14}$	CGG	1370	5.38	-2.58		-0.0014
$La_3Ga_5SiO_{14}$	LGS	1470	6.16	-5.36	0.45	-0.077
$La_3Ga_5GeO_{14}$	LGG	1470	6.59	-5.51		
$La_2Ga_{5.5}Ta_{0.5}O_{14}$	LGT	1510			0.54	0.07
$La_3Ga_{5.5}Nb_{0.5}O_{14}$	LGN	1510	6.63	-5.55	0.44	-0.05
$Sr_3Ga_2Ge_4O_{14}$	SGG	370	9.41	-6.96	0.567	-0.055

2.2.1.6 *Lithium Niobate and Lithium Tantalate.* Lithium niobate and tantalate have excellent electromechanical properties with high piezoelectric sensitivity. Both lithium niobate and tantalate, like tourmaline, belong to trigonal class 3m (see Equation 2.2-2 above). The Curie temperature for lithium niobate ($LiNbO_3$) is 1197° C, which is just below its melting temperature of 1260° C. The Curie and melting temperatures of lithium tantalate ($LiTaO_3$) are 620° C and 1560° C respectively (Gerber, 1985).

The material properties of the crystals show relatively low temperature dependence. Crystals of lithium niobate and tantalate require poling to obtain single-domain crystals. Of the two crystals lithium tantalate is quite easily the more dense, 7450 kg/m^3 as opposed to 4640 kg/m^3 for lithium niobate. However, the elastic modulus coefficient, c_{11}, for both materials is quite similar, 203 GPa and 229 GPa for niobate and tantalate respectively. The piezoelectric strain constants d_{22}, d_{31}, d_{33} and d_{15} are 21×10^{-12}, -1×10^{-12}, 6×10^{-12} and $68\times10^{-12}CN^{-1}$ respectively for lithium niobate; and 7.6×10^{-12}, -3×10^{-12}, 7×10^{-12} and $26\times10^{-12}CN^{-1}$ for lithium tantalate.

2.2.1.7 *Other single crystal compounds.* Lithium tetraborate or LTB ($Li_2B_4O_7$) has tetragonal symmetry of class 4mm. LTB has a density of 2450 kg/m^3, on par with the density of quartz. The material has a relatively low melting temperature of 917°C. Lithium tetraborate is not ferroelectric but is pyroelectric. The crystals of LTB exhibit high electromechanical coupling with piezoelectric strain constants d_{15} and d_{33} of 8.07×10^{-12} and $24\times10^{-12}CN^{-1}$ respectively (Gautschi, 2002).

Bismuth germanium oxide or BGO ($Bi_{12}GeO_{20}$) and Bismuth silicon oxide or BSO ($Bi_{12}SiO_{20}$) show no pyroelectricity and one independent piezoelectric strain coefficient with d_{14}=d_{25}=d_{36}. In BGO the independent coefficient d_{14} is $37.6\times10^{-12}CN^{-1}$. BSO has a slightly larger coefficient, d_{14} is $40\times10^{-12}CN^{-1}$. The density of bismuth germanium oxide is 9230 kg/m^3.

Lithium sulfate-monohydrate, also known by the abbreviations LH or LSH has chemical formula, $Li_2SO_4\bullet H_2O$. Due to dehydration of the crystal above 100°C LSH is not used in applications where the temperature exceeds 90°C. LSH does have the advantage of having a relatively large piezoelectric strain coefficient.

The ferroelectric semiconductor SbSI has a peak piezoelectric strain coefficient, d_{33}, of over $2000\times10^{-12}CN^{-1}$ at about 15°C. The peak d_{33} value is twice the value at -10°C. Another shortcoming of SbSI besides the large variation in d_{33} value is that the Curie temperature is a mere 22°C.

2.2.2 Non-crystalline Piezoelectric Materials

The non-crystalline piezoelectric materials are predominantly ceramic in nature. To exhibit piezoelectric behavior the materials require poling. Poling or polarization is normally achieved at an elevated temperature by applying a high electric field across the material.

Ceramics have some advantages over crystalline piezoelectric materials (Gautschi, 2002). These advantages include a lower processing and manufacturing cost, ready availability of the constituent materials of the ceramic and higher piezoelectric sensitivity.

Ceramics have some disadvantages as well. Some of the ceramics are difficult to pole. During poling, the change in size associated with the phase change may cause cracking. Aging or loss of polarization can also occur if the ceramic is under mechanical load at high temperatures. These all affect the stability of the piezoelectric ceramic. Another disadvantage is that the ceramics may exhibit dependence of electromechanical properties on temperature. This is especially so in the vicinity of the Curie temperature of the materials. Thirdly, the temperature range over which the ceramic is useful is determined by the Curie temperature above which all piezoelectric properties are lost. Pyroelectricity is another problem that can lead to the inability to distinguish between changes in temperature or changes in the mechanical strain of material as the root cause of the change in electric field on the material. Lastly the resistivity of ceramics is, in general, lower than in crystals. This means that sensors made of ceramics cannot be used to make quasistatic measurements since the lower resistance of the ceramic in the sensor causes charge leakage when changes in strain are very slow (quasistatic).

2.2.2.1 *Barium Titanate.* Crystals of barium titanate, $BaTiO_3$, also show the piezoelectric effect but most of the experiments have been undertaken on the ceramic form of the substance (Rosen, 1992).

The Curie temperature of barium titanate is only 120° C and it has a material density of 5720 kg/m^3. The elastic modulus coefficient c_{11} is about 166GPa. Common values of the piezoelectric strain coefficients d_{15}, d_{31} and d_{33} are 270×10^{-12}, -79×10^{-12} and $191\times10^{-12}CN^{-1}$.

2.2.2.2 *Bismuth Titanate family.* Bismuth titanate and several other compounds that are related to bismuth titanate through the substitution of one or more elements, belong to a family called the bismuth titanate family (Gautschi, 2002). This family of piezoelectric materials, which is also called the bismuth layer structure ferroelectrics, exhibits some enhanced piezoelectric through the substitutions effected. Bismuth titanate has piezoelectric strain coefficients d_{33}, d_{31} and d_{15} of 18×10^{-12}, -2×10^{-12} and $16\times10^{-12}CN^{-1}$.

Bismuth titanate has a Curie temperature of 650° C. The Curie temperatures of other members of the family are Bi_3TiNbO_9 940° C, $SrBi_2Nb_2O_9$ 440° C, $Na_{0.5}Bi_{4.5}Ti_4O_{15}$ 655° C, $SrBi_4Ti_4O_{15}$ 530° C and $CaBi_4Ti_4O_{15}$ 787° C.

2.2.2.3 *Tungsten Bronze family.* One of the materials used in transducers in non-destructive testing and medical purposes is lead metaniobate ($PbNb_2O_6$), which is a member of the tungsten bronze family (Gautschi, 2002). Lead metaniobate is used due to its high piezoelectric strain coefficients. Lead metaniobate has a Curie temperature of 500° C and strain

coefficient d_{33} of $100\times10^{-12}CN^{-1}$. $(BaPb)Nb_2O_6$ has a lower Curie temperature (400°C) and d_{33} strain coefficient ($85\times10^{-12}CN^{-1}$).

2.2.2.4 *Perovskite Layer Structure Ferroelectrics.* Like the bismuth titanate family, these materials have a layered structure. The best known members $Sr_2Nb_2O_7$ and $La_2Ti_2O_7$, have quite high Curie temperatures, 1342°C and 1500°C respectively. By comparison, the solid solution $Sr_2(Nb_{0.5}Ta_{0.5})_2O_7$ has a Curie temperature of only 820°C and a piezoelectric strain coefficient d_{15} of $2.6\times10^{-12}CN^{-1}$. Despite its lower Curie temperature, this solid solution has the highest resistivity of tested ceramic materials (Gautschi, 2002).

2.2.2.5 *Lead Zirconate Titanate (PZT).* The most widely used of the piezoelectric ceramics is lead zirconate titanate or PZT. PZT is a solid solution of lead zirconate, $PbZrO_3$, and lead titanate, $PbTiO_3$. The solutions are made in a range from pure lead zirconate to pure lead titanate. The percentage of zirconate or titanate in the mix determines not only the phase of the solution at a particular temperature but also certain material properties like the piezoelectric coefficients.

Lead titanate, at one extreme, has the same basic structure as barium titanate. The Curie temperature of PbTiO3 is 490°C. One problem of ceramic lead titanate is that it is prone to cracking as it cools from the Curie temperature. Further, attempts at poling at room temperature with an electric field are rarely successful. The high conductivity of the ceramic near the Curie temperature makes higher temperature poling impractical. Lead zirconate is antiferroelectric and thus cannot form a piezoelectric ceramic. If anything above ten mole

percent of PbTiO3 is in solid solution with PbZrO3, then the solution becomes ferroelectric (Rosen, 1992). The highest piezoelectric sensitivity is found in a solution that contains 55% lead zirconate. Typical values of the Curie temperature for soft and hard PZT are 250° and 330° C respectively. PZT is classified as either hard or soft depending on the elasticity of the ceramic. PZT-5A and PZT-5H are two examples of soft PZT. Hard PZT has piezoelectric coefficients d_{33} and d_{31} of 190×10^{-12} and $-55\times10^{-12}CN^{-1}$ respectively. Soft PZT has piezoelectric constants d_{33}, d_{31} and d_{15} of 425×10^{-12}, -170×10^{-12} and $500\times10^{-12}CN^{-1}$. The density of PZT varies depending on composition but is approximately 7700 kg/m^3. PZT belongs to the class of symmetry *6mm* and ∞mm which has the matrix of piezoelectric strain coefficients as below.

$$d = \begin{bmatrix} 0 & 0 & 0 & 0 & d_{15} & 0 \\ 0 & 0 & 0 & d_{15} & 0 & 0 \\ d_{31} & d_{31} & d_{33} & 0 & 0 & 0 \end{bmatrix} \tag{2.2- 3}$$

The success of PZT formulations has led to investigations into similar solid solutions. Two of these similar solid solutions are PZN-PT (Lead Zinc Niobate–Lead Titanate) and PMN-PT (Lead Manganese Niobate-Lead Titanate). The chemical formula for PZN-4.5%PT is $Pb(Zn_{1/3}Nb_{2/3})O_3$-4.5%$PbTiO_3$ while that of PMN-PT is $Pb(Mg_{1/3}Nb_{2/3})O_3$-$PbTiO_3$. For PZN-4.5%PT the piezoelectric coefficients d_{33}, d_{31} and d_{15} are 2140×10^{-12}, -980×10^{-12} and $130\times10^{-12}CN^{-1}$ respectively (Hackenberger, 2002). PMN-PT has piezoelectric coefficient d_{33} that varies between 1400×10^{-12} and $3500\times10^{-12}CN^{-1}$. For PMN-PT the advantages of this high piezoelectric strain coefficient and a Young's modulus of 105 GPa are offset by the fact that the Curie temperature is as low as 75° C (H.C. Materials Corp., 2002). Hackenberger indicated that PZN-PT crystals grow in irregular shapes and are generally quite small. PMN-PT crystals

grow faster and are easier to machine. PZN-PT and PMN-PT densities are slightly higher than the density of PZT at 8300 kg/m^3 and 7900 kg/m^3 respectively.

2.2.2.6 *Aluminum Nitride.* Aluminum nitride is a non-ferroelectric substance that has piezoelectric behaviour when deposited as a thin film. The piezoelectric effect of thin films of AlN_3 has been observed at temperatures of 1150° C (Gautschi, 2002). Aluminum nitride has a density of 3260 kg/m^3 , modulus of elasticity of 331GPa and a melting temperature of 2200° C. The piezoelectric coefficient d_{33} of aluminum nitride is $3.9\times10^{-12}CN^{-1}$ (Dubois, 1998).

2.2.2.7 *Zinc Oxide* Thin films of zinc oxide, ZnO, are used in micro-devices to provide actuation or sensing through the piezoelectric effect. ZnO can be deposited on the target surface or substrate by reactive sputtering (Racine, 1998), rf magnetron sputtering (von Preissig, 1998) or metalorganic chemical vapor deposition. Racine also notes that PZT has a larger piezoelectric effect. However, the manufacturing of thin films of ZnO using typical integrated circuit techniques is easier than manufacture using PZT as the piezoelectric material. For example, there is no need to take precautions against lead leaching into the silicon substrate. Zinc oxide has a melting temperature of 1975°C, a material density of 5610 kg/m^3 and a maximum measured d31 piezoelectric coefficient of $4\times10^{-12}CN^{-1}$ (von Preissig, 1998).

2.2.2.8 PVDF. PVDF or polyvinylidene fluoride is a polymer material that exhibits the piezoelectric effect. PVDF is not as dense as PZT, its density is only about 1780 kg/m^3 (Venkatragavaraj, 2001). PVDF also has a lower piezoelectric strain coefficients d_{33} and d_{32}. The

d_{32} and d_{33} values for PVDF are 3×10^{-12} and $28\times10^{-12}CN^{-1}$ respectively (Baz, 1996). Like PZT, PVDF requires poling using a high electric field at an elevated temperature.

To improve the piezoelectric characteristics of PVDF composites are sometimes made using other piezoelectric materials. When PZT is used to make the composites, the characteristics of the new composite are between that of PVDF and PZT. By varying the volume fraction of PZT from 10% to 70% piezoelectric strain coefficient d_{33} were measured and found to be vary between 2×10^{-12} and $23\times10^{-12}CN^{-1}$. The density of the composite was between about 2600 kg/m^3 and 5100 kg/m^3 (Satish, 2002).

2.3 PIEZOELECTRIC SYSTEMS, CLASSES AND MATERIAL STRAINS

The various piezoelectric materials in the previous section can be categorized according to the population of their various constituent matrices; including the piezoelectric strain matrix, *d*. The elements of these matrices determine which class the piezoelectric materials fall into while the system is determined by the symmetry of the crystal structure.

2.3.1 Piezoelectric Systems and Classes

In piezoelectric materials the material strains are related to electrical field and mechanical stress as follows (IEEE Std 176-1987),

$$S = (c^E)^{-1}T + d^T E \qquad (2.3\text{-} 1)$$

where c^E is the constant electrical field mechanical stiffness, T the mechanical stress, d^T is the transpose of the piezoelectric strain matrix, E is a vector of applied electric field and S is the vector of material strains. This vector of strains is,

$$S = \begin{Bmatrix} \varepsilon_{XX} \\ \varepsilon_{YY} \\ \varepsilon_{ZZ} \\ \varepsilon_{YZ} \\ \varepsilon_{ZX} \\ \varepsilon_{XY} \end{Bmatrix} = \begin{Bmatrix} \varepsilon_{X} \\ \varepsilon_{Y} \\ \varepsilon_{Z} \\ \varepsilon_{ZY} \\ \varepsilon_{XZ} \\ \varepsilon_{YX} \end{Bmatrix} \tag{2.3- 2}$$

where the first three rows of the vector of strains are extensional and the last three are shear strains. It follows then that in the piezoelectric strain matrix, d, the elements in the first column determine the ability of the material to cause extensional strains in the X direction, the second column determines extensional strains in the Y direction, and so on. Where the elements in the strain matrix are zero, it is then impossible to induce strains using applied charge. For example, in bismuth germanium oxide (shown later in Equation 2.3-9), it is impossible to cause extensional strains using an applied electrical field.

The general piezoelectric strain matrix is given by,

$$d = \begin{bmatrix} d_{11} & d_{12} & d_{13} & d_{14} & d_{15} & d_{16} \\ d_{21} & d_{22} & d_{23} & d_{24} & d_{25} & d_{26} \\ d_{31} & d_{32} & d_{33} & d_{34} & d_{35} & d_{36} \end{bmatrix} \tag{2.3- 3}$$

The three rows are the crystallographic axes: X, Y and Z respectively. If, for example, we apply a charge to an electrode perpendicular to the X crystallographic axis, we induce strains in the six strain directions. The magnitude of the strains in each of the directions is determined by the value of the elements in the first row of the matrix; d_{1j} , where j is 1,2,3…6.

2.3.1.1 Orthorhombic System. Rochelle salt is a member of this system. Within the orthorhombic system, Rochelle salt belongs to class 222. The form of the piezoelectric strain matrix for Rochelle salt is given below.

$$d = \begin{bmatrix} - & - & - & \bullet & - & - \\ - & - & - & - & \bullet & - \\ - & - & - & - & - & \bullet \end{bmatrix} \tag{2.3- 4}$$

Where the three non-zero elements in the matrix are not equal and indicated by the dots. The dashes are the elements in the matrix with a value of zero. From the piezoelectric strain matrix, it can be seen that charge applied in each of the three crystallographic directions causes shear strains.

2.3.1.2 Tetragonal System. Lithium tetraborate is a member of this system in class 4mm. The piezoelectric strain matrix form for this class member is,

$$d = \begin{bmatrix} - & - & - & - & \bullet & - \\ - & - & - & \bullet & - & - \\ \bullet & \bullet & \bullet & - & - & - \end{bmatrix} \tag{2.3- 5}$$

In the strain matrix shown above in Equation 2.3-5, the matrix elements that are tied together by a line are equal in value. For materials in the tetragonal system, charges applied to the surfaces perpendicular to the crystallographic axes X and Y induce shear strains and charges applied on surfaces perpendicular to Z cause extensional strains in all three directions.

2.3.1.3 Trigonal System. Several materials in the previous section on piezoelectric materials belong to this system. These materials are quartz, gallium phosphate and the CGG group in class 32, and tourmaline, lithium niobate and lithium tantalate in class 3m.

The piezoelectric strain matrix for class *32* is,

$$d = \begin{bmatrix} \bullet & \circ & - & \bullet & - & - \\ - & - & - & - & \circ & \otimes \\ - & - & - & - & - & - \end{bmatrix} \qquad (2.3\text{- }6)$$

where the matrix elements represented by circles with white centers are negative and the cross indicates that the element is twice the magnitude of the elements it is tied to with a line. The *32* class of materials has no strains induced by charges applied to surfaces perpendicular to the Z axis, shear strains when the charge is on the surfaces perpendicular to the Y axes and a combination of shear and extensional strains when the charges are on the surface perpendicular to the X axis.

The *3m* class strain matrix is,

$$d = \begin{bmatrix} - & - & - & - & \bullet & \otimes \\ \otimes & \bullet & - & \bullet & - & - \\ \bullet & \bullet & \bullet & - & - & - \end{bmatrix} \qquad (2.3\text{- }7)$$

For this class, charges applied to a surface perpendicular to the X axis causes only extensional strains. Charges on the surface perpendicular to the Z axis causes only shear strains while a combination of shear and extensional strains occur with charges on a surface perpendicular to the Y axis.

2.3.1.4 Hexagonal System. Lead zirconate titanate (PZT) is a class 6mm or ∞mm member of this system. The piezoelectric strain matrix is,

$$d = \begin{bmatrix} - & - & - & - & \bullet & - \\ - & - & - & \bullet & - & - \\ \bullet & \bullet & \bullet & - & - & - \end{bmatrix} \tag{2.3- 8}$$

The form of the strain matrix is identical to the tetragonal system class *4mm* material lithium tetraborate. Shear strains are induced by charges on surfaces perpendicular to the X and Y axes and extensional strains by charges on surface perpendicular to the Z crystallographic axis (which is the poling axis in PZT and other poled ceramics).

2.3.1.5 Cubic System. Bismuth germanium oxide (BGO) is a class 23 member of the system. In this class, only shear strains are induced by charges applied to surfaces perpendicular to the three crystallographic axes.

$$d = \begin{bmatrix} - & - & - & \bullet & - & - \\ - & - & - & - & \bullet & - \\ - & - & - & - & - & \bullet \end{bmatrix} \tag{2.3- 9}$$

2.3.2 Piezoelectric Strain Matrices and Induced Strains

In the previous section the piezoelectric strain matrices for several different classes of piezoelectric material were given. In this section we shall indicate what strains can be induced by the different material classes.

The piezoelectric strain matrix, *d*, indicates the strength with which different material strains are coupled to an induced charge or vice versa through the piezoelectric effect. Table 2 below

illustrates the strains that can be induced in the piezoelectric material and the surface perpendicular to which the charge needs to be applied to induce the strain.

Table 2. Applied charges and induced strains

Class	**Material**	**Charge perpendicular to**		
		X-axis	**Y-axis**	**Z-axis**
222	Rochelle Salt	ε_{YZ}	ε_{ZX}	ε_{XY}
4mm	Lithium Tetraborate	ε_{ZX}	ε_{YZ}	$\varepsilon_X, \varepsilon_Y, \varepsilon_Z$
32	Quartz, Gallium Phosphate, CGG Group	$\varepsilon_X, \varepsilon_Y, \varepsilon_{YZ}$	$\varepsilon_{ZX}, \varepsilon_{XY}$	-
3m	Tourmaline, Lithium Niobate and Tantalate	$\varepsilon_{ZX}, \varepsilon_{XY}$	$\varepsilon_X, \varepsilon_Y, \varepsilon_{YZ}$	$\varepsilon_X, \varepsilon_Y, \varepsilon_Z$
6mm, ∞mm	Lead Zirconate Titanate	ε_{ZX}	ε_{YZ}	$\varepsilon_X, \varepsilon_Y, \varepsilon_Z$
23	BGO	ε_{YZ}	ε_{ZX}	ε_{XY}

This work uses lead zirconate titanate as the piezoelectric material. From Table 2 it can be seen that it is impossible to induce the shear strain ε_{XY}. Also, to induce a shear strain the surface on which the strain is produced has to be electroded. In addition, the electrode surface has to be parallel to the poling axis, Z.

3.0 RESONATORS AND OSCILLATORS AND THEIR CHARACTERISTICS

3.1 RESONATOR CHARACTERISTICS

There are some characteristics that are considered to be desirable in a resonator. These are characteristics that make the resonator useful. These characteristics include having a high Q or quality factor and frequency stability.

3.1.1 Q

The Q value of a resonator is given as a measure of performance. The equation for Q is,

$$Q = \frac{f}{Bandwidth} = \frac{f}{\Delta f_{3dB}} \tag{3.1- 1}$$

In general, the higher the Q value, the better the resonator is. The advantages of a high Q resonator are that the resonator signal will be much larger than the noise that may be present. Also, the high Q resonator tends to hold a particular frequency better than a low Q resonator would.

The bandwidth of the resonator is the difference in the frequencies at a level 3dB down from the peak signal. The frequency, *f*, used in the calculation is the frequency at the peak of the response of the resonator (see Figure 5 below).

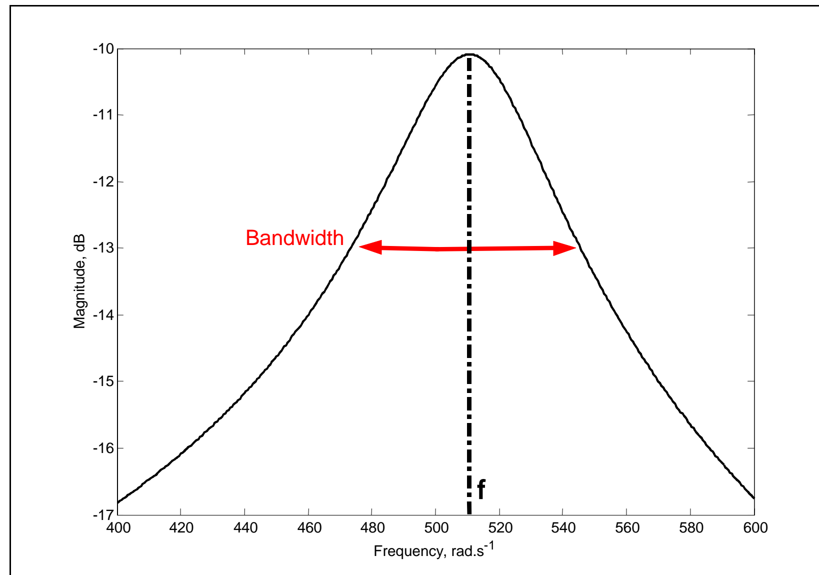

Figure 5. Q Factor

3.1.2 Stability

Stability, as it relates to resonators, is the ability of the resonator to maintain a particular frequency. There are three major measures of stability. These are jitter, drift or aging, and temperature stability. If a resonator is made specifically to be tunable this may cause the stability to be worse since the resonator will be more susceptible to disturbances.

3.1.2.1 Jitter. Jitter is the variation in the timing of a signal observable over a few periods of the signal. This timing variation is sometimes referred to as phase noise (Vig, 2001). The phase noise may be as a result of external electrical interference or mechanical shock and vibration applied to the resonator. Jitter causes non-permanent variations in frequency that are observable on time-scales of the order of the period of the resonator.

3.1.2.2 *Drift and Aging* Over time the characteristics of the components in a resonator may change. This change in the characteristics of the components may cause a change in resonant frequency. If observed over a long time, the frequency will be seen to drift as the characteristics change due to the aging of the components. External factors such as the impact

of radiation on the resonator or changes in the power supplied to the resonator may also cause the frequency of the resonator to drift. It is commonly accepted that drift can be due to a combination of effects, both external and internal to the resonator but aging is purely an internal effect (Vig, 2001).

Some of the mechanisms of aging (Vig, 2001) include mass transfer due to contamination, stress relief in the mounting or bonding of the resonator, outgassing and diffusion, chemical reactions, resonator enclosure pressure changes, circuit component aging, as well as changes in the electric field on the resonator and changes in controller circuitry (for example in oven controlled resonators).

3.1.2.3 Temperature Stability. The piezoelectric coefficients of materials are functions of temperature. The coefficients may be strongly affected by changes in temperature or weakly so, as in the AT-cut quartz crystals which are designed to have zero temperature coefficient at room temperature. If the resonator material does not have isotropic coefficients of thermal expansion then thermal stresses may be introduced into the resonator. These stresses can cause a change in the resonant frequency of the device.

Temperature stability is measured by slowly cycling the resonator temperature through the temperature range of operation and noting the change in resonant frequency. A typical range through which the temperature would be cycled is -40° to 85°C for civilian applications and -55° to 105°C for military applications (MIL-PRF-3098H). A typical specification for a resonator is that the maximum change in frequency over the operating temperature range should be 20 ppm.

3.2 TYPES OF RESONATORS AND OSCILLATORS

The various resonator and oscillator types shall be looked at first followed by the resonance and oscillation modes utilized in devices. In this work, the resonators and oscillators shall be classified according to the material that is used in manufacture or the nature of the device i.e. whether the device is mechanical or electrical in nature. Crystal resonators shall be looked at first followed by atomic devices, microwave devices that use direct electrical coupling, electrical circuit devices, and finally mechanical and electromechanical devices.

3.2.1 Crystal Resonators and Oscillators

Crystal is the most common material used in resonators and oscillators. Crystal resonators are grouped according to the mode of vibration that is induced in the crystal or the application that the crystal is used in. Quartz is the most commonly used crystal material in frequency devices due to its high stiffness and, consequently, high Q value. This leads to devices that may be capable of better frequency stability. Other crystalline materials that have recently generated a lot of interest are langasite ($La_3Ga_5SiO_{14}$) and its isomorphs, langanite ($La_3Ga_{5.5}Nb_{0.5}O_{14}$) and langatate ($La_3Ga_{5.5}Ta_{0.5}O_{14}$). These materials have a higher Q value and piezoelectric coupling than quartz crystal (Smythe, 2000).

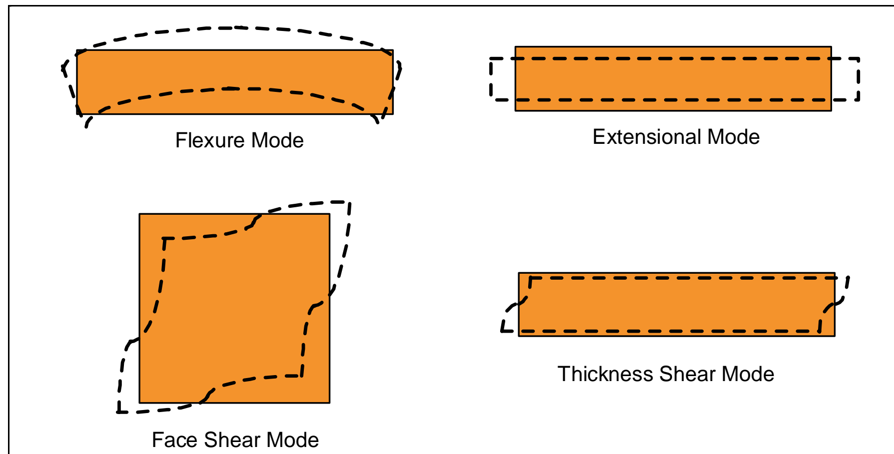

Figure 6. Examples of shear, flexure and extensional vibration modes

In the oscillator or resonator application, the crystal is forced to vibrate in one of its particular modes through electromechanical coupling using the piezoelectric effect. The most commonly used mode of vibration is the shear thickening mode (see Figure 6). Other modes involve excitation of surface acoustic waves (SAW) or bulk acoustic waves (BAW). SAW and BAW devices operate at high frequencies (MHz range), in low frequency applications the mode of vibration may be some type of flexure, either through a bar or tuning fork design.

3.2.2 Atomic Resonators and Oscillators

Atomic resonators are of various types but all use the same operating principle. The resonator is populated with a particular chemical species that has an observable transition between atomic states. Firstly, one of the states is selectively populated through manipulation of the chemical. The observable transition from the selected state to the depopulated state is then detected and used as a timing signal. Group I elements are the predominant elements used in atomic resonators (Gerber, 1985). Cesium is one such Group I element (The standard second is based on Cs^{133} transitions between two hyperfine levels of the ground state).

In general, atomic resonators are not used in isolation but usually have the timing signal from the atomic transition used as a source to which a reference crystal oscillator is frequency locked. This arrangement describes an active atomic resonator device. The reference oscillator must be some kind of tunable oscillator such as a Voltage Controlled Crystal Oscillator (VCXO). Passive atomic resonator devices use an external signal to cause the atomic transitions. This external signal may be the frequency multiplied output of a reference oscillator. The output of the atomic resonator is then used to lock the reference oscillator. In the passive device, the atomic transitions act as a frequency discriminator or filter.

3.2.3 Microwave Resonators and Oscillators

A third class of frequency source is the microwave device. Microwave devices can use either a cavity mode vibration or microstrip lines to form the signal source. In the cavity mode of vibration electrical oscillation is generated between the input and output of the device using the cavity and the walls of the cavity as coupling. The cavities can be either superconducting cavities or dielectrically loaded cavities. Frequency of operation of the device is determined both by the cavity dimensions and the contents of the cavity (Gerber, 1985; Miranda, 2000).

In microstrip line devices, a tiny gap capacitively links the input and output lines. The dimension of the gap and the use of intervening linking structures determines the operational frequency of this device (Oates, 1999).

3.2.4 Electrical Circuits

A less sophisticated way to generate an oscillating signal is to use electrical circuit components. The series combination of an inductive and a capacitive element provide the basic components required (see Figure 7). The frequency of oscillation of such a circuit is then the square root of the inverse of the magnitude of the inductor and the capacitor. Frequency selection in the electrical circuit devices is by the choice of magnitude of the capacitance and inductance of the devices.

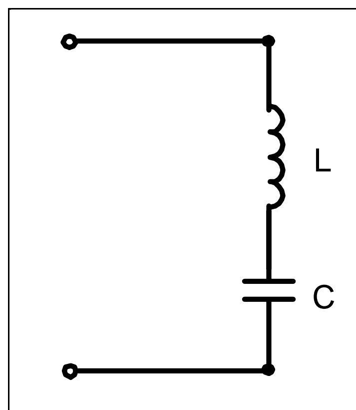

Figure 7. The basic electrical resonant circuit

An oscillating signal can also be generated using inverters arranged to form a ring oscillator. When an odd number of inverters are connected in series to form a ring, the voltage output of any of the inverters oscillates with a frequency that is the inverse of twice the sum of the propagation delays of the individual inverters in the circuit.

3.2.5 Mechan ical and Electromechanical Resonators and Oscillators

Mechanical devices utilize some form of mechanical vibration to provide the frequency of interest. A frequency of interest can be determined by selectively exciting a particular vibration

mode. Mechanical and electromechanical resonators and oscillators may be either macro or micro devices.

Most Microelectromechanical Systems (MEMS) oscillators and resonators are built using silicon chip manufacturing technology. The materials that are compatible with silicon chip micromachining are few; consequently, the oscillators and resonators are generally silicon based. As in larger scale oscillators and resonators, the micro systems work by either causing a mechanical vibration, which is electrically sensed and actuated, or by causing an electrical oscillation in a circuit without an associated mechanical vibration.

Different structures have been demonstrated for generating mechanical vibration in MEMS including comb driven resonators and resonant plates. An example of a comb driven resonator is the electrostatically driven micromechanical resonator (Nguyen, 1999). Interdigitated fingers are cut into a silicon structure that is suspended over the substrate. An input and an output set of these fingers are joined by a folded-beam structure that provides the coupling between input and output. By choosing the suspension structure, number of fingers, etc. a natural frequency for the structure can be chosen. Nguyen demonstrated a comb resonator with a Q factor of 23400 for a 16.5 kHz resonator operating at 20 mTorr (1 atm= 7.6×10^5 mTorr). The Nguyen resonator is an example of a linear resonant plate. Torsional resonant plates have also been demonstrated (Tang, 1989). In the torsional resonant plate, the comb drive or interdigitated fingers are arranged concentrically to excite torsional vibration of a spiral structure. Tang demonstrated Q factors of about 100 at 40 kHz.

Another example of a micro-oscillator component is a varactor design (Yoon, 2000). A spring loaded movable dielectric is actuated using a DC voltage bias across two plates that sandwich the dielectric. The movement of the dielectric changes the effective dielectric constant of the gap between the plates, changing the capacitance of the varactor. The varactor can be used in conjunction with other circuit components (as seen in Section 3.2.4 which deals with electrical circuits) to provide a tunable oscillatory signal.

3.3 MODES OF RESONANCE OR OSCILLATION

3.3.1 Bulk Acoustic Waves (BAW)

Bulk acoustic waves are waves that propagate through the medium *in toto* (Gerber, 1985). The thickness of the material in the direction of wave propagation determines the wavelength of the fundamental mode. If this thickness is t, then the fundamental mode wavelength is,

$$\lambda = 2t \tag{3.3-1}$$

The velocity of the acoustic wave in the medium is,

$$v_A = \sqrt{\frac{E}{\rho}} \tag{3.3-2}$$

where E is the relevant elastic constant in the direction of wave motion and ρ is the density of the material. The frequency of vibration of the fundamental bulk acoustic mode is,

$$f = \frac{v}{\lambda} = \sqrt{\frac{E}{4\rho t^2}} \tag{3.3-3}$$

In BAW devices the acoustic waves are generated between electrodes that are located on opposite sides of the material. The electromagnetic coupling effect of piezoelectric materials couples the acoustic waves to electromagnetic waves in the electrodes.

3.3.2 Surface Acoustic Waves (SAW)

Surface acoustic waves are generated between electrodes situated on the same surface of the material. Wave motion does not penetrate deep into the material and about 90% of the wave energy is within one acoustic wavelength of the surface (Vig, 2001). The electrodes on the surface of the surface acoustic wave device are interdigitated. The spacing between the digits is half the wavelength of the fundamental mode of the resonator. If we let the interdigital distance be t, then the above equations for bulk acoustic wave vibration can be used.

3.3.3 Direct Electrical Coupling

In direct electrical coupling, the electrical vibration is not transformed into a physical vibration. Examples of direct electrical coupling vibration are microwave cavity modes and microstrip lines.

3.3.3.1 *Microwave Cavity Modes.* In the microwave cavity modes, the electric field within the cavity undergoes the vibration. The cavity may be filled with a dielectric material, air or a vacuum (Chen, 1990; Mahdi, 1990; Poplavko, 2001). The dimensions of the cavity and the relative permittivity of the material within the cavity affect the impedance of the cavity and consequently, the frequency of vibration of the cavity. In transverse electromagnetic mode (TEM) vibration, the electrical field distributions of the various transverse modes resemble the membrane modes seen in mechanical vibration. The walls of the cavity act as nodes of vibration and have zero electrical field.

Direct electrical coupling is achieved by connecting the input and output probes to the wall of the cavity. Different connection schemes can be utilized to allow frequency switching and tuning (Mahdi, 1990).

3.3.3.2 *Microstrip Lines* The resonant structures found in microstrip line oscillators include rings and strips. In the ring structures, the input line passes within close proximity of the ring. If the device is to be used as a resonator, the output line may be attached directly to the ring or could be a line that passes in close proximity to the ring (see Figure 8). The space between the lines and the resonant structures acts as a capacitive link. The impedance and resonant frequency of the microstrip line oscillators is determined by the strip dimensions and the substrate under the strips (Hammerstad, 1980).

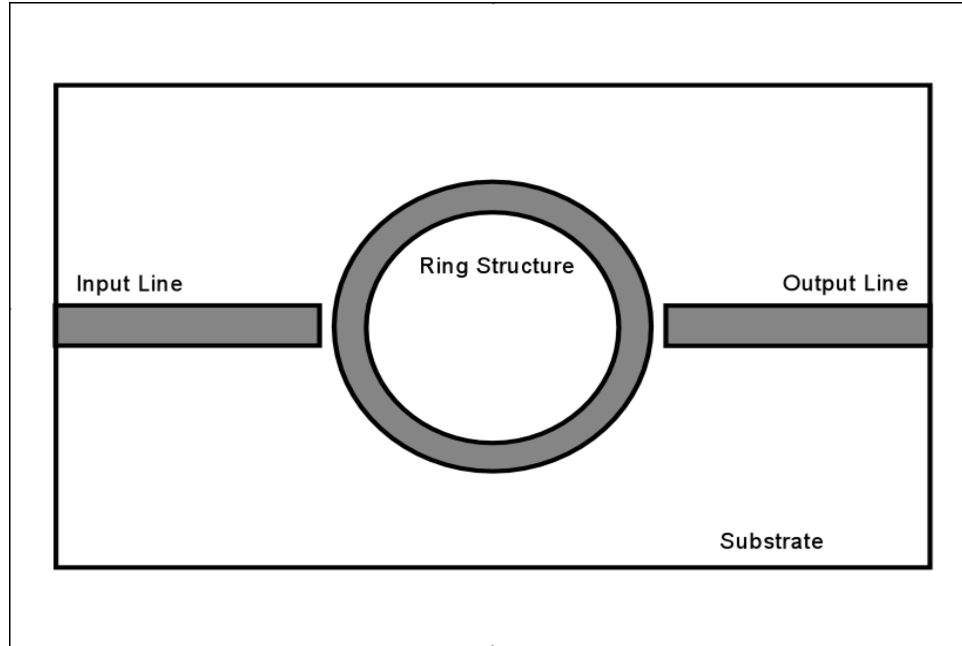

Figure 8. Microstrip Line Oscillator - Ring Type

3.3.4 Mechanical Vibration

There are several different mechanical vibration types. The vibration types can be classified based on the kind of displacement the mechanical system undergoes or on the dimensions of mechanical system involved in vibration. Hence, there is transverse vibration, torsional vibration, axial vibration, membrane vibration, etc.

3.3.4.1 Transver se Vibration. Transverse vibration is generally associated with the vibration of beams. Displacement is in a direction that is perpendicular or transverse to the long axis of the beam. A simple analysis of transverse vibration of beams could use the Bernoulli-Euler beam equation (Benaroya, 1998), which is,

$$EI\frac{\partial^4 y}{\partial x^4} + m\frac{\partial^2 y}{\partial t^2} = p(x,t) \qquad (3.3\text{-}4)$$

where *E, I* and *m* are the modulus of elasticity, mass moment of inertia and the mass of the beam respectively. The transverse displacement is *y* and the coordinate measured along the

long axis of the beam is x. A force p, which in general is a function of both the axial coordinate and time, may be applied to the beam.

With the appropriate boundary conditions, the above equation can be solved to find both the frequency of vibration and the shape of the displacement associated with that frequency of vibration (also referred to as mode shape).

3.3.4.2 Torsional Vibration. Just as transverse vibration is associated with beams, torsional vibration is associated with vibration of shafts. The equation associated with this type of vibration is,

$$I\frac{\partial^2\theta}{\partial t^2}-\frac{\partial}{\partial x}\left[GJ(x)\frac{\partial\theta}{\partial x}\right]=m_\theta(x,t) \qquad (3.3\text{-}5)$$

where I, G and J are the mass moment of inertia, shear modulus and polar moment of inertia for the cross-section of the shaft. The applied moment on the shaft is m_θ, which can be function of both the axial coordinate and time. The angular displacement is θ. Solution of this equation using the appropriate boundary conditions, just as in transverse vibration, gives the frequencies of vibration and the associated mode shapes.

3.3.4.3 Axial Vibration. Axial or longitudinal vibration involves displacement along the axis of the beam. The general form of the equation for axial vibration is,

$$\frac{\partial}{\partial x}\left[A(x)E\frac{\partial u(x,t)}{\partial x}\right]=m(x)\frac{\partial^2 u(x,t)}{\partial t^2} \qquad (3.3\text{-}6)$$

In the above equation, the mass per unit length is $m(x)$, cross-sectional area at position x along the axial coordinate is $A(x)$ and E is the modulus of elasticity. The displacement in the axial coordinate direction is u.

3.3.4.4 *Membrane Vibra tion.* Membranes and plates are structures whose dimension in the thickness direction is much smaller than the dimension in the length and width coordinate directions. Membranes are differentiated from plates by their inability to resist bending moments.

If we let x and y denote the coordinates that define the plane in which the membrane lies then the equation of motion for the membrane is,

$$\frac{T}{m(A)}\left[\frac{\partial^2 w}{\partial x^2}+\frac{\partial^2 w}{\partial y^2}\right]+\frac{1}{m(A)}p(x,y,t)=\frac{\partial^2 w}{\partial t^2} \tag{3.3-7}$$

where T is the tension in the membrane, $m(A)$ is the mass per unit area, p the force applied to the membrane surface and w is the displacement normal to the surface of the membrane i.e. the transverse direction.

3.3.4.5 Plate Vibration. For deflection normal to the plane of the plate, w, the equation of motion for a plate is,

$$\frac{Eh}{12(1-\nu^2)}\left(\frac{\partial^4 w}{\partial x^4}+2\frac{\partial^4 w}{\partial x^2 \partial y^2}+\frac{\partial^4 w}{\partial y^4}\right)+\rho h\frac{\partial^2 w}{\partial t^2}=p(x,y,t) \tag{3.3-8}$$

As before, E is the modulus of elasticity and p is the normal force applied to the plate surface. The thickness of the plate is h, ρ the plate density and ν the Poisson ratio. As in all the vibration types described in this section, the frequency of vibration and the shape of the vibration can be obtained by solving the equation of motion with appropriately applied boundary conditions.

4.0 DESIGN AND MODELING

There are a large number of choices to be made when designing a resonator. Decisions on vibration type and mode set the frequency range and the frequency of operation. Once the vibration type and mode are decided on, the next choice will be to set a layout for the resonator e.g. beam, rod, fork, plate, etc. The materials available and the properties of the materials available determine the dimensions of the resonator. Adding resonator tunability narrows the number of choices that can be made since the tuning technique used in this work is not compatible with all resonator types, e.g. SAW devices. The maximum tuning range available, in turn, is determined by the dimensions of the piezoelectric layer that can be used solely for tuning. Sensing and actuation are also to be accomplished using the piezoelectric material and so the dimensions of the electrodes for the sensor and actuator have to be determined. At the same time, sizing and placing the sensor and actuator electrodes affects the magnitude of the feedback gain required for the operation of the resonator by determining sensor voltage and actuator authority.

An analytical model for the resonator would greatly simplify the design process. Two model types were looked at; a simple single degree of freedom model and a single degree of freedom Rayleigh-Ritz model developed from the generalized Hamiltonian for electromechanical systems. The resonators were then designed to meet certain frequency, tuning and gain requirements using these models.

A cantilever bending type resonator was chosen to illustrate the concepts of tuning. Two one degree of freedom analytical models were developed. A simple beam model and a Rayleigh-Ritz model. The simple beam model does not capture the tuning that can be achieved since the model is purely mechanical in nature. The Rayleigh-Ritz model is able to capture both the mechanical and electrical nature of the problem. The Rayleigh-Ritz analytical model was then extended to the particular resonator chosen, the cantilever resonator.

Using the model, the analytical bending frequencies of vibration were found. In addition, the analytical tuning range for each of the bending modes was determined. An analytical model was also developed to show what feedback gain would be required to drive the resonator at a particular bending frequency of vibration for various actuator and sensor dimensions.

This chapter illustrates the general design and modeling procedure and applies the procedure to the cantilever beam. As indicated earlier, the analytical model can be extended to cover bending type cantilever beams with different electrode layouts and dimension.

4.1 DESIGN

A cantilever beam layout was chosen to illustrate the effects of design choices and the concept of a tunable piezoelectric resonator because of the ease with which such beams could be manufactured and because of previous experience with cantilever beams. The cantilever beam has lateral or bending beam vibration being the predominant type of vibration. The materials used were aluminum for the substrate and lead zirconate titanate (PZT) as the piezoelectric material.

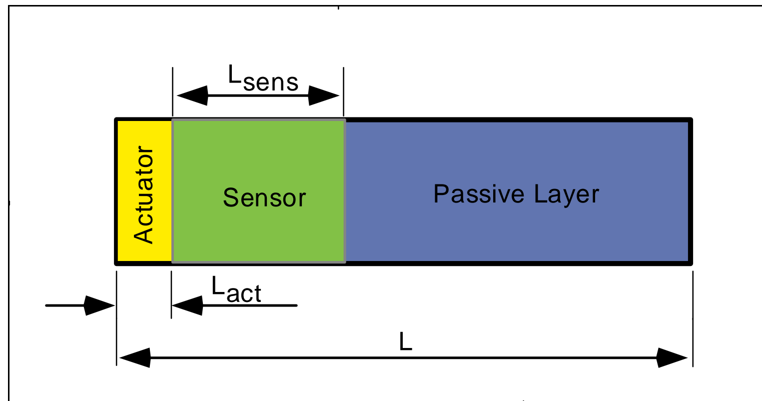

Figure 9. Plan view of the layout of the resonator

Sheets of 127 μm thick aluminum were cut in an Isomet 1000 Precision Saw to form a comb-like structure with 2.3mm wide teeth. The teeth were then cut from the comb structure, forming the resonator substrate layer. An electrode pattern was then etched into the top surface of PZT-5H sheets using ferric chloride, $FeCl_3$ (see Figure 9). This pattern defines the actuator, sensor and passive portions of the resonator. PZT-5H was used for the piezoelectric layer because PZT-5H has nickel electrodes that are easily etched. The electrode in the first three resonators (Resonators PS VIII*, PS XII and PS XIII) is gold sputtered onto the top surface of the PZT. The top surface of the PZT sheets for these three resonators were prepared by completely removing the nickel electrode using ferric chloride. The electrode pattern was then formed by scouring the sputtered gold surface. Problems with the gold sputtering machine meant that a different approach had to be used to form the electrode pattern for the last three resonators; Resonators PS XIV, PS XV and PS XVI. For these resonators the electrode pattern was formed directly in

*PS stands for Precision Saw and indicates the method used in preparing the substrate. Resonators were consecutively numbered after manufacturing. Low working resonator yield is indicated by the gaps in the number sequence.

the nickel electrode using thread soaked in ferric chloride. The piezoelectric layers were then cut to size from the electroded PZT-5H sheets using an X-ACTO knife.

The PZT layer was bonded to the metal substrate using two-part epoxy as the bonding agent. Equal volumes of the two parts of the epoxy were mixed and applied to the contacting surfaces. The two layers were then joined and placed in a clamp. The clamp was used to apply a uniform pressure ensuring that the layers bond in intimate contact. As can be seen in Figure 10, the substrate layer was designed to be slightly longer than the PZT to aid in mounting the cantilever to the clamping device. This metallic substrate was also used as the electrical ground for the system. Leads were attached to the actuator, sensor and passive portions of the PZT using conductive epoxy. Signals derived from the sensor were used to provide actuation using a feedback loop and the lead attached to the passive layer used in frequency tuning.

A set of cantilever beams that were built to the same specification were used to experimentally verify the analytical models developed. The width of the aluminum and PZT-5H layers was 2.3mm and the layer thickness was 127 μm. The PZT layer was approximately 2.1cm long. The length of the actuator section was approximately 5.4mm and the sensor length was 2.7mm.

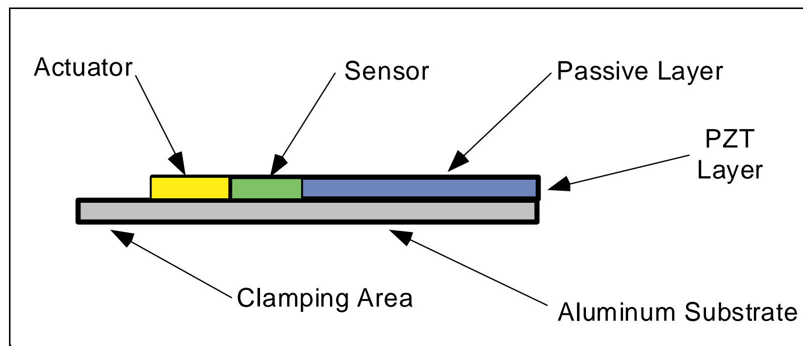

Figure 10. Side view of the layout of the resonator

Every effort was expended to try and produce identical resonators. However, cutting the PZT layers by hand introduced some differences in the length and width of the piezoelectric layers. In addition, the clamping process sometimes introduced displacement and rotation of the piezoelectric layer in relation to the substrate; introducing some layer misalignment. It is expected that these manufacturing issues will manifest themselves in differences in the performance of the resonators.

4.2 MODELING OF THE DESIGNS

A one degree of freedom system was chosen for the analytical model for its simplicity. The one degree of freedom (DOF) system was then analyzed in two ways. Firstly, from equations derived from simple beam theory and then with equations from the Hamiltonian principle as applied to the full electromechanical system (Hagood, 1990). In all derivations, the system is assumed to be a cantilever beam.

4.2.1 One Degree of Freedom Systems

4.2.1.1 *Simple Model from the Beam Equation.* The exact solution for the frequency of vibration of a cantilever beam is (Rao, 1990),

$$\omega = (\beta_n l)^2 \sqrt{\frac{EI}{\rho A L^4}} \tag{4.2-1}$$

where the term $\beta_n l$ is from beam theory and is the constant for the nth natural frequency of the beam derived from the solution to the beam equation. E is the modulus of elasticity, I the mass moment of inertia, ρ the beam material density, A the cross sectional area and L the length of the beam.

The cantilever beam design is a two-ply composite structure. The upper layer is lead zirconate titanate (PZT) and the other layer, to which the PZT is bonded, is metal (aluminum). Since the two materials have different moduli of elasticity, simple application of equation (4.2-1) above is impossible. The mass moment of inertia, I, needs to be calculated from the centroid of the cross section which is no longer simply halfway up through the thickness of the rectangular cross section of the beam.

Since we know that the frequency of vibration of the system is given by,

$$\omega = \sqrt{\frac{k}{m}} \tag{4.2-2}$$

where k is the stiffness and m the mass. Using our two equations, (4.2-1) and (4.2-2), we can write,

$$\begin{aligned} k &= \beta^4 LEI \\ m &= \rho AL \end{aligned} \tag{4.2-3}$$

The contributions of each layer to the stiffness and mass needs to be taken into account and added together before using equation (4.2-2) to find the natural frequency. Calculating the mass contribution from each layer is straightforward since all that is needed are the dimensions and material densities of the layers. To find the mass moment of inertia of the system the centroid of the cross section of the beam needs to be found (Beer, 1992). The first step is to define the following ratio of the moduli of elasticity.

$$n = \frac{E_2}{E_1} \tag{4.2-4}$$

The subscripts refer to the layer number. If the modulus of elasticity of layer two is greater than that of layer one, then the following figure shows the transformation that is done on the section to find the centroid (for the case where the converse is true, the transformation would make the width of layer two smaller than that of the first layer).

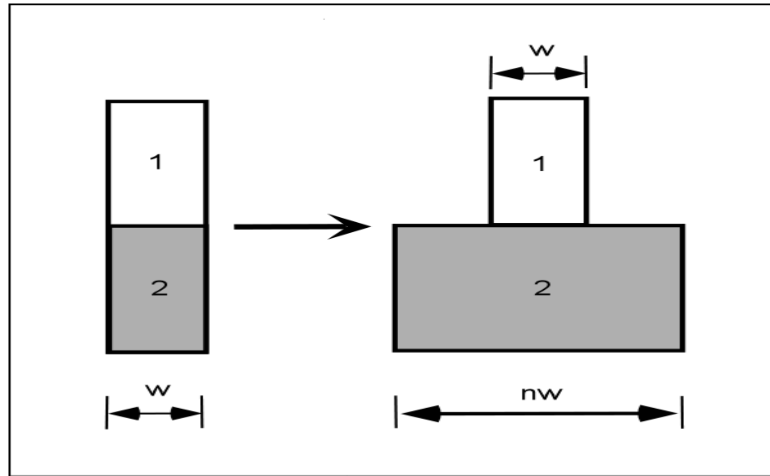

Figure 11. Width transformation in calculation of the centroid

The dimensions of the cross section after the transformation are then used to find the centroidal location by the usual method, i.e.

$$\overline{Y} = \frac{nwh_2\overline{y}_2 + wh_1\overline{y}_1}{nwh_2 + wh_1} \tag{4.2-5}$$

As in Figure 11 above, the original width of the layers is w, and the layer thickness and layer centroid heights are given by h_i and $\overline{y}_i$, respectively (note that the datum for the centroidal heights is the base of the beam). The subscripts, as before, denote the layer that the dimension relates to. The moment of inertia of each layer is then,

$$
\begin{aligned}
I_1 &= I_1' + A_1 d_1^2 = \frac{1}{12} w h_1^3 + w h_1 \left\| \overline{y}_1 - \overline{Y} \right\|^2 \\
I_2 &= I_2' + A_2 d_2^2 = \frac{1}{12} w h_2^3 + w h_2 \left\| \overline{y}_2 - \overline{Y} \right\|^2
\end{aligned}
\qquad (4.2\text{-}6)
$$

The individual moments of inertia, I_1 and I_2; the corresponding moduli of elasticity; and the layer densities can then be used to find the stiffness and mass of the two layer system as follows,

$$
\begin{aligned}
k &= \beta^4 L(E_1 I_1 + E_2 I_2) \\
m &= L(\rho_1 A_1 + \rho_2 A_2)
\end{aligned}
\qquad (4.2\text{-}7)
$$

The above result can then be substituted into equations 4.2-2 and 4.2-3 to find the bending frequencies of operation of the resonator.

4.2.1.2 Shape Functions applied to the Hamiltonian of the Electromechanical System. The generalized Hamiltonian for coupled electromechanical systems (Hagood, 1990) is,

$$
\int_{t_1}^{t_2} \left\{ \partial(T - U + W_e - W_m) + \partial W \right\} dt = 0 \qquad (4.2\text{-}8)
$$

where,

$$
\begin{aligned}
T &= \int_{V_{SUBSTRATE}} \frac{1}{2} \rho_s \dot{u}^T \dot{u} + \int_{V_{PIEZO}} \frac{1}{2} \rho_p \dot{u}^T \dot{u} \\
U &= \int_{V_{SUBSTRATE}} \frac{1}{2} S^T T + \int_{V_{PIEZO}} \frac{1}{2} S^T T \\
W_e &= \int_{V_{PIEZO}} \frac{1}{2} E^T D \\
W_m &\approx 0 \\
\partial W &= \sum_i \partial u(x_i) \bullet f(x_i) - \sum_j \partial \phi_j \bullet q_j
\end{aligned}
\qquad (4.2\text{-}9)
$$

T and U are the kinetic and potential energies, and W_e and W_m are electrical and magnetic energies. W is the work associated with the forces, f_i, and charges, q_j , applied at the beam

positions x_i and x_j, respectively. Displacement and velocity are u and $\dot{u}$. The density of the material is ρ, with subscript s for the substrate layer and p for the piezoelectric. S and T are the material strain and stress matrices, and E and D are the matrices for the electrical field and electrical displacement. ϕ is the scalar electrical potential. The superscript T denotes the transpose. Matrices and matrix values are denoted by capitalization.

For piezoelectric materials we can write,

$$\begin{bmatrix} D \\ T \end{bmatrix} = \begin{bmatrix} \varepsilon_S & e \\ -e^T & c^E \end{bmatrix} \begin{bmatrix} E \\ S \end{bmatrix} \tag{4.2-10}$$

In the above equation ε_S is the matrix of dielectric constants, e the piezoelectric material constant relating electrical displacement and strain, and c^E is the constant electrical field mechanical stiffness. D, E, S and T are the electrical displacement, electric field, mechanical strain and mechanical stress respectively (IEEE Std 176-1987). Solving Equation 4.2-9 for the mechanical strain, S, gives us Equation 2.3-1. Displacement and electrical potentials on the piezoelectric that are functions of both position and time can be defined such that,

$$\begin{aligned} u(x,t) &= \psi_r(x) r(t) \\ \phi(x,t) &= \psi_V(x) v(t) \end{aligned} \tag{4.2-11}$$

then for a differential operator, L_u, and gradient operator, L_ϕ,

$$\begin{aligned} S &= L_u u(x,t) = L_u \psi_r(x) r(t) = N_r(x) r(t) \\ E &= L_\phi \phi(x,t) = L_\phi \psi_V(x) v(t) = N_V(x) v(t) = -\nabla \psi_V(x) v(t) \end{aligned} \tag{4.2-12}$$

For the substrate (which is not a piezoelectric material), equation (4.2-10) reduces to,

$$T = c_S S \tag{4.2-13}$$

where c_S is the constant mechanical strain mechanical stiffness.

In the Hamiltonian the kinetic and potential energy terms including contributions from the two layers in the system are,

$$\begin{aligned} \partial T &= \int_{V_{SUBSTRATE}} \rho_S \partial \dot{u}^T \dot{u} + \int_{V_{PIEZO}} \rho_P \partial \dot{u}^T \dot{u} \\ \partial U &= \int_{V_{SUBSTRATE}} \partial S^T c_S S + \int_{V_{PIEZO}} \partial S^T c^E S - \frac{1}{2}\left\{ \partial S^T e^T E + S^T e^T \partial E \right\} \end{aligned} \tag{4.2-14}$$

The electrical energy is,

$$\partial W_E = \int_{V_{PIEZO}} \partial E^T \varepsilon^S E + \frac{1}{2}\left\{ \partial E^T e S + E^T e \partial S \right\} \tag{4.2-15}$$

Integration of the Hamiltonian gives,

$$\int_{t_1}^{t_2} \left\{ \begin{aligned} & \int_{V_{SUBSTRATE}} [-\rho_S \ddot{u} \partial u - \partial S^T c_S S] + \\ & \int_{V_{PIEZO}} [-\rho_P \ddot{u} \partial u - \partial S^T c^E S + \partial S^T e^T E + \partial E^T e S + \partial E^T \varepsilon^S E] \\ & + \sum_i \partial u_i \bullet f_i + \sum_j \partial \phi_j \bullet q_j \end{aligned} \right\} dt = 0 \tag{4.2-16}$$

If the following substitutions are used,

$$\begin{aligned} u &= \psi_r r \\ S &= N_r r \\ E &= N_v v = -\nabla \psi_v v \end{aligned} \tag{4.2-17}$$

then equations (4.2-16) become,

$$\int_{t_1}^{t_2}\left\{\begin{array}{c}\int\limits_{V_{SUBSTRATE}}[-\rho_S\psi_r^2\ddot{r}\partial r - N_r^T c_S N_r r\partial r]+\\ \int\limits_{V_{PIEZO}}[-\rho_P\psi_r^2\ddot{r}\partial r - N_r^T c^E N_r r\partial r + N_r^T e^T N_v v\partial r + N_v^T e N_r^T r\partial v + N_V^T \varepsilon^S N_v v\partial v]\\ +\sum_i \psi_{r_i}\bullet f_i\partial r - \sum_j \psi_{v_j}\bullet q_j\partial v\end{array}\right\}dt = 0 \quad (4.2\text{-}18)$$

In equation 4.2-11, r and v are defined as functions of only time. Consequently, it follows that the variations of r and v are also only dependent on time. This means that the volume integrals in equation 4.2-18 can be evaluated. Defining the volume integrals as follows,

$$\begin{aligned}M_S &= \int\limits_{V_{SUBSTRATE}}\rho_S\psi_r^2\\ M_P &= \int\limits_{V_{PIEZO}}\rho_P\psi_r^2\\ K_S &= \int\limits_{V_{SUBSTRATE}}N_r^T c_S N_r\\ K_P &= \int\limits_{V_{PIEZO}}N_r^T c^E N_r\\ C_P &= \int\limits_{V_{PIEZO}}N_V^T\varepsilon^S N_V\\ \theta &= \int\limits_{V_{PIEZO}}N_r^T e^T N_V\end{aligned} \quad (4.2\text{-}19)$$

gives,

$$\begin{aligned}&\int_{t_1}^{t_2}-\left\{(M_S+M_P)\ddot{r}+(K_S+K_P)r-\sum_i\psi_{r_i}\bullet f_i-\theta v\right\}\partial r\cdot dt+\\ &\int_{t_1}^{t_2}\left\{\theta^T r + C_P v - \sum_j\psi_{v_j}\bullet q_j\right\}\partial v\cdot dt = 0\end{aligned} \quad (4.2\text{-}20)$$

M_S and M_P are mass matrices for the substrate and piezoelectric layers respectively, K_S and K_P are the stiffness matrices, C_P is the matrix of piezoelectric capacitance, and θ is the piezoelectric

electromechanical coupling matrix. From the equation above the equations of motion for the coupled electromechanical system are,

$$
\begin{aligned}
(M_S + M_P)\ddot{r} + (K_S + K_P)r &= \sum_i \psi_{r_i} \bullet f_i + \theta v \\
\theta^T r + C_P v &= \sum_j \psi_{v_j} \bullet q_j
\end{aligned}
\qquad (4.2\text{-}21)
$$

or using input matrices, B_f and B_q, for the applied forces and charges,

$$
\begin{aligned}
(M_S + M_P)\ddot{r} + (K_S + K_P)r &= B_f f + \theta v \\
\theta^T r + C_P v &= B_q q
\end{aligned}
\qquad (4.2\text{-}22)
$$

Equation 4.2-22 gives the equations of motion for the coupled electromechanical system from which the frequency of the bending modes of vibration, tuning range and resonator feedback gain can be obtained. The analytical models developed to obtain these values use equation 4.2-22 as a basis. The following chapters will present these models in detail.

5.0 BENDING FREQUENCIES OF VIBRATION

In this chapter and consequent chapters we shall, in turn, look at the experimental and analytical results for bending frequency of vibration, tuning range, feedback gain, and reactance and resonator operating frequencies.

5.1 ANALYTICAL MODEL

The beam design has three distinct sections of piezoelectric material as determined by the electrode pattern. Each of these sections has its particular electromechanical coupling and capacitance. From equation 4.2-21 we can partition θ , C_P and v accordingly, which gives,

$$\begin{bmatrix} \theta^A \\ \theta^S \\ \theta^P \end{bmatrix} r + \begin{bmatrix} C^A & 0 & 0 \\ 0 & C^S & 0 \\ 0 & 0 & C^P \end{bmatrix} \begin{Bmatrix} v^A \\ v^S \\ v^P \end{Bmatrix} = B_q \begin{bmatrix} q^A \\ q^S \\ q^P \end{bmatrix} \tag{5.1-1}$$

The superscripts define the three different sections, namely, the actuator, sensor and passive portions of the piezoelectric. Note that the subscripts on the capacitance have been dropped since the capacitance is calculated only in the piezoelectric material. No external charge is applied to the passive section of the piezoelectric so,

$$\begin{aligned} & q_P = 0 \\ & \Rightarrow \theta^P r + C^P v^P = 0 \\ & \therefore v^P = -(C^P)^{-1} \theta_P r \end{aligned} \tag{5.1-2}$$

The above equation gives the voltage on the passive portion of the beam as a function of tip displacement, *r*. Partitioning the equations of motion in equation 4.2-21 and applying the result above,

$$
\begin{aligned}
(M_S + M_P)\ddot{r} + (K_S + K_P)r &= B_f f + \begin{bmatrix} \theta^A & \theta^S & \theta^P \end{bmatrix} \begin{Bmatrix} v^A & v^S & v^P \end{Bmatrix}^T \\
(M_S + M_P)\ddot{r} + (K_S + K_P)r &= B_f f + \begin{bmatrix} \theta^A & \theta^S \end{bmatrix} \begin{Bmatrix} v^A \\ v^S \end{Bmatrix} + \theta^P v^P \\
(M_S + M_P)\ddot{r} + (K_S + K_P)r &= B_f f - \theta^{P^T} C^{p^{-1}} \theta^P r + \begin{bmatrix} \theta^A & \theta^S \end{bmatrix} \begin{Bmatrix} v^A \\ v^S \end{Bmatrix}
\end{aligned}
\tag{5.1-3}
$$

Equation 5.1-3 can be rearranged to give the following form,

$$
(M_S + M_P)\ddot{r} + (K_S + K_P + \theta^{P^T} C^{p^{-1}} \theta^P)r = B_f f + \begin{bmatrix} \theta^A & \theta^S \end{bmatrix} \begin{Bmatrix} v^A \\ v^S \end{Bmatrix} \tag{5.1-4}
$$

where the term associated with the passive portion of the piezoelectric material has been moved from the right hand side of the equation (associated with the inputs) to the left hand side (associated with our degree of freedom). For a single mode of a one degree of freedom system it can be seen that the frequency of vibration associated with this degree of freedom is,

$$
\omega = \sqrt{\frac{k_S + k_P + \theta^{P^T} c^{p^{-1}} \theta^P}{m_S + m_P}} = \sqrt{\frac{k_S + k_P + c^{p^{-1}} \theta^{P^2}}{m_S + m_P}} \tag{5.1-5}
$$

since the stiffness, capacitance and mass terms are now scalars. The multi-modal frequencies of vibration are found from the solution of the eigenvalue problem,

$$
\omega^2 (M_S + M_P) r = (K_S + K_P + \theta^{P^T} C^{p^{-1}} \theta^P) r \tag{5.1-6}
$$

In our model, solution of equation 5.1-6 gives us our bending frequencies of vibration.

5.2 EXPERIMENTAL SETUP

System identification was performed from the frequency response function of the resonator. Bending type frequencies of vibration were identified in the frequency response functions by comparison to the analytical model results.

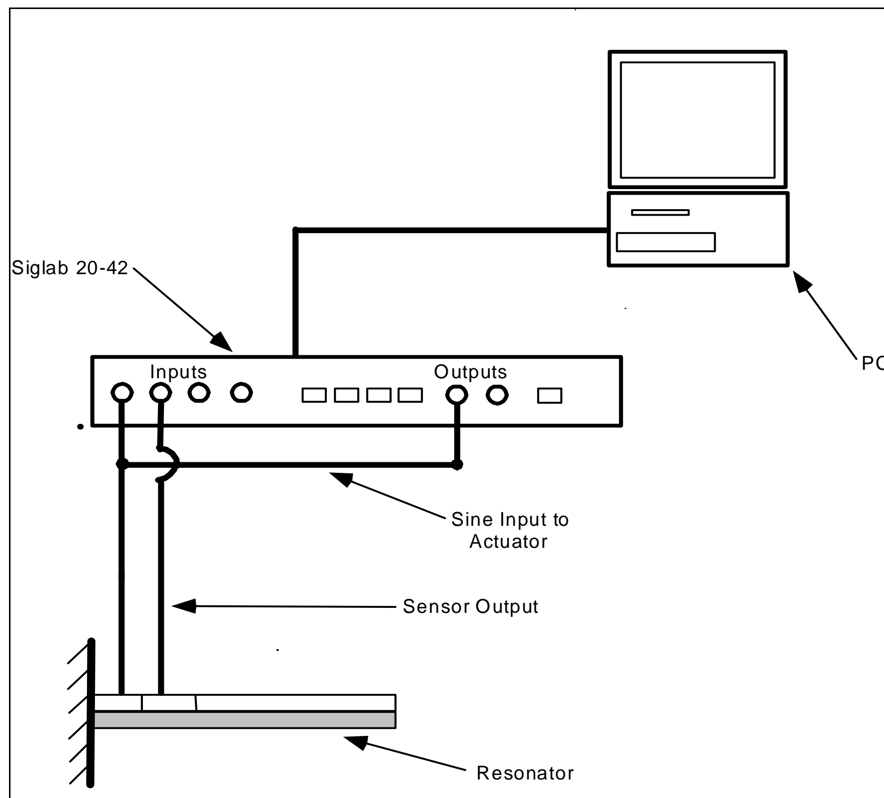

Figure 12. Frequency response measurement experimental setup

A DSP Technology, Inc. SigLab™ Model 20-42 Dynamic Signal and System Analyzer was used to undertake a swept sine input to the actuator. The output of the sensor was then compared to the actuator input and a frequency response function was generated by the signal analysis software in SigLab, which interfaces with Matlab®. The sine input was stepped from 1 Hz to 20 kHz. An inter-step delay was utilized to improve the quality of the measurement through

minimization of the effects of transients. At each step or frequency data point, 4 averages were taken. The experimental setup is shown pictorially in Figure 12.

5.3 COMPARISON OF ANALYTICAL AND EXPERIMENTAL RESULTS

The first eight displacement shape functions from the exact solution to the Bernoulli-Euler fixed-free beam were used to generate the mass and stiffness matrices of the beam in MathCAD. Figure 13 is a plot of these shape functions for a beam of unit length. Similarly, the displacement of the shape functions has also been normalized. The displacement shape functions used in the development of all the analytical models are orthogonal. Hence, the matrices in the equations of motion, equation 5.1-6, used in finding the frequencies of vibration of the system are approximately diagonal.

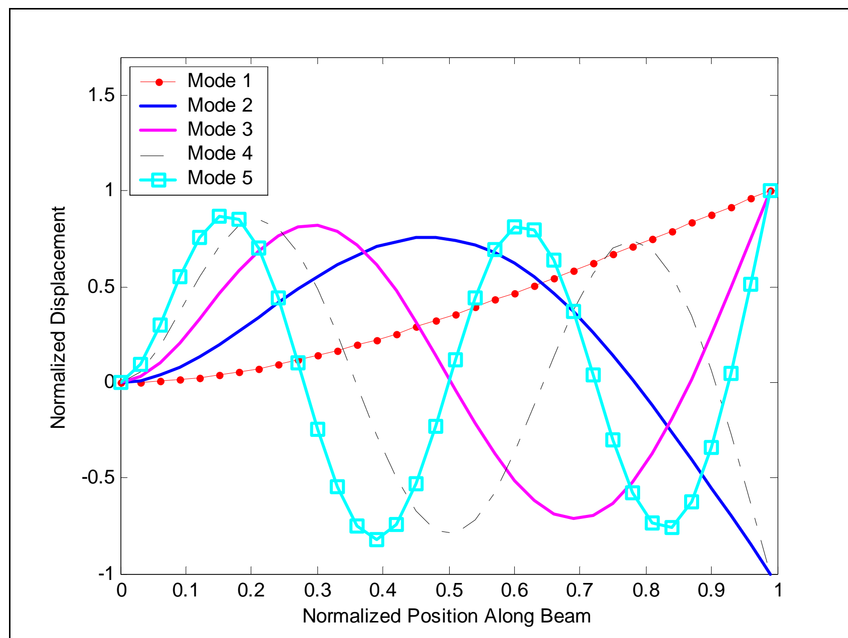

Figure 13. First five displacement mode shapes

Using the material properties for the PZT and the substrate layers, Table 3, the MathCAD model was used to find the first eight bending mode frequencies of vibration for the beams (Table 4).

Table 3. Table of material properties used in the model

Property	PZT-5H	Aluminum
Density (kg/m^3)	7700	2800
Elastic Modulus	50 GPa	79 GPa
Thickness	125 μm	125 μm
Length	2.1cm	>2.1cm
Width	2.3mm	2.3mm
Relative Dielectric constant	3800	
Piezoelectric Strain coefficient	-320×10^{-12}	

The MathCAD data in Table 4 shows that the first five bending modes of vibration are predicted to be under 20kHz. The SigLab used in experiment has a bandwidth of 20kHz and so was used for identification of the bending modes of the beams.

Table 4. Frequency of vibration from MathCAD

Mode Number	Calculated Frequency (Hz)
1	269
2	1687
3	4723
4	9255
5	15300
6	22850
7	31920
8	42500

The frequency response of beams PS XII and PS XVI to 10kHz to sinusoidal excitation from zero hertz to ten kilohertz is shown in Figure 14. Although the two resonators, PS XII and PS XVI, are built to the same specification, it can be seen that there are differences in the frequency responses. The differences that are apparent in magnitude of the response as well as location of peaks and troughs in response are due to repeatability problems in the manufacturing process.

The experimental bending frequency is taken to be the largest peak in the frequency response in the vicinity of the analytically calculated frequency of vibration. The analytical bending mode frequencies of vibration are compared to the experimental values in Table 5. Two values are given for mode number 1 frequency of vibration for resonator PS XII and mode 3 of PS VIII because the peaks at those frequencies are of approximately equal magnitude.

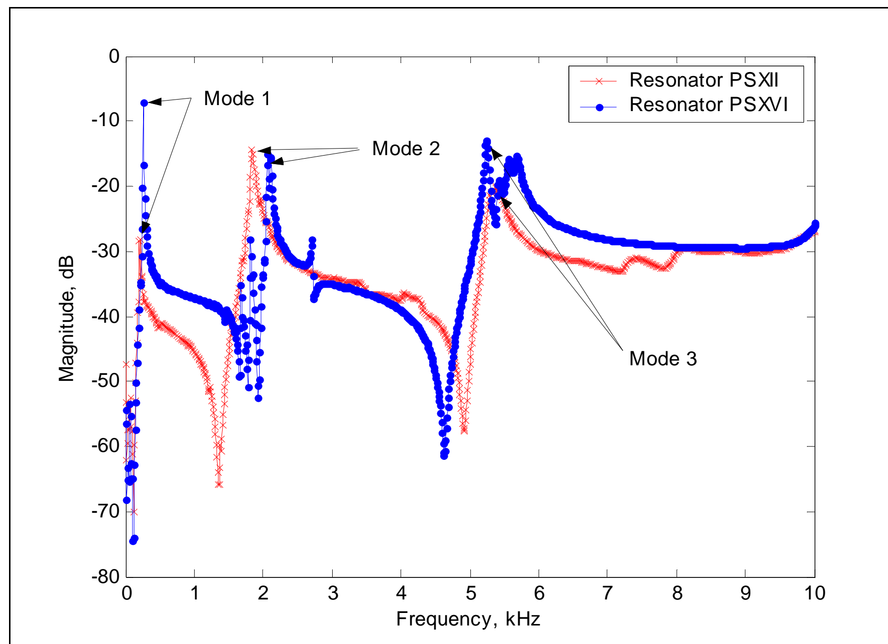

Figure 14. Frequency response for beams PS XII and PS XVI to 10kHz

Table 5. Experimental and analytical bending mode frequencies

Mode Number	Calculated Frequency (Hz)	Experimental Frequency (Hz)					
		PS VIII	PS XII	PS XIII	PS XIV	PS XV	PS XVI
1	269	261	185/352	250.8	226.25	164.5	268
2	1687	1609	1897	1740	1732	1781	2109
3	4723	4655/4952	5530	4870	5074	4999	5238
4	9255	9488	10770	9320	9311	11317	9998
5	15300	16000	16130	15570	15487	15184	18445

The frequency responses of the six resonators from zero hertz to ten kilohertz, and from ten kilohertz to the maximum frequency of the SigLab equipment are shown in Figure 15 to Figure 18.

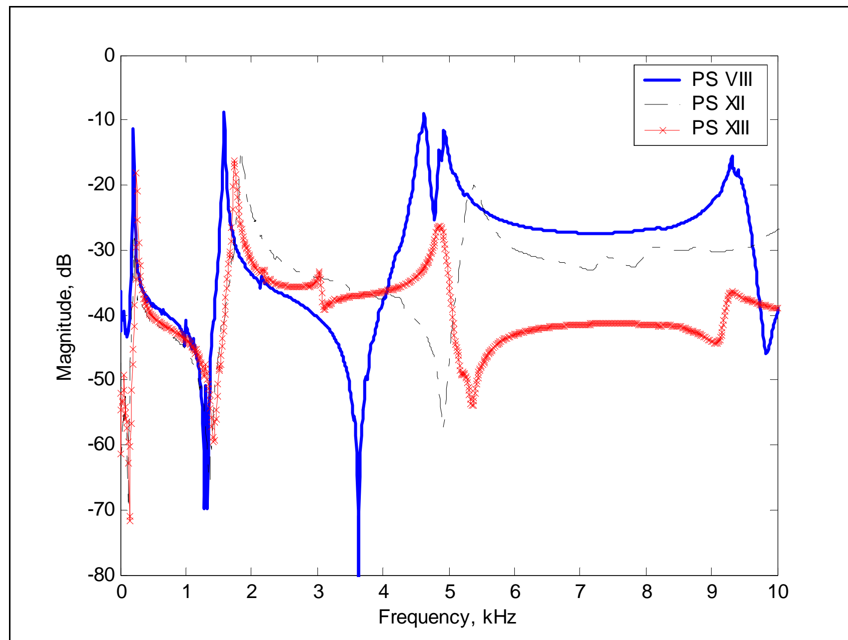

Figure 15. Frequency response to 10kHz for PS VIII, PS XII and PS XIII

If we think of the frequency response in terms of poles and zeros in the transfer function from the actuator to sensor voltage, then it can be seen in Figure 15 that below about two kilohertz there is little difference between the resonators. At approximately three kilohertz, there is a pole in PS XIII that is not apparent in the responses for PS XII and VIII. In addition, the zero near the pole at five kilohertz appears after the pole in only the resonator PS XIII response. Looking at Figure 15 and Figure 16 we can see that this reversal occurs again in the pole and zero positions near 10kHz with a PS XIII zero before the pole. Figure 16 also shows that the PS XII pole is at a higher frequency then the PS VIII and PS XIII poles.

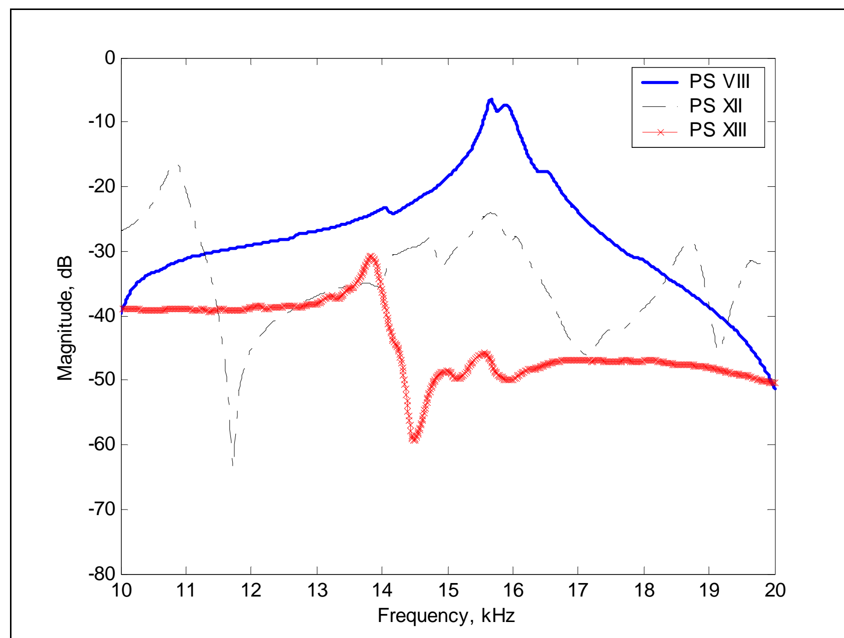

Figure 16. Frequency response from 10 to 20kHz for PS VIII, PS XII and PS XIII

In Figure 16 the pole associated with mode 5 bending vibration appears at just below 16kHz for PS VIII and about 14kHz for PS XIII. The zeros associated with these poles are at just over 14kHz and at over 20kHz for PS XIII and PS VIII respectively. From the PS XII response the peak between 15kHz and 16kHz is the best guess for the location of the fifth bending mode.

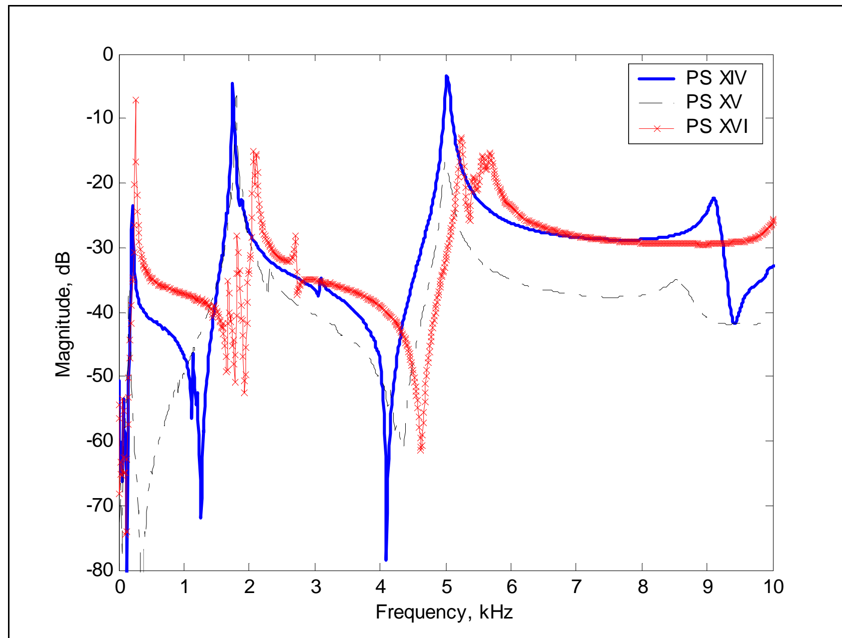

Figure 17. Frequency response to 10kHz for PS XIV, PS XV and PS XVI

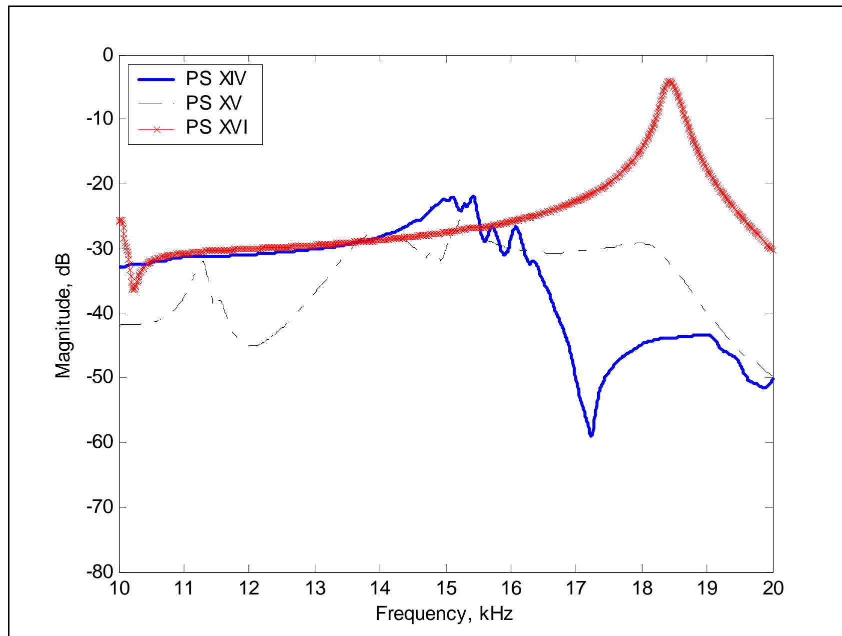

Figure 18. Frequency response from 10 to 20kHz for PS XIV, PS XV and PS XVI

Figure 17 shows that the poles and zeros associated with PS XVI are at slightly higher frequencies than poles and zeros of PS XIV and PS XV. The flattened peaks in the response of PS XV suggest that the resonator has higher damping than the other two resonators. This can

be seen especially when talking about mode 4 at about 9kHz (Figure 17) and mode 5 at about 15kHz (Figure 18). In keeping with the data for the response below 10kHz, mode 5 in PS XVI is at about 18kHz which is higher than the response for resonators PS XIV and PS XV, indicating that PS XVI is slightly stiffer than PS XIV and PS XV.

5.4 SUMMARY

The experimental and analytical frequencies are closer at the higher mode numbers. For mode 5, five out of six of the experimental values are within ten percent of the analytically calculated frequency of vibration. For modes 2, 3 and 4, three quarters of the analytical values are within ten percent. The lowest frequency mode, mode 1, has only half of the experimental frequency values within ten percent of the analytical values.

The differences in stiffness and damping that can be observed within the batch of resonators built are due to problems in manufacturing identical resonators by hand.

6.0 TUNING RANGE

6.1 ANALYTICAL MODEL

Equations 5.1-5 and 5.1-6 are reproduced below,

$$\omega = \sqrt{\frac{k_S + k_P + \theta^{P^T} c^{p^{-1}} \theta^P}{m_S + m_P}} = \sqrt{\frac{k_S + k_P + c^{p^{-1}} \theta^{P^2}}{m_S + m_P}} \tag{6.1-1}$$

$$\omega^2 (M_S + M_P) r = (K_S + K_P + \theta^{P^T} C^{p^{-1}} \theta^P) r \tag{6.1-2}$$

In these two equations the product of the square of the electromechanical coupling and the inverse of the capacitance associated with the passive portion of the piezoelectric appears as a stiffness term in the equation for the frequency of vibration. The three stiffness terms, i.e. the stiffness of the substrate, PZT and this coupling-capacitance product, combine in a parallel manner as shown in Figure 19. The product of electromechanical coupling and capacitance is what allows tuning of the frequency of vibration. Altering the electromechanical coupling or the capacitance of the passive portion of the piezoelectric can change the stiffness of the system and the frequency of vibration. Since the coupling is set by the electrode placement and size, real-time changes in frequency are only possible through manipulation of the capacitance.

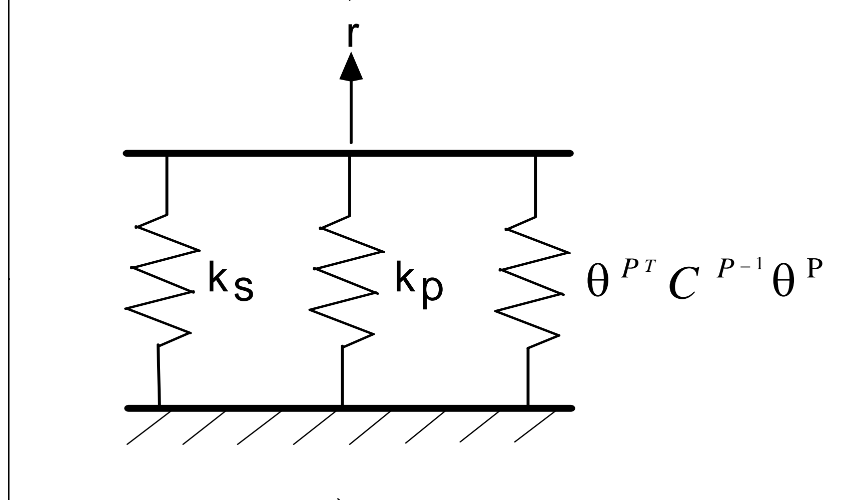

Figure 19. Parallel stiffnesses in the resonator

In this work the electromechanical coupling-capacitance product is altered by way of a capacitive shunt. The shunt is placed in electrical parallel with the capacitance of the passive portion of the piezoelectric layer (see Figure 20). Since the capacitances are in parallel, the total capacitance seen by the system is given by the sum of the shunt capacitance and the piezoelectric layer capacitance. If the electrical shunt is left as an open circuit, the capacitance is simply that of the passive portion. When the electrodes are short circuited, the capacitance of the passive portion is zero. Equation 5.1-2 is reproduced below.

$$\begin{aligned} q_P &= 0 \\ \Rightarrow \theta^P r + C^P v^P &= 0 \\ \therefore v^P &= -(C^P)^{-1} \theta_P r \end{aligned} \tag{6.1-3}$$

If the capacitance, C^P is zero, then the coupling-capacitance terms no longer appear in the stiffness terms in the equations of motion. Thus, the short circuit and open circuit stiffness values define the limits of our tuning.

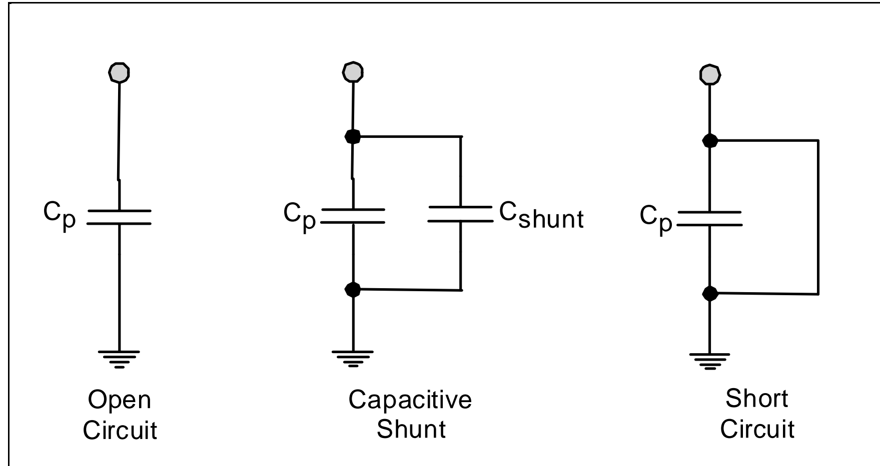

Figure 20. Electrical shunting of the passive layer capacitance

The third option is to apply a capacitor in parallel with the passive portion of the piezoelectric layer. As shown in Equation 6.1-4 this produces a total electrical capacitance larger than the passive layer value.

$$\begin{gathered} C^T = (C^P + C) > C^P \\ \therefore \theta^{P^T} C^{P^{-1}} \theta^P > \theta^{P^T} C^{T^{-1}} \theta^P \end{gathered} \tag{6.1-4}$$

Since the reciprocal of this value appears in the equations, the effect of the shunt is to reduce the effect of the electromechanical coupling on the system. In effect, producing an intermediate "stiffness" that is between the open and short circuit stiffnesses. Continuously varying the shunt capacitance therefore would, in principle, allow any frequency between the open and short circuit frequencies of vibration to be obtained.

Maximizing the tuning range of the resonators can be achieved by either increasing the electromechanical coupling of the passive section of the PZT layer, reducing the capacitance of the passive section, or by both increasing the coupling and reducing the capacitance.

The dimensions of the piezoelectric and the shape and position of the electrode on the beam sets the electromechanical coupling and therefore the coupling is difficult to change after the beam has been built. However, clever selection of the position and dimensions of the passive portion can maximize the value of the coupling for selected modes of vibration.

The electromechanical coupling of the passive portion of the resonator, Equation 6.1-5, is the volume integral of the product of the displacement and voltage shape functions and the piezoelectric material constant, e^T. The displacement shape function varies in value both along the length of the beam and from mode to mode. In theory, for a particular mode a position can be found on the beam that maximizes the value of the electromechanical coupling. This position on the beam may be sub-optimal for maximizing the coupling for a different mode and so differences in tuning range from mode to mode should occur.

$$\theta^P = \int_{V^P_{PIEZO}} N_r^T e^T N_V \tag{6.1-5}$$

As seen in Section 2.3 the piezoelectric material matrix of constants, e^T, also governs the suitability of the shunt tuning method to differing types of vibration. For PZT, the matrix of piezoelectric material constants is,

$$e = \begin{bmatrix} 0 & 0 & 0 & 0 & e_{15} & 0 \\ 0 & 0 & 0 & e_{15} & 0 & 0 \\ e_{31} & e_{31} & e_{33} & 0 & 0 & 0 \end{bmatrix} \tag{6.1-6}$$

where the columns correspond to the following strains (IEEE Std 176-1987),

$$\varepsilon = \begin{bmatrix} \varepsilon_{11} & \varepsilon_{22} & \varepsilon_{33} & \varepsilon_{23} & \varepsilon_{31} & \varepsilon_{12} \end{bmatrix} \tag{6.1-7}$$

The rows in Equation 6.1-6 correspond to an applied charge on the surfaces defined relative to the poling direction. The third row is the poling axis. From equations 6.1-6 and 6.1-7 if a charge is applied on the surface perpendicular to the poling direction, we obtain equal strains in the two axes that are perpendicular to the poling direction as well as a strain in the poling direction. Different vibration types produce different strains in the piezoelectric material. Using e a determination can be made of both the possibility of using the tuning method for different vibration types (from the population of the matrix), and the relative effectiveness of the tuning (from the relative values of the constants, e_{ij}).

For example, if we electrode the z-surface (the surface perpendicular to the poling axis) application of a charge will produce strains in the three axis directions when the piezoelectric material is not constrained. These three unconstrained strains will produce a longitudinal vibration device with three frequencies of vibration determined by the dimensions and material properties in the three axis directions. The material properties determine the strain wave velocity and the dimensions in the axis directions the time for the strain wave to travel between the edges of the material. If, as we have done in this work, we constrain one of the z-surfaces by gluing it to a substrate layer or by holding the lower surface at ground potential (which through the coupling afforded by the piezoelectric effect is equivalent), the applied charge causes a strain in the top surface that is different from the lower surface inducing bending in the transverse direction (rotations around both the x and y axes) and extension in the plane of the electrode.

As shall be seen in the next section on feedback gain, the actuator and sensor portions of the resonator were chosen to minimize electrode area and required feedback gain. The passive

portion of the resonator was then the leftover piezoelectric material surface area. No attempt was made to optimize the tuning range by placing the passive electrode such that the electromechanical coupling is maximized and the capacitance is minimized. The capacitance and electromechanical coupling for each bending mode was analytically calculated and used to determine the tuning range of our cantilever beams.

6.2 EXPERIMENTAL SETUP

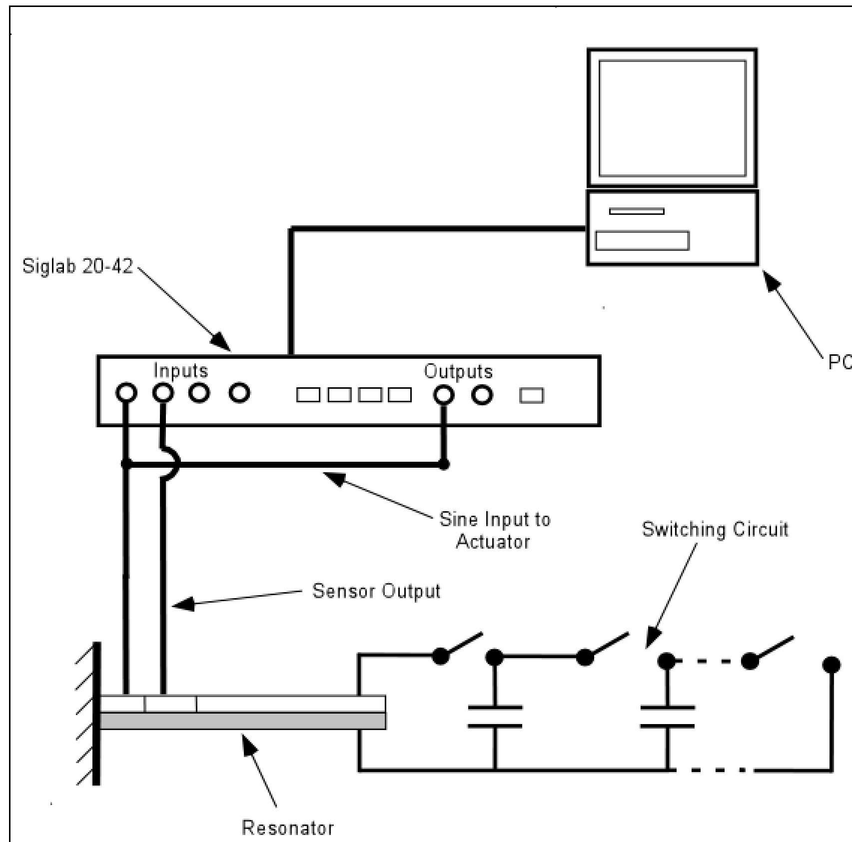

Figure 21. Tuning range measurement experimental setup

Shunt tuning data was obtained using the SigLab setup shown in Figure 21. The leads on the passive portion of the resonator were then connected either as an open circuit, a short circuit or

shunted with various capacitors. Data was taken using the same settings for excitation level and inter-step delay used in the frequency response measurements. Around the bending modes of vibration, additional data was taken with smaller frequency steps in the stepped sine input to improve the resolution of the data.

6.3 COMPARISON OF ANALYTICAL AND EXPERIMENTAL RESULTS

The analytical model developed for the beams was used to calculate the change in frequency that would be obtained from our designs. The tuning range shown in Table 6 is the difference between the frequency of vibration of the beam with and without the added stiffness provided by the shunt on the passive portion of the beams, i.e. the difference between the open and short circuit frequencies of vibration.

Table 6. Theoretical tuning ranges from analytical model

Mode Number	**Analytical Model**	
	$\Delta\omega$ (Hz)	$\frac{\Delta\omega}{\omega_i}$ %
1	0.62	0.002
2	24.2	1.4
3	33.4	0.71
4	1.65	0.018
5	15.9	0.1
6	42.5	0.19
7	4.44	0.014
8	15.9	0.004

SigLab was used to determine the frequency response of the resonators below 20kHz. The frequency difference in peak responses between the open and short circuit were used to determine the experimental tuning range. Table 7 summarizes the experimentally observed and analytically calculated tuning range of the resonators. In some cases the short circuit frequency was higher than open circuit frequency producing the negative values in Table 7. This result is counter to expectations since shorting the passive region reduces the stiffness of the resonator and, consequently, reduces the frequency of vibration of a particular mode. Three of the six resonators, i.e. PS VIII, PS XIV and PS XV exhibited this behavior. An explanation for this anomaly is given in the Summary section, Section 6.4.

Table 7. Comparison of tuning range from SigLab and analytical data

Mode Number	Analytical Frequency Change (Hz)	Experimental Change in Frequency (Hz)					
		PS VIII	PS XII	PS XIII	PS XIV	PS XV	PS XVI
1	0.62	0.3	2/2	0	0.25	-1.75	1.75
2	24.2	-5.5	13	10	1	-5	12
3	33.4	-3.6/-9	55	50	2	3.5	15
4	1.65	-4	0	90	9	5	2
5	15.9	-7	20	130	-21	20	43

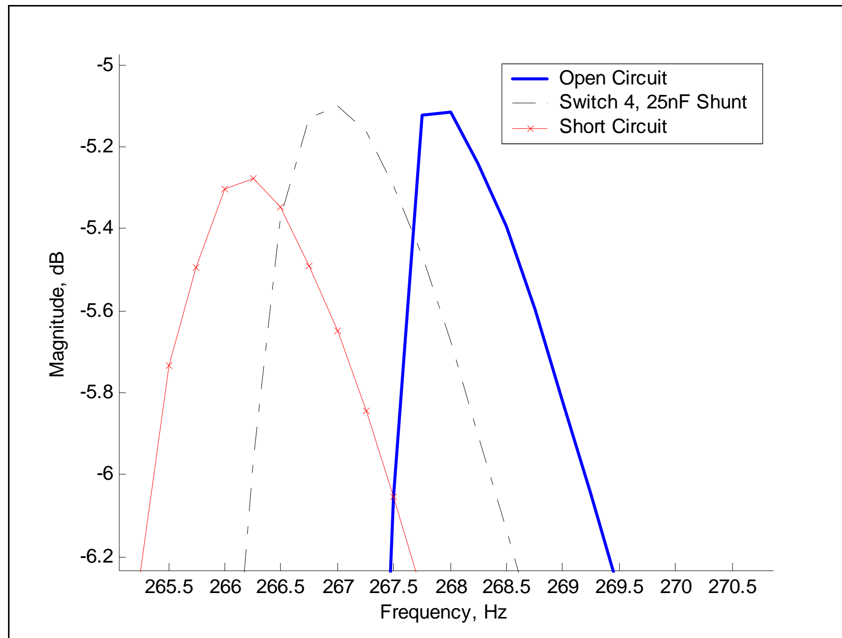

Figure 22. Changes in frequency response near mode 1, PS XVI

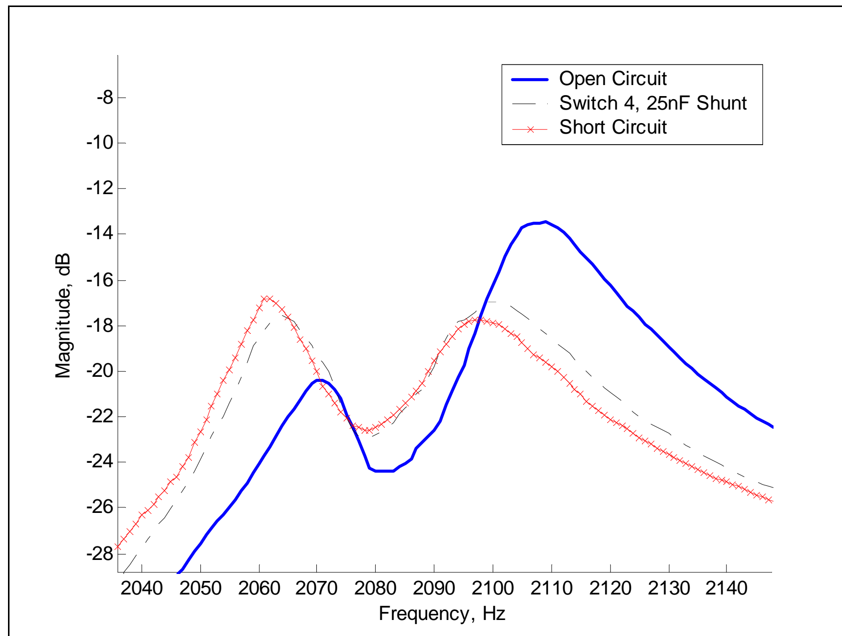

Figure 23. Changes in frequency response near mode 2, PS XVI

Figure 22 and Figure 23 show resonator PS XVI data obtained from SigLab for bending modes one and two. Three switch conditions are shown; open circuit, short circuit and a 25nF capacitive shunt (to obtain an intermediate frequency of vibration). The two figures show that

changing the switch condition on the passive portion of the resonator affects the frequency and magnitude of the peak in the frequency response.

Figure 24 to Figure 26 show the effect of switching on the frequency response of beam PS XVI for modes three to five. Changes in frequency and magnitude are readily observable in modes three and five. There is not much observed change in the frequency or magnitude of mode four. From Table 7 the expected change in frequency is only approximately two hertz, indicating that for mode four the electromechanical coupling is weaker than, for example, coupling to mode three.

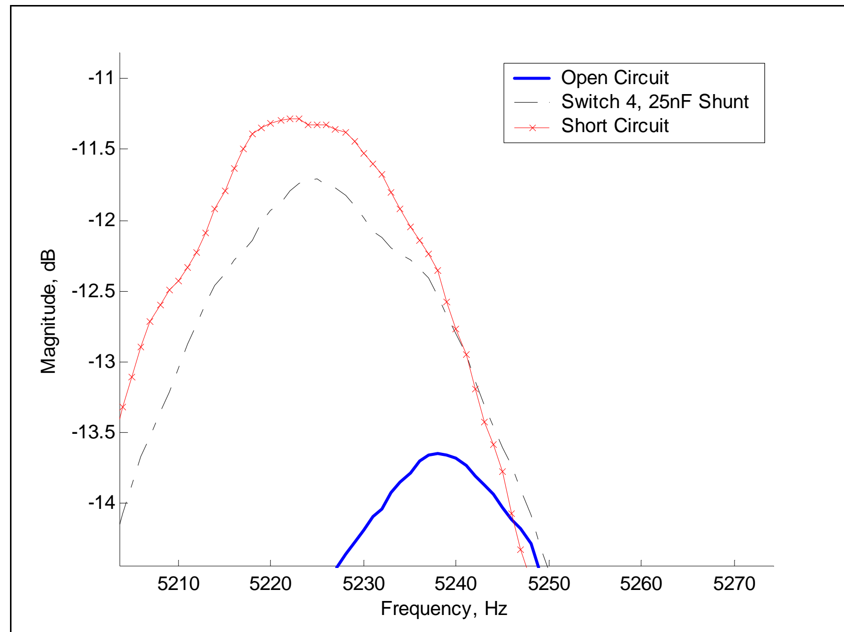

Figure 24. Changes in frequency response near mode 3, PS XVI

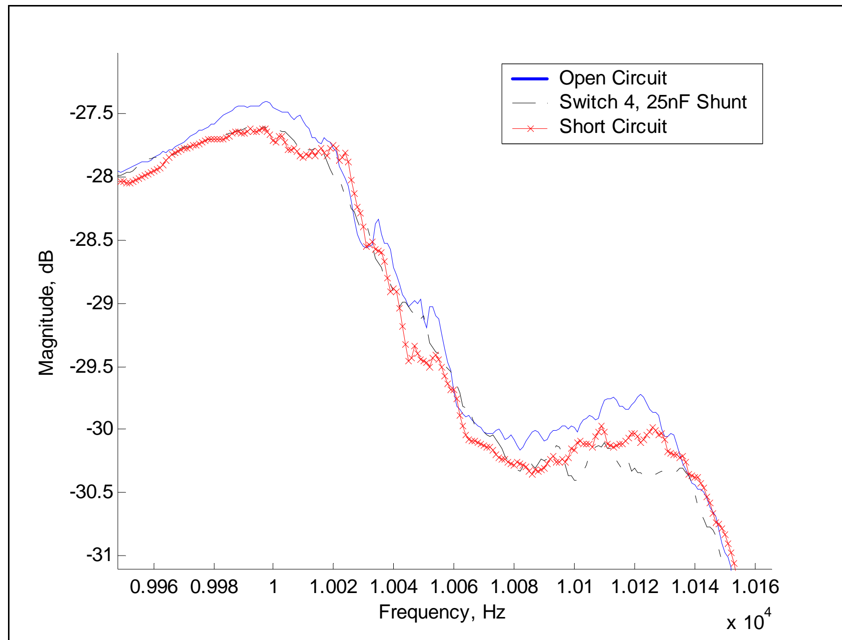

Figure 25. Changes in frequency response near mode 4, PS XVI

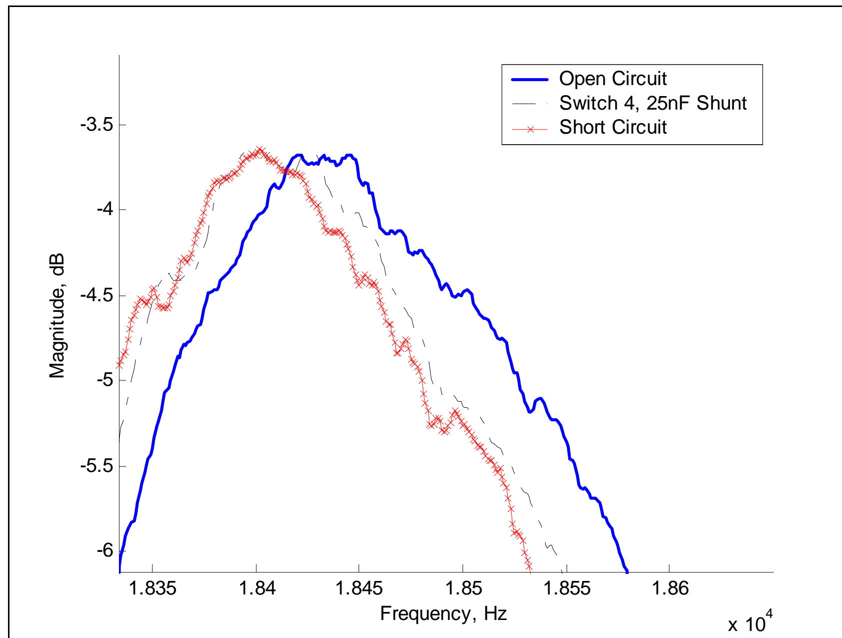

Figure 26. Changes in frequency response near mode 5, PS XVI

Figure 27 to Figure 41 are show the changes in frequency response due to switching of the passive portion of resonators PS VIII, PS XII, PS XIII, PS XIV and PS XV. In Figure 27 the change in frequency for resonator PS VIII from holding the passive portion open circuited to

short circuiting the passive layer is clear for mode 1. The PS VIII mode 2 plot (Figure 27) shows how the switching does not always cause an observable shift in the peak response frequency. Since we define the frequency of the mode to be at the peak in the frequency response, the short circuit frequency is said to be higher than the open circuit frequency.

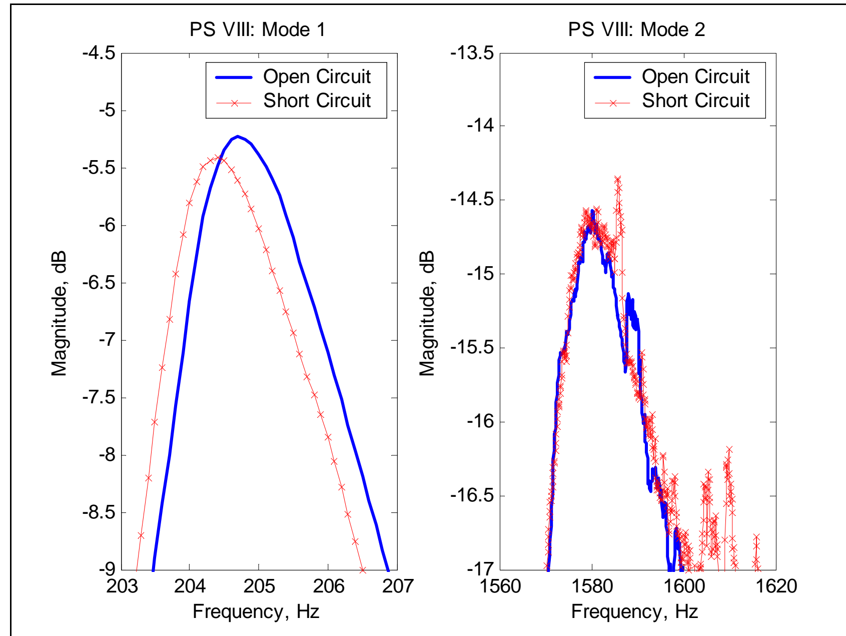

Figure 27. Changes in frequency near modes 1 and 2, PS VIII

Figure 28 shows the mode 3 frequency response and Figure 29 shows the mode 4 and 5 responses for resonator PS VIII. As in the mode 2 data, the data for modes 3 to 5 shows minimal shift in frequency or a short circuit frequency that is higher than the open circuit value.

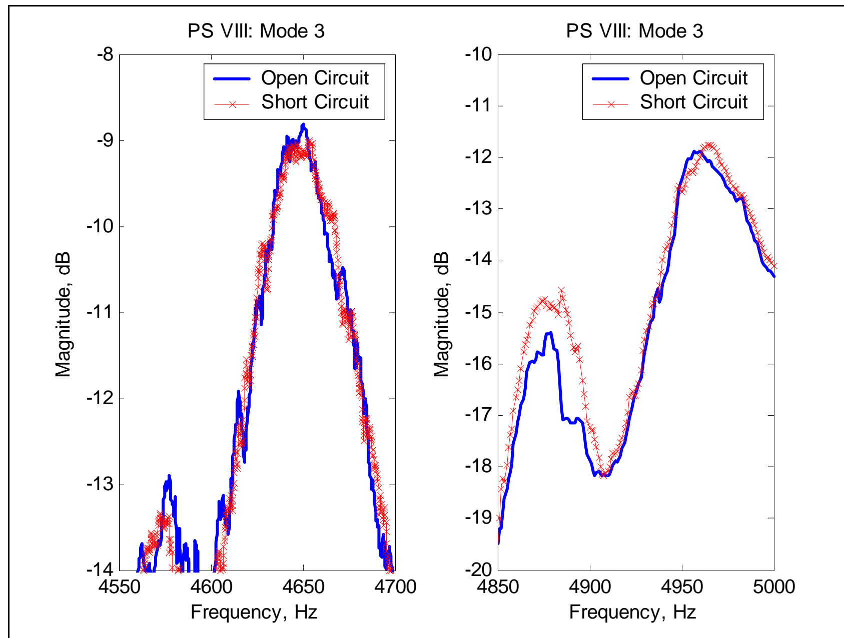

Figure 28. Changes in frequency near mode 3, PS VIII

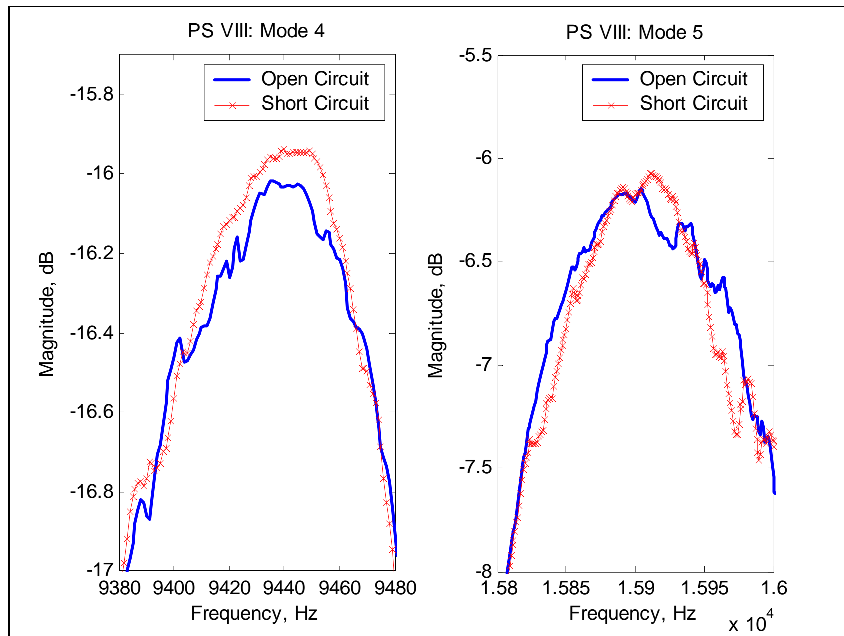

Figure 29. Changes in frequency near modes 4 and 5, PS VIII

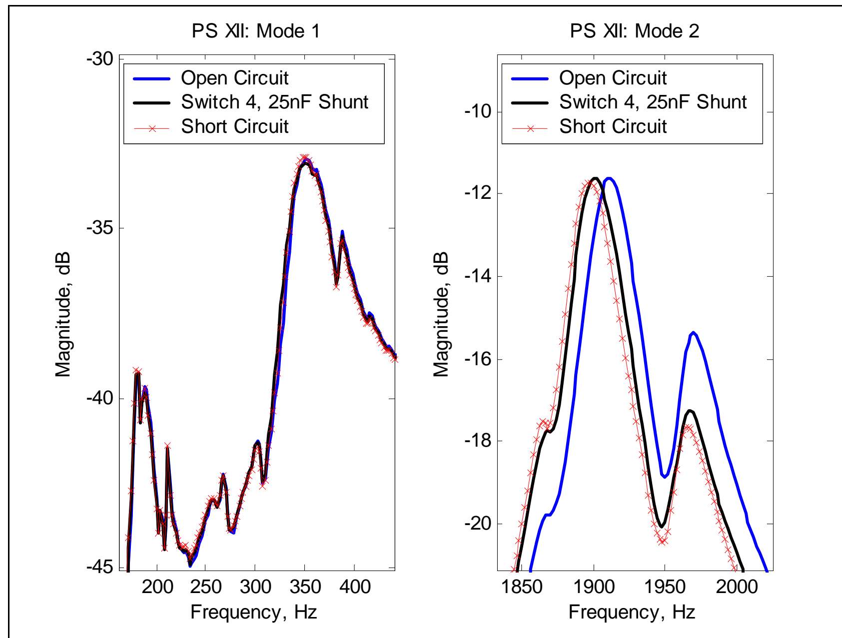

Figure 30. Changes in frequency near modes 1 and 2, PS XII

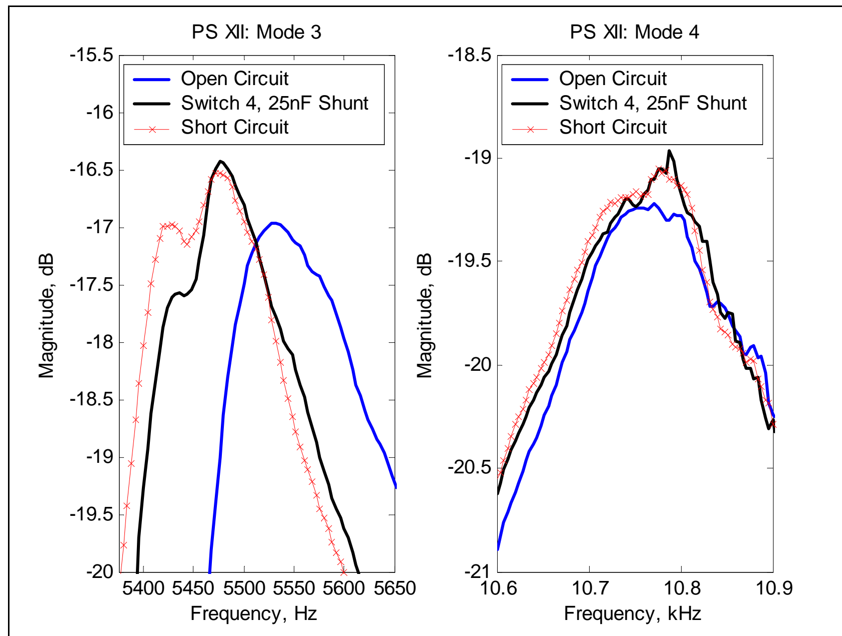

Figure 31. Changes in frequency near modes 3 and 4, PS XII

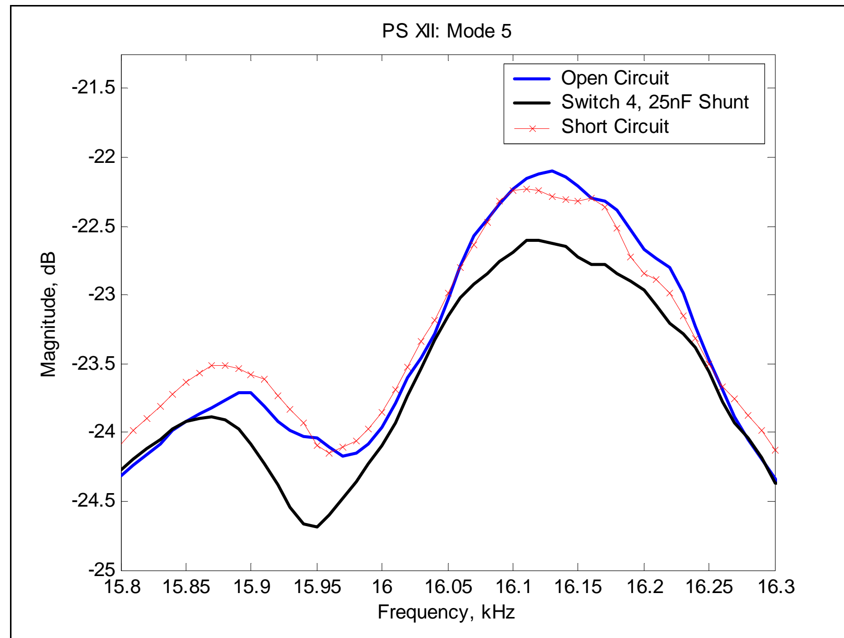

Figure 32. Changes in frequency near mode 5, PS XII

Figure 30 shows the mode 1 and mode 2 frequency responses for resonator PS XII. The change in frequency in mode 1 is approximately 2 Hz for both possible mode 1 responses at 185Hz and 352Hz. The change in frequency of the peak response of mode 2 is approximately 13Hz and can be clearly seen in the figure. The 55Hz frequency change in mode 3 peak response is shown in Figure 31. There is no apparent change in the frequency of vibration of mode 4 as seen in the frequency response plot. Mode 5 tuning, as seen in Figure 32, is approximately 20Hz.

Resonator PS XIII mode 1 data, Figure 33, shows differences in magnitude of response away from the resonance peak but no difference in the resonance peak frequency. However, the Mode 2 data shows that there is a frequency shift of 10Hz as a result of switching between the open and short circuit condition on the passive layer. Modes 3, 4 and 5 in resonator PS XIII (Figure 34 and Figure 35) are also equally well behaved showing frequency tuning of 50Hz, 90Hz and 130Hz respectively. In Figure 34 it can be seen that the peak in the frequency

response with the intermediate capacitive shunt is on occasion lower in frequency than the short circuit peak response frequency.

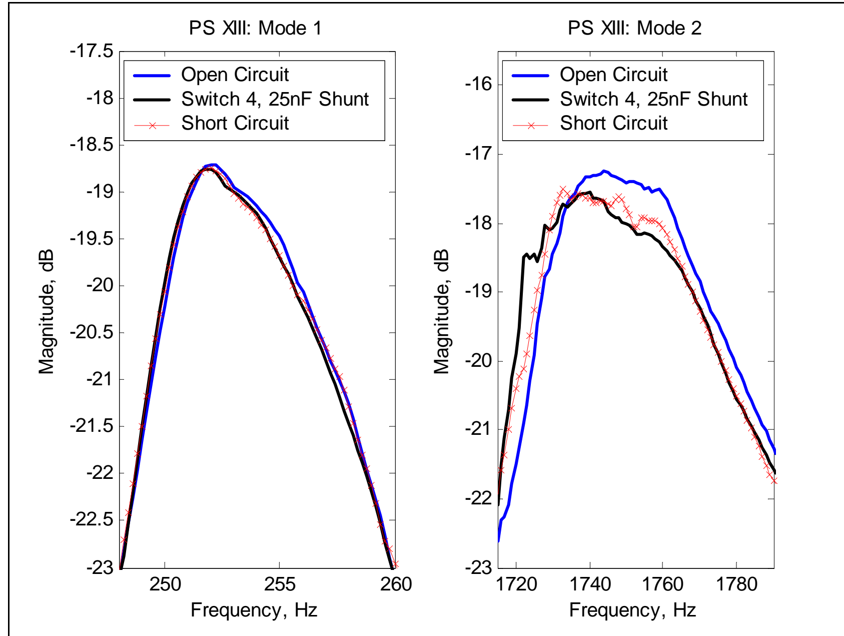

Figure 33. Changes in frequency near modes 1 and 2, PS XIII

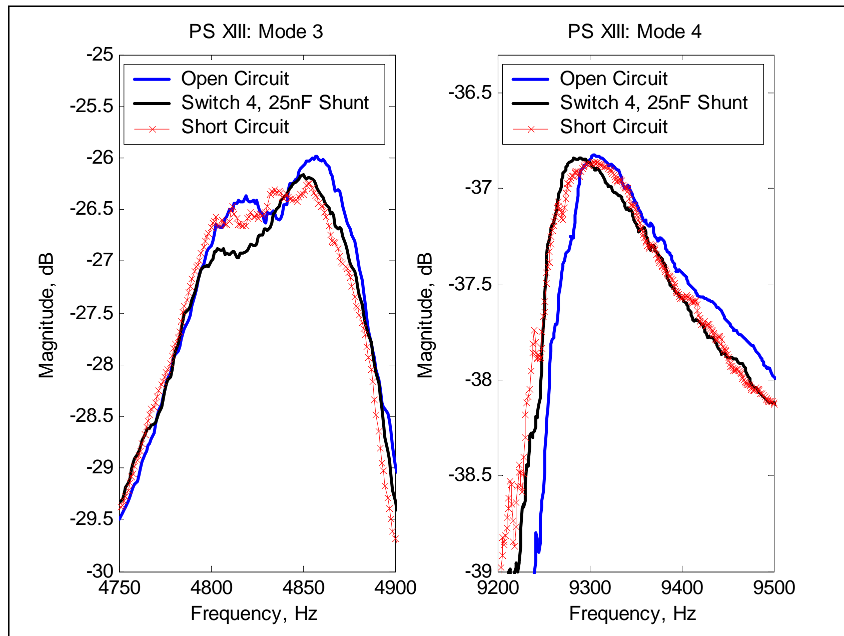

Figure 34. Changes in frequency near modes 3 and 4, PS XIII

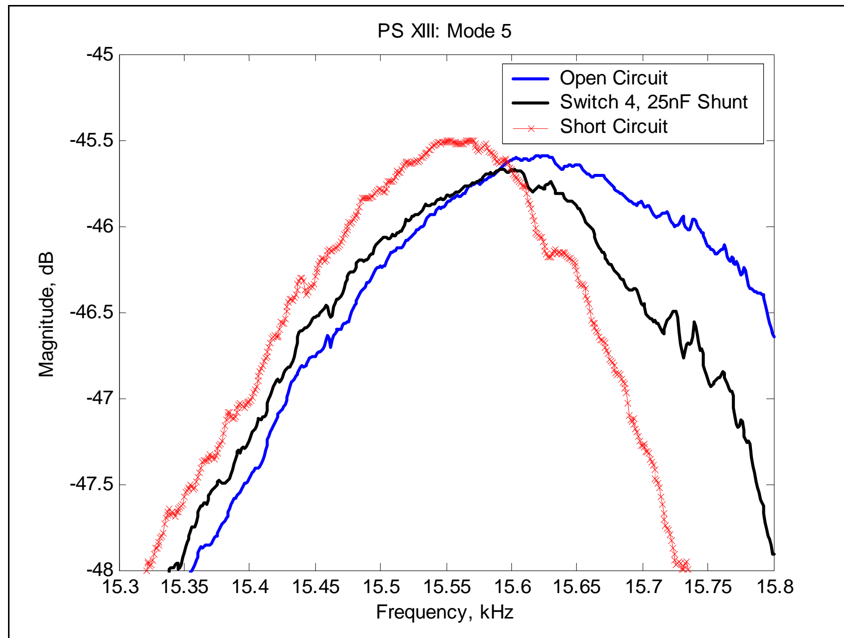

Figure 35. Changes in frequency near mode 5, PS XIII

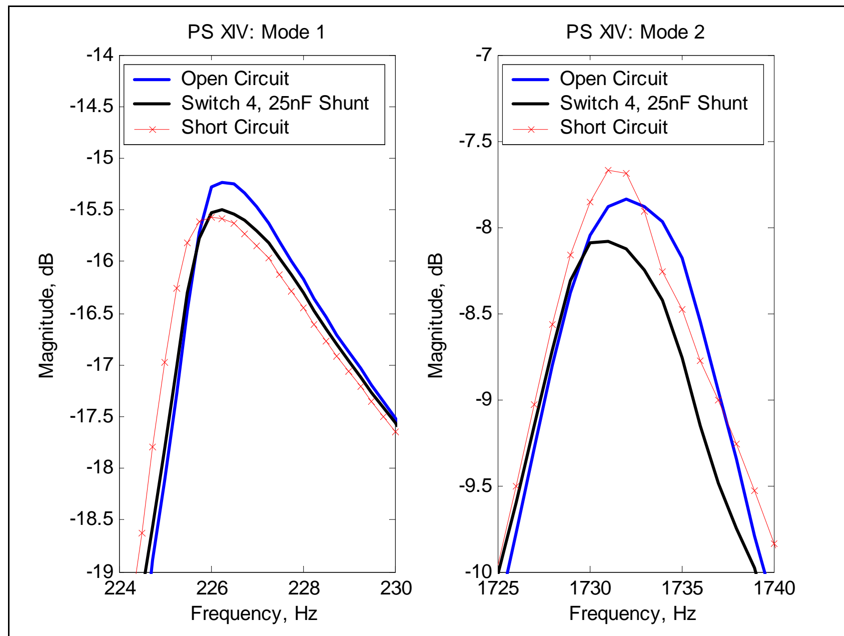

Figure 36. Changes in frequency near modes 1 and 2, PS XIV

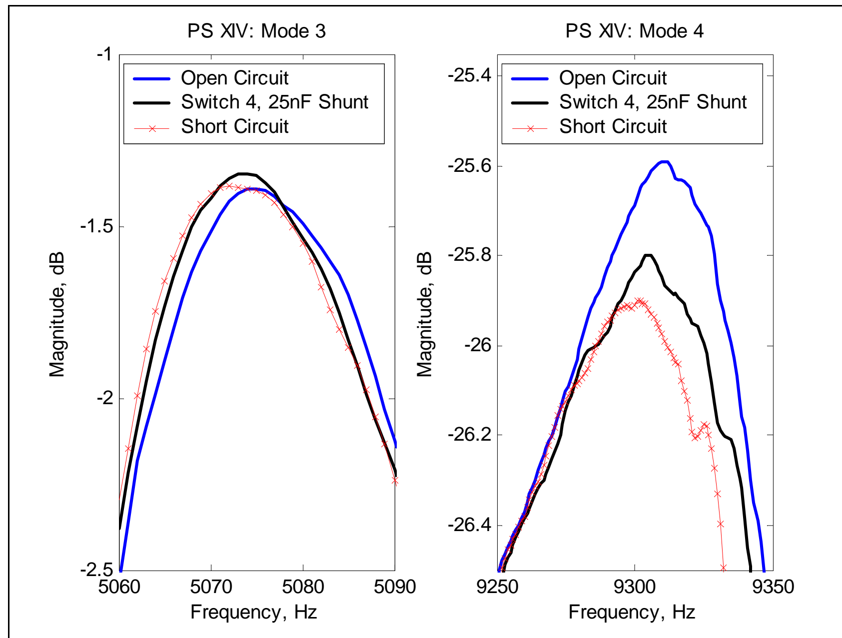

Figure 37. Changes in frequency near modes 3 and 4, PS XIV

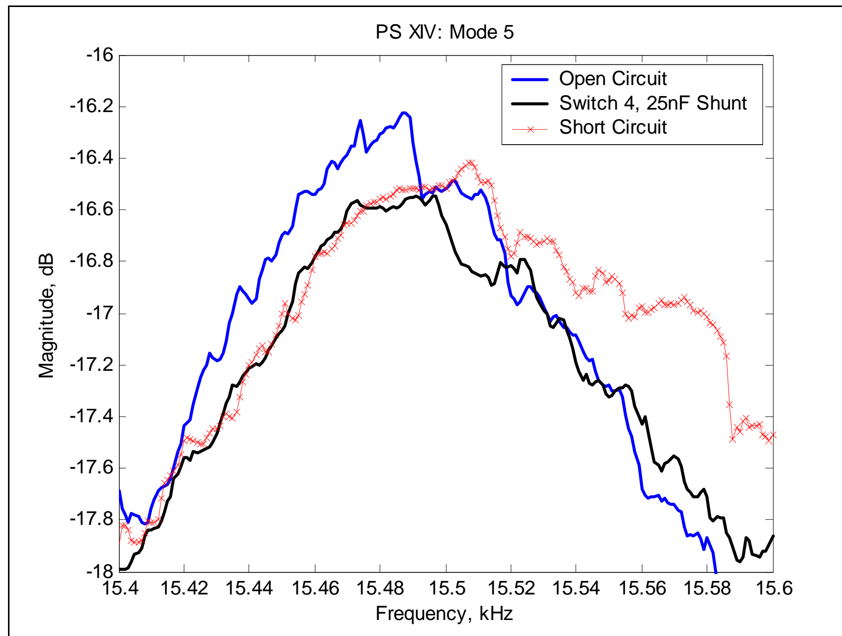

Figure 38. Changes in frequency near mode 5, PS XIV

Resonator PS XIV frequency response and tuning data can be seen in Figure 36 to Figure 38. In Figure 36, the frequency response curves are smooth and the curves clearly shift to the left (and lower in frequency) as we move from the open circuit condition, to the capacitive shunt and to

short circuit. The tuning range for resonator PS XIV modes 1 and 2 is 0.25Hz and 1 Hz respectively. The mode 3 and mode 4 frequency response, Figure 37, is also quite smooth (for example in contrast with mode 2 response for resonator PS XV in Figure 39), and the tuning effect of switching can be seen. The tuning range is not as high as was observed in PS XIII, 2Hz and 9Hz for modes 3 and 4 respectively versus 50Hz and 90Hz for PS XIII. Figure 38 is the frequency response of resonator PS XIV for the three switch conditions; open circuit, short circuit and shunt with a 25nF capacitor. The data shows that the peak in the frequency response is at a higher frequency when the resonator passive layer is short circuited than when the layer is held in the open circuit condition.

The tuning data for resonator PS XV is shown in Figure 39 to Figure 41. Figure 39 shows the mode 1 and mode 2 data. The mode 1 open circuit resonance peak was chosen to be at 164.5Hz. Switching from open circuit to the capacitive shunt causes a reduction in magnitude of the response below the resonance peak. This collapse is amplified when we short circuit the passive layer. Consequently, the short circuit peak frequency is higher than the open circuit frequency. Mode 2 data is quite noisy near resonance resulting in a higher short circuit than open circuit frequency. The noisy nature of the data is also apparent in mode 3 and 4 data in Figure 40. However, the tuning range for modes 3 and 4 are 3.5Hz and 5Hz with a short circuit frequency below the open circuit value. The frequency response of mode 5 of resonator PS XV can be seen in Figure 41. The tuning range for this mode is 20Hz. As with the other modes, the resonance curves are not smooth.

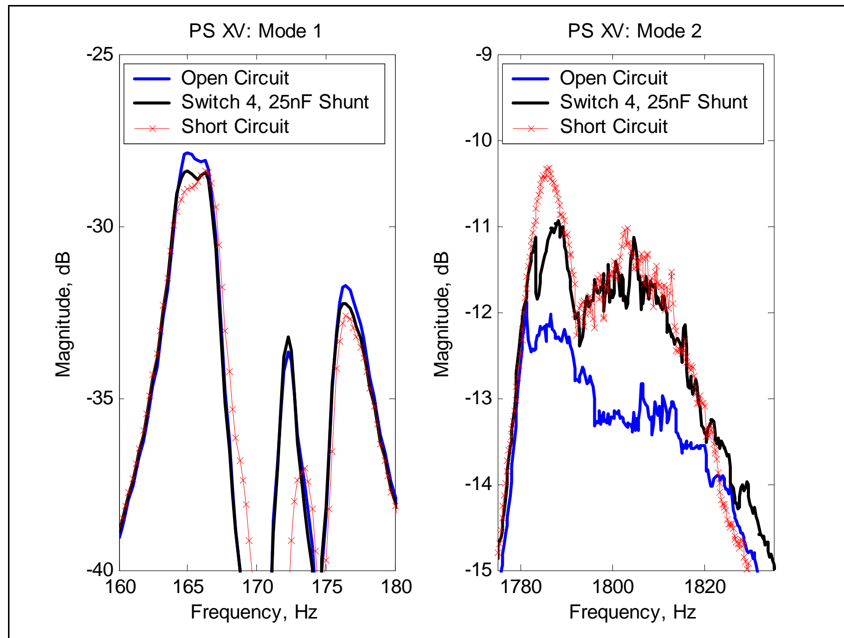

Figure 39. Changes in frequency near modes 1 and 2, PS XV

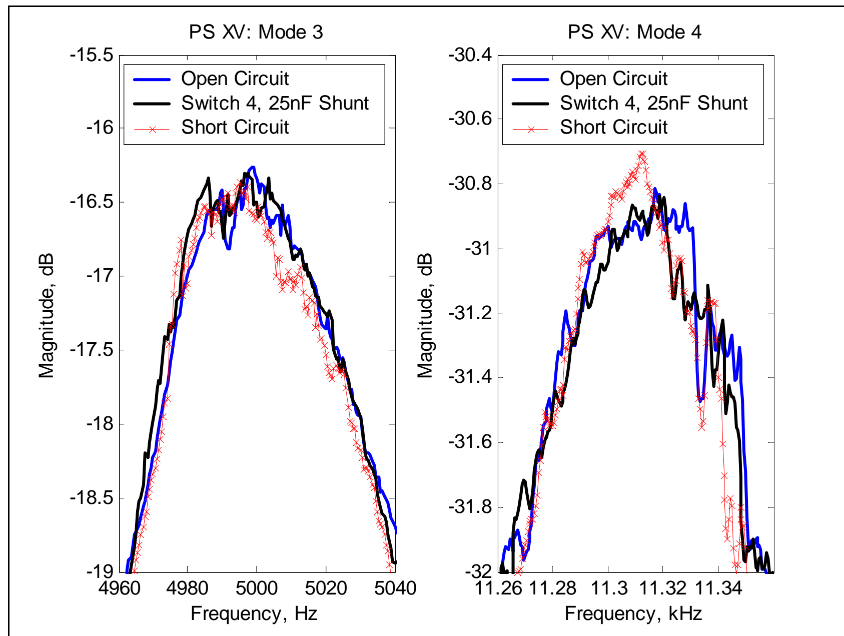

Figure 40. Changes in frequency near modes 3 and 4, PS XV

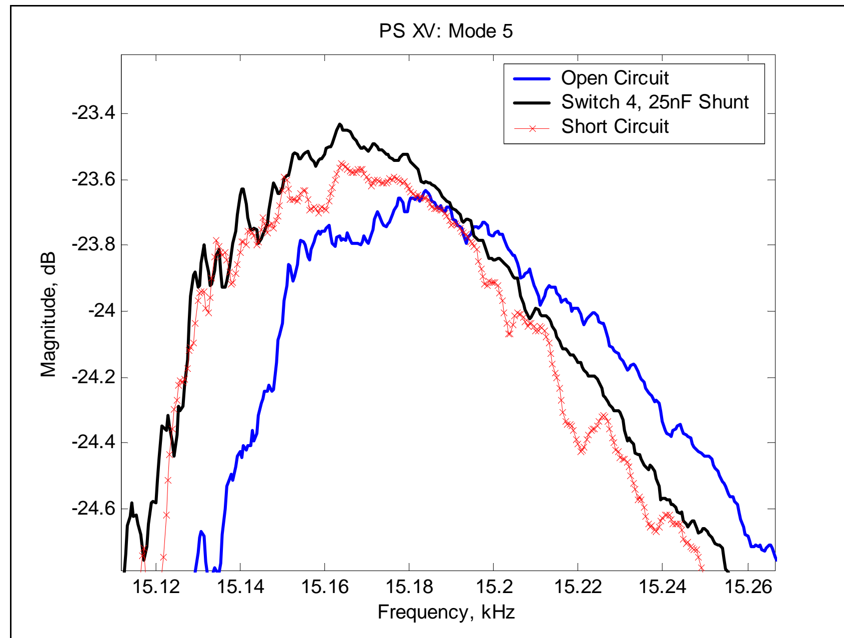

Figure 41. Changes in frequency near mode 5, PS XV

6.4 SUMMARY

The analytical model predicts that the passive portion of our resonators couples differently to the various bending modes. This differential coupling is borne out in terms of differences in the tuning range as a percentage of the open circuit frequency of vibration. The magnitude of the tuning ranges observed in experiment match the predicted values to within an order of magnitude with the observed value sometimes surpassing prediction and vice versa. As was seen in Table 7, the experimental tuning range obtained from SigLab is negative for three of the resonators. The open and short circuit frequencies of vibration are chosen to be the peak value in the frequency response near the analytically calculate bending mode frequency. On occasion, due to the noisy nature of some of the frequency response data, using the peak value in the frequency response causes the short circuit frequency to be recorded as higher than the open circuit frequency.

An example of this result is shown in Figure 42 which shows the frequency response of resonator PS VIII at frequencies close to the analytically calculated frequency of vibration for bending mode two. The bending mode two open circuit frequency of vibration is chosen, as indicated by arrow, to be at approximately 1580Hz. Using the same technique - maximum response indicates the bending mode of vibration - the short circuit frequency is chosen to be at approximately 1586Hz. Consequently, the tuning range is indicated as being –6Hz, a result contrary to expectation.

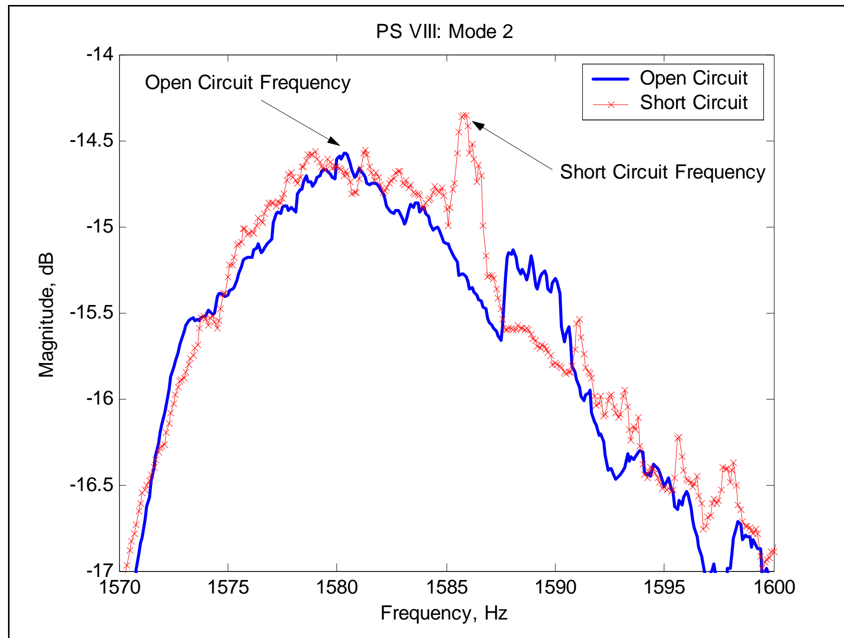

Figure 42. Changes in frequency near mode 2, PS VIII

Another source of variability in the experimental tuning data shown in Table 7 are the difficulties encountered in the manufacturing process. Differences in the size; and therefore the frequency of operation and tuning range, of the PZT layers was inevitable since the PZT was cut by hand. In addition, the substrate and PZT layers were joined in a clamping mechanism that on occasion allowed misalignment of the two layers.

7.0 FEEDBACK GAIN

7.1 ANALYTICAL MODEL

It is intended that the amplified sensor signal be fed back to the actuator to drive self-oscillation of the resonator. For a resonator to operate at a particular vibration mode there are gain and phase requirements for the loop transfer function at the frequency of vibration. The resonator will only operate at a frequency of vibration for which the magnitude of the loop transfer function is one and the phase an integer multiple of 360° (Gerber, 1985). This holds true for all the different feedback schemes that may be utilized. The equations developed in this section are concerned only with gain and ignore the phase relationship.

An evaluation of the amplification gain required could help give an indication of the feasibility of the designs and feedback techniques. For a particular available gain, it may even be possible to predict the mode and frequency of vibration at which the system would operate.

If the sensor voltage is used as the input to a feedback loop whose gain is G the voltage at the output (the actuator) is,

$$v_A = G v_S \tag{7.1-1}$$

Then equation 5.1-4, reproduced below,

$$(M_S + M_P)\ddot{r} + (K_S + K_P + \theta^{P^T} C^{p^{-1}} \theta^P) r = B_f f + \begin{bmatrix} \theta^A & \theta^S \end{bmatrix} \begin{Bmatrix} v^A \\ v^S \end{Bmatrix} \quad (7.1\text{-}2)$$

can be written as,

$$\begin{gathered} (M_S + M_P)\ddot{r} + (K_S + K_P + \theta^{P^T} C^{p^{-1}} \theta^P) r = B_f f + (\theta^A G + \theta^S) v^S \\ v^S = C^{S^{-1}} [q^S - \theta^S r] \end{gathered} \quad (7.1\text{-}3)$$

If there are no external forces applied to the beam then f is zero. Making the substitution for the voltage on the sensor for the case where f is zero,

$$(M_S + M_P)\ddot{r} + (K_S + K_P + \theta^{P^T} C^{p^{-1}} \theta^P) r = (\theta^A G + \theta^S) C^{S^{-1}} q^S - (\theta^A G + \theta^S) C^{S^{-1}} \theta^S r \quad (7.1\text{-}4)$$

which upon simplification is as below.

$$(M_S + M_P)\ddot{r} + (K_S + K_P + \theta^{P^T} C^{p^{-1}} \theta^P + \theta^A G C^{S^{-1}} \theta^S + C^{S^{-1}} \theta^{S^2}) r = (\theta^A G + \theta^S) C^{S^{-1}} q^S \quad (7.1\text{-}5)$$

With the following product,

$$v^{S'} = C^{S^{-1}} q^S \quad (7.1\text{-}6)$$

a transfer function from the voltage, $v^{S'}$, to tip displacement can be developed for the system,

$$\frac{R(s)}{v^{S'}(s)} = \frac{\theta^A G + \theta^S}{s^2 (M_S + M_P) + K_S + K_P + \theta^{P^T} C^{P^{-1}} \theta^P + \theta^A G C^{S^{-1}} \theta^S + C^{S^{-1}} \theta^{S^2}} \quad (7.1\text{-}7)$$

Equation 7.1-6 gives the system transfer function from the voltage on the sensor to the displacement variable, *R(s),* when there is a feedback gain *G.*

Using Equation 5.1-1, reproduced below,

$$\begin{bmatrix}\theta^A \\ \theta^S \\ \theta^P\end{bmatrix} r + \begin{bmatrix} C^A & 0 & 0 \\ 0 & C^S & 0 \\ 0 & 0 & C^P \end{bmatrix} \begin{Bmatrix} v^A \\ v^S \\ v^P \end{Bmatrix} = B_q \begin{bmatrix} q^A \\ q^S \\ q^P \end{bmatrix} \tag{7.1-8}$$

an equation for the actuator voltage of the system as a function of displacement can be written for the case where there is no charge accumulation ($q^A = 0$). This gives the transfer function from displacement to actuator voltage as below,

$$\frac{v^A(s)}{R(s)} = (C^A)^{-1}\theta^A \tag{7.1-9}$$

Concatenating the systems defined by equations 7.1-7 and 7.1-9,

$$\begin{gathered} \frac{v^A(s)}{R(s)} \frac{R(s)}{v^{S'}(s)} = \frac{v^A(s)}{v^{S'}(s)} \\ \frac{v^A(s)}{v^{S'}(s)} = \frac{(C^A)^{-1}\theta^A(\theta^A G + \theta^S)}{s^2(M_S + M_P) + K_S + K_P + \theta^{P^T} C^{P^{-1}} \theta^P + \theta^A G C^{S^{-1}} \theta^S + C^{S^{-1}} \theta^{S^2}} \end{gathered} \tag{7.1-10}$$

Equation 7.1-10 is the system transfer function from the voltage on the sensor to the actuator voltage. In a resonator, whose characteristics are described by the system transfer function, the transfer function is required to have at least a value of unity at the frequency of resonator operation. A feedback gain, *G*, can be found that would ensure that the transfer function has unit value at a particular resonant frequency. This then would be the minimum feedback gain required for the resonator to operate at that particular frequency. Varying the physical dimensions of the sensor and actuator would cause changes in the couplings and capacitances of the sensor and actuator portions. Consequently, the effect of these changes on the gain can be determined.

7.2 RESULTS

The cantilever beam resonator actuator is to be driven by the amplified voltage signal from the sensor. For resonance to occur the amplifier gain must be sufficient to drive the resonator from the sensor signal. This means that the gain must be high enough to overcome any losses in the electrical and mechanical parts of the resonator. In addition, the loop phase has to be 360° or some integer multiple of 360°.

Using Matlab® the feedback gain required to achieve this has been found. Any design changes made to the sensor and actuator dimensions change four of the elements in the transfer function given for the resonator (equation 7.1-10). These four elements are the electromechanical couplings of the sensor and actuator, θ^S and θ^A, and the capacitances, C^S and C^A.

Figure 43 shows the gain results obtained from the Matlab model. The gain, *G*, required to make the magnitude of the loop transfer function equal to one is shown as a function of the normalized sensor and actuator lengths. The actuator, in this plot and subsequent plots of the gain and actuator coupling, is located adjacent to the root of the beam. The actuator length is varied from zero to the full beam length. The sensor is located adjacent to the actuator and its length varies from the edge of the actuator to the full beam length. This sensor and actuator placement corresponds to the layout in Figure 9. The section of the plots where the normalized sensor and actuator lengths approach one is the region where no solution can be calculated from the model since the normalized sensor and actuator lengths must, at most, add up to the normalized beam length, one.

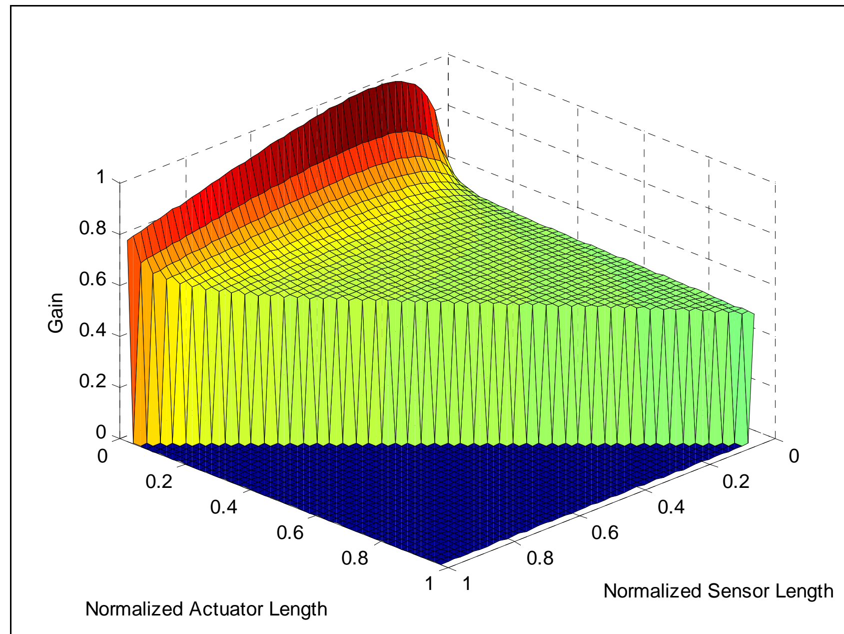

Figure 43. Gain for bending mode 1 versus sensor and actuator dimensions

From Figure 43 it can be seen that the lowest calculated gain is found when the actuator length is at least approximately half the beam length. At the same time it is apparent that in this region, changes in sensor length do not seem to affect the magnitude as much as changes in actuator length do.

The gain required for operation of the resonator is determined, in part, by the actuator authority and the magnitude of the voltage developed on the sensor portion of the PZT layer of the beam. Greater actuator authority means a lower voltage for a particular displacement of the beam. It has already been shown that the actuator electromechanical coupling (with no force input), is proportional to the displacement of the beam, and thus, proportional to the actuator authority. Figure 44 shows how the magnitude of the electromechanical coupling changes as the actuator length is increased from a minimal value to the full length of the beam. Also plotted in the figure is the displacement shape function.

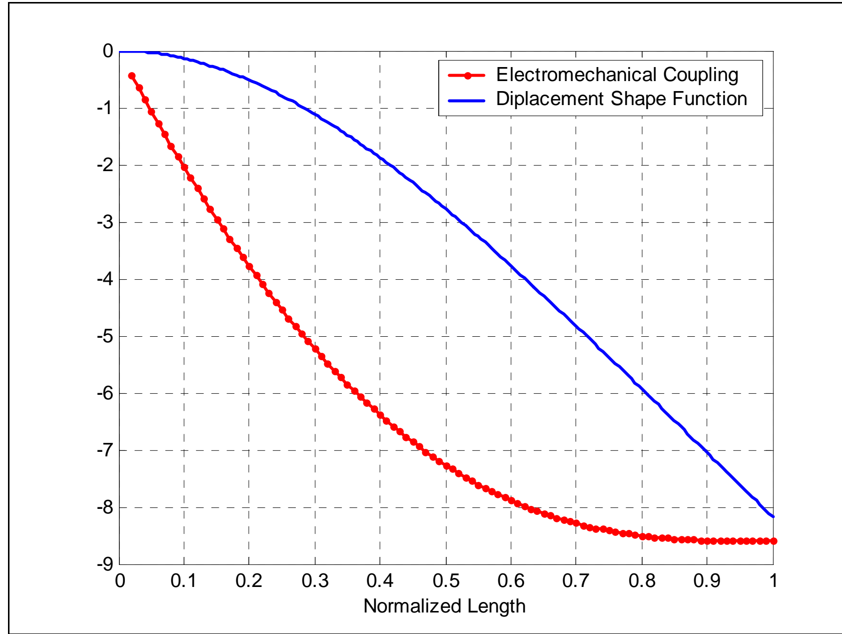

Figure 44. θ^A as a function of actuator length for bending mode 1

From Figure 44, it is apparent that as actuator length grows from zero, there is a rapid increase in the magnitude of the authority the actuator has over bending mode one. This increase is seen to diminish as the actuator length approaches full coverage of the beam. Figure 43 shows that this rapid increase in authority occurs in tandem with the decrease in gain. The diminishing increase in authority is exhibited in Figure 43 by the flattening of the gain curve. Further increases in actuator authority beyond about one half beam coverage are offset by decreases in sensor output as the sensor shrinks. Therefore, the optimum design point for minimum gain for bending mode one is an actuator that covers about half the beam.

Figure 45 to Figure 52 show the corresponding results (as in Figure 43 and Figure 44) for modes two through five. The first plot for each mode shows the required gain for resonance as sensor and actuator lengths are varied. Each plot shows variations in gain as the actuator length changes from zero to the beam length. It is interesting that for each mode there are bands of

high and low gain. As the mode number increases there are more bands. This pattern is not coincidental but depends strongly on the actuator coupling to any given mode.

The second plot for each mode (following the gain plot) shows the actuator coupling value plotted as a function of actuator length normalized to the beam length. This value is seen to vary. Also shown in each plot is the mode shape itself (The actuator coupling is proportional to the second partial derivative of the displacement function with respective to the coordinate x, the axis along which the beam length is measured).

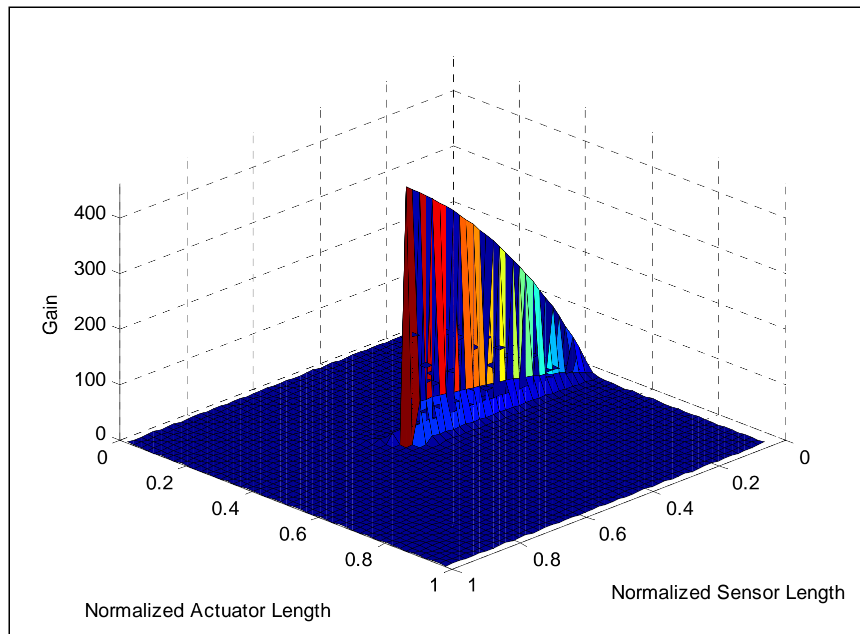

Figure 45. Gain for bending mode 2 versus sensor and actuator dimensions

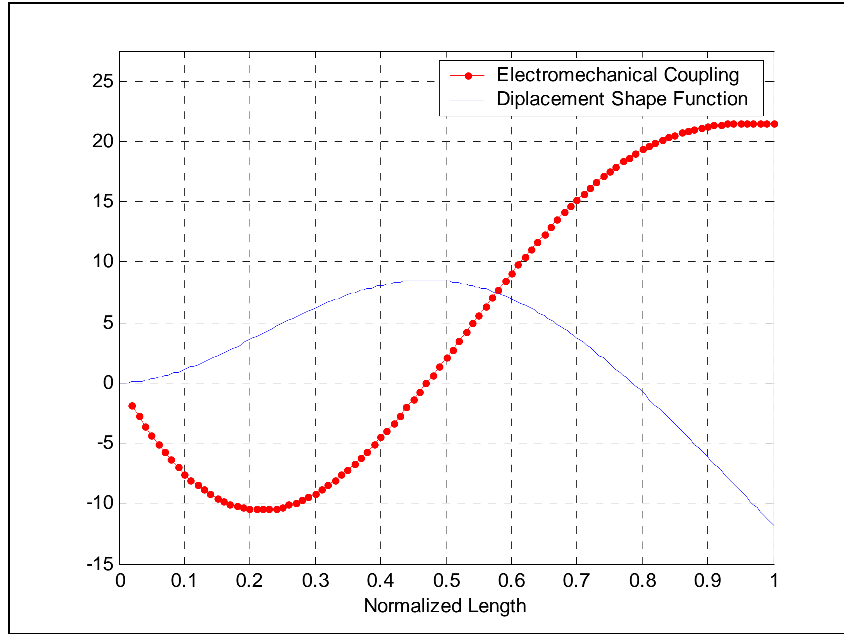

Figure 46. θ^A as a function of actuator length for bending mode 2

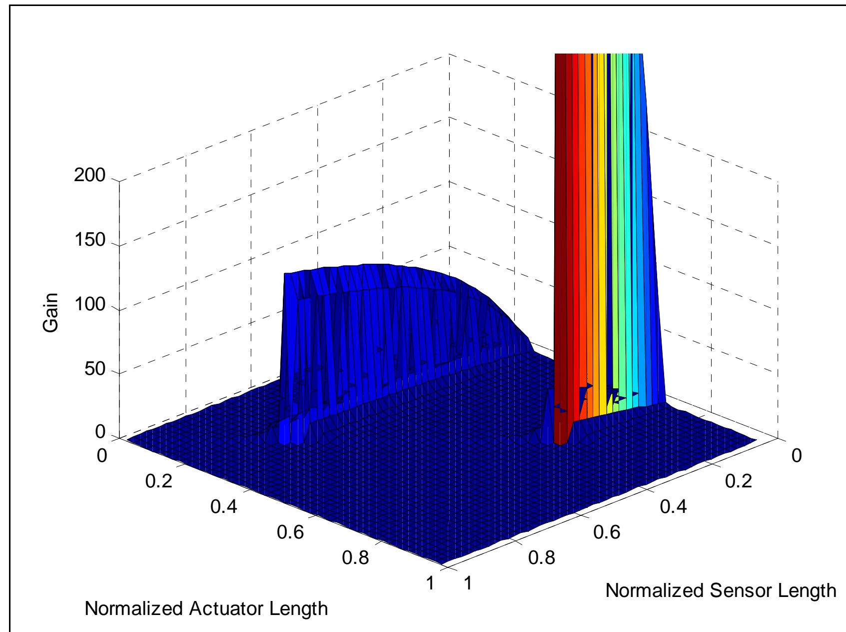

Figure 47. Gain for bending mode 3 versus sensor and actuator dimensions

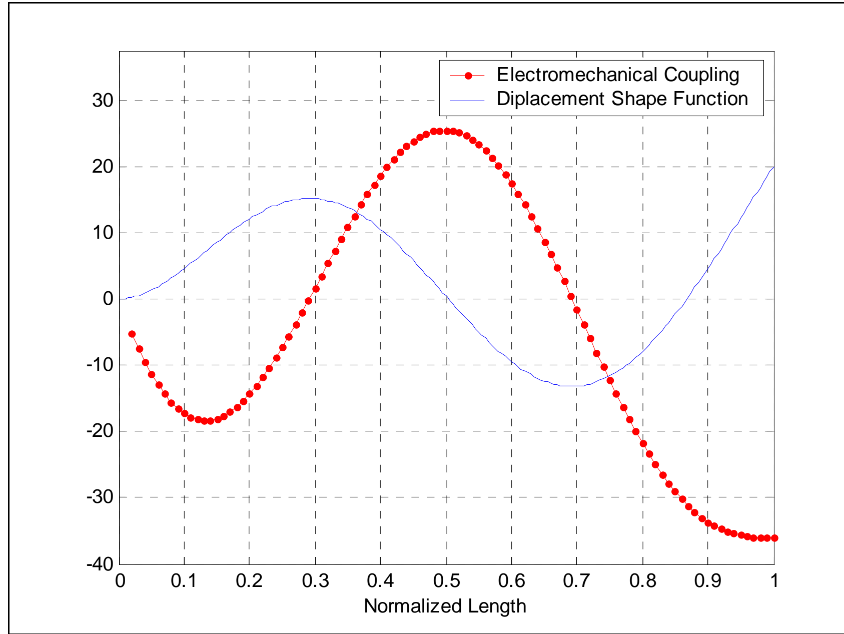

Figure 48. θ^A as a function of actuator length for bending mode 3

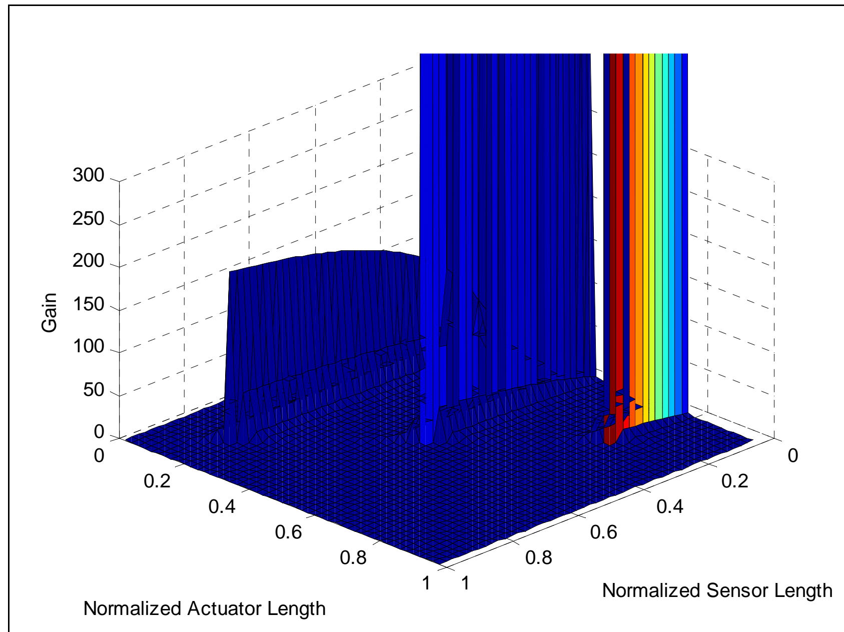

Figure 49. Gain for bending mode 4 versus sensor and actuator dimensions

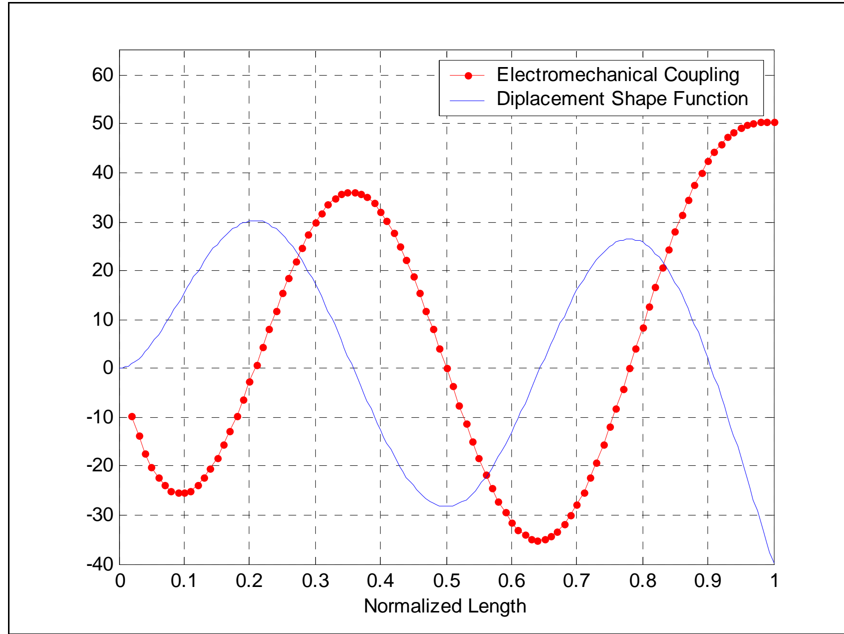

Figure 50. θ^A as a function of actuator length for bending mode 4

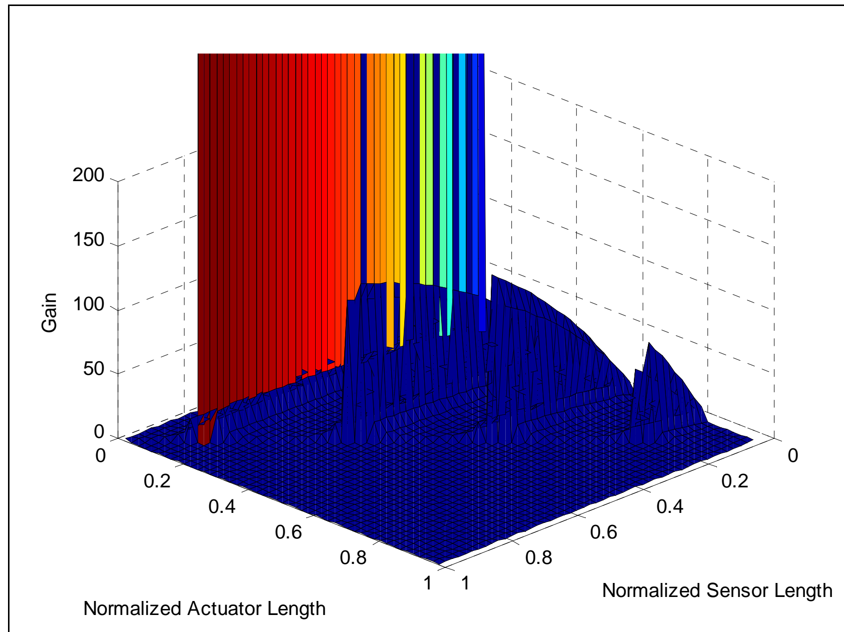

Figure 51. Gain for bending mode 5 versus sensor and actuator dimensions

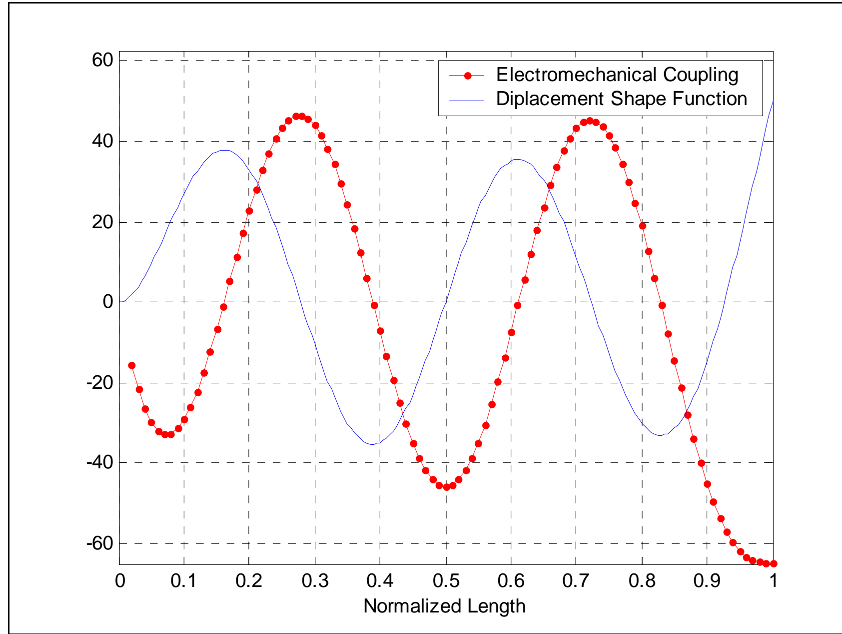

Figure 52. θ^A as a function of actuator length for bending mode 5

Note that the regions in each gain plot that show the highest required gain correspond to the actuator lengths that have coupling factors of zero. For example, Figure 51 shows that the gain required for resonance is largest at approximately 0.15, 0.4, 0.6 and 0.83 of the normalized length of the beam. As can be seen in Figure 52, these correspond to points for which the electromechanical coupling, θ^A, is zero. It can also be seen that these points are where the displacement shape functions have a gradient of zero. The same characteristics can be observed for each set of figures, with high gain areas occurring when the electromechanical coupling of the actuator is low for each mode. In the high gain bands, with the exception of the first mode, it is interesting to note that increasing the sensor length has a deleterious effect vis-à-vis minimizing gain. This result is counterintuitive to expectations; it seems logical that a greater sensor area would produce a larger signal voltage and hence cause a lower gain requirement.

7.3 SUMMARY

The minimum feedback gain that ensures that the sensor to actuator voltage transfer function has at least unit magnitude is seen to depend mainly on the second partial derivative of the displacement function or mode shape. Where the second derivative of the mode shape approaches zero the gain approaches maximal value. This zero in the second derivative of the mode shape function corresponds to both the zero in the electromechanical coupling and a gradient of zero in the shape function. Low feedback gain occurs as a consequence of having high coupling to the particular mode in question. This combination of low feedback gain and high coupling makes a resonator more efficient at operating at a particular mode.

This result was used in the design of our resonators. The actuator length was set at approximately a quarter of the total beam length. The electromechanical coupling, which is large when the mode shape is far from the high gain (low gradient) region of the displacement shape function, is highest for mode six at this length. In descending order, the magnitude of the electromechanical coupling to other modes is mode eight, mode five, mode three, mode seven, mode two, mode four and, lastly, mode one.

8.0 REACTANCE AND RESONATOR OPERATING FREQUENCIES

Impedance, resistance and capacitance of an electrical circuit determine the behavior of the circuit. If the impedance, resistance and capacitance are known circuit properties, the behavior of the circuit at various frequencies can be determined by transforming the circuit properties into their equivalent impedance terms. These impedance terms have real and imaginary parts. An electrical equivalent of the resonator characteristics (mass, stiffness, etc.) can be obtained and these terms transformed into impedance.

The imaginary part of impedance is known as reactance and is important in resonator design. On a reactance versus frequency plot each point where the reactance equals zero (when the impedance is purely real) corresponds to a vibration mode. When the resonator is placed in a driving circuit, such as the Pierce circuit configuration, the operational frequency of the resonator is close to the vibration mode frequency but in the positive reactance (or inductive) region. The frequency of vibration shifts into this region due to the reactance that is added to the total electrical system by the addition of the Pierce circuit (Parzen, 1983).

In this chapter we shall look at how the equations of motion developed for the resonator can be transformed into impedance terms. The particular resonance requirements for a Pierce circuit shall be given in terms of the impedance terms developed. The setups used to obtain the

reactance versus frequency behavior of the resonators and to operate the resonators shall then be shown. The experimental reactance data from the resonators used in this work shall then be presented and the reactance and resistance of the actual operational points of the resonator using various circuit configurations shall be noted. Lastly, a summary of the chapter is given.

8.1 ANALYTICAL MODEL

From the equations developed starting from equation 5.1-1 it can be seen that the product of electromechanical coupling and displacement is equivalent to charge in an electrical system. So an electrical equivalent of the mechanical system can be obtained by the transformation,

$$M\theta\ddot{r} + K\theta r = 0 \Leftrightarrow L\ddot{q} + \frac{1}{C}q = 0 \tag{8.1-1}$$

where L is the inductance and C the capacitance of the system. It has been assumed that the electromechanical coupling is not a function of time. Therefore, the dynamic behavior of the system in equations 8.1-1 is unaffected by multiplication by the constant electromechanical coupling since the natural frequency of the system does not change. From equation 8.1-1 above, an equation for the impedance of the system as a function of frequency can be written since the impedance of inductance, resistance and capacitance are respectively,

$$\begin{aligned} Z_L &= j\omega L \\ Z_C &= \frac{-j}{\omega C} \end{aligned} \tag{8.1-2}$$

where ω is the frequency variable. The impedance for each mode modeled is then,

$$Z_i = j\left\{\omega L_i - \frac{1}{\omega C_i}\right\} \tag{8.1-3}$$

where j is the imaginary number. The total impedance of the modeled modes of the system, Z_T, is then,

$$\frac{1}{Z_T} = \sum_i \frac{1}{Z_i} \tag{8.1-4}$$

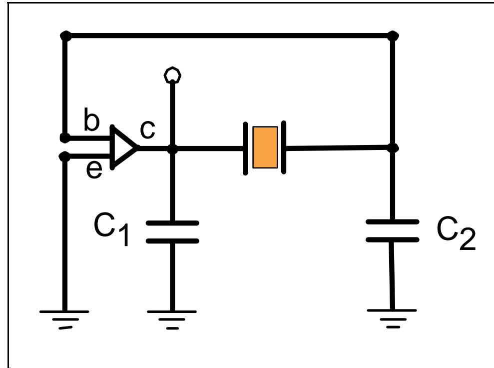

Figure 53. Pierce oscillator circuit configuration

A plot of the imaginary part of impedance (or reactance, X) can then give an indication of possible frequencies of vibration of the system since the requirements for oscillation for the Pierce oscillator configuration in Figure 53 are (Frerking, 1978; Parzen, 1983),

$$\begin{aligned} X_T &= X_1 + X_2 + X_r = 0 \\ g_m X_1 X_2 &\geq R_r \end{aligned} \tag{8.1-5}$$

where X_1 and X_2 are the reactances of the capacitors C_1 and C_2 in the circuit shown and R_r is the resistance of the resonator. g_m is the gain of the amplifier in the feedback loop. The subscripts r refer to the properties of the resonator. The first equation gives the phase requirements and the second gives the gain requirements for operation of the oscillator. The gain requirement is similar to that seen in the previous chapter.

Where the reactance and resistance of the resonator as a function of frequency are available the frequency of operation of the oscillator will be seen to be between the resonance and anti-resonance frequencies of the resonator (Figure 54) where the resistance is small enough to be overcome by the gain of the amplifier.

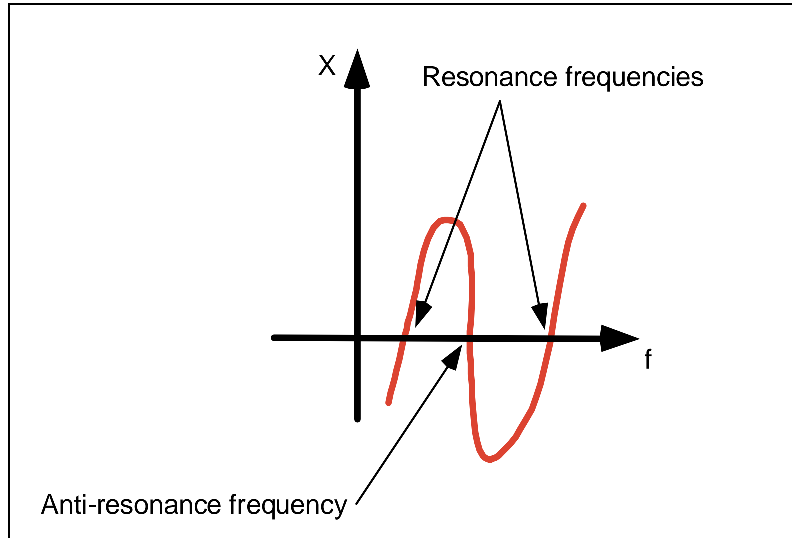

Figure 54. Resonance and anti-resonance frequency points

8.2 EXPERIMENTAL SETUP

Impedance data for the resonators was taken using an Agilent 4294A Precision Impedance Analyzer (see Figure 55). The resonators were in operational configuration with an inductor in line (or in series) with the sensor electrode. A series inductor was used so that impedance data obtained would match the setup in the experiments conducted using the modified Pierce circuit. Data obtained was for various series inductances and passive layer switch conditions.

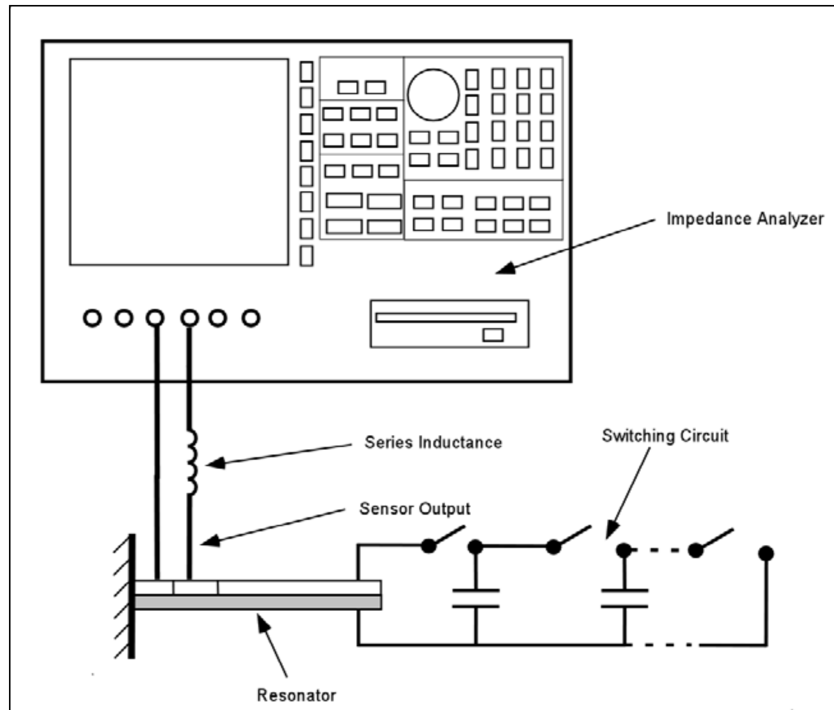

Figure 55. Impedance analysis experimental setup

To obtain the operational frequency data an amplifier was placed in a feedback loop between the sensor and actuator (see Figure 56). The output line of the amplifier was tied to both the actuator and a universal counter. The gate on the counter was set to 0.1 seconds and the frequency of operation of the resonator was read from the display. The amplifier input signal was obtained from the sensor electrode of the resonator. Both the sensor and actuator electrodes were also attached to the inputs of an HP54603B–60Mhz digital oscilloscope.

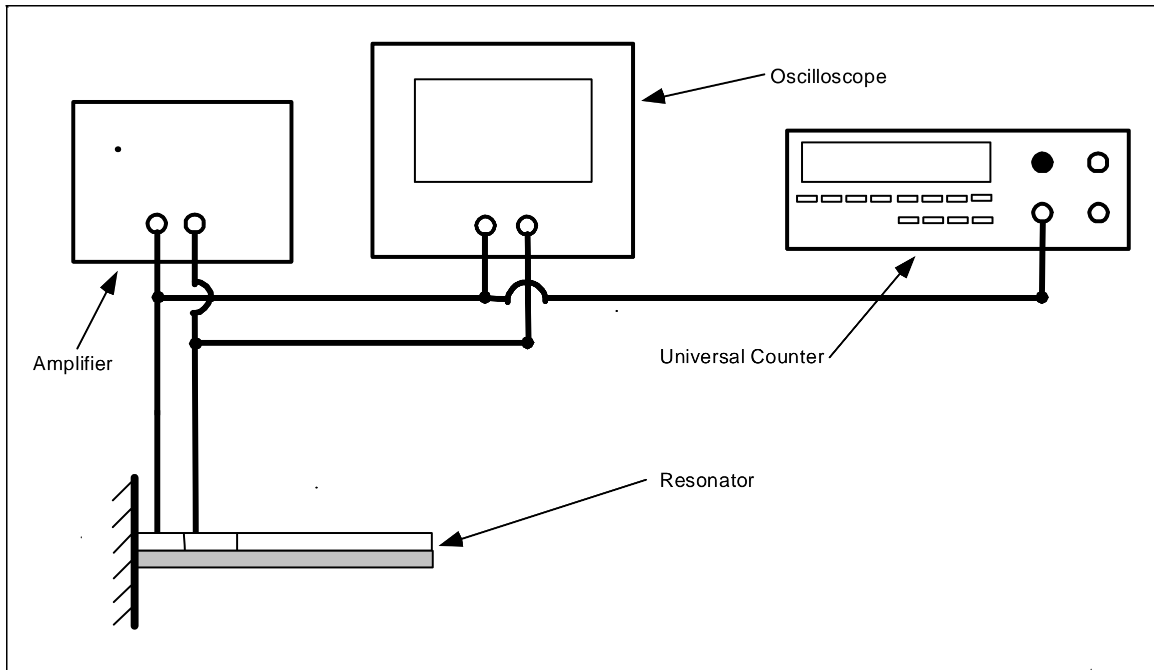

Figure 56. Operational frequency experimental setup

Two different schemes were implemented with varying success for amplification of the sensor signal. The first scheme was an amplifier with separate gain and phase adjustment (Figure 57 and Figure 58). The phase and gain adjustment is effected by potentiometers. The circuit is connected to positive and negative voltage as well as ground and has seventeen components. The second scheme used a variation of the Pierce configuration used in crystal resonators as shown in Figure 60 and Figure 59. The configuration used an inverter as an amplifier. The inverter is a Texas Instruments hex inverter model number SN54HCU04. C_1 and C_2 are 47pF capacitors and R is a 10kΩ biasing resistor. The modified Pierce circuit is the simpler to implement, having only four components and requiring only positive voltage and ground connections. Various inductors, L, were used in experiment. The inductances ranged from a low value of 1mH to a high of 82mH.

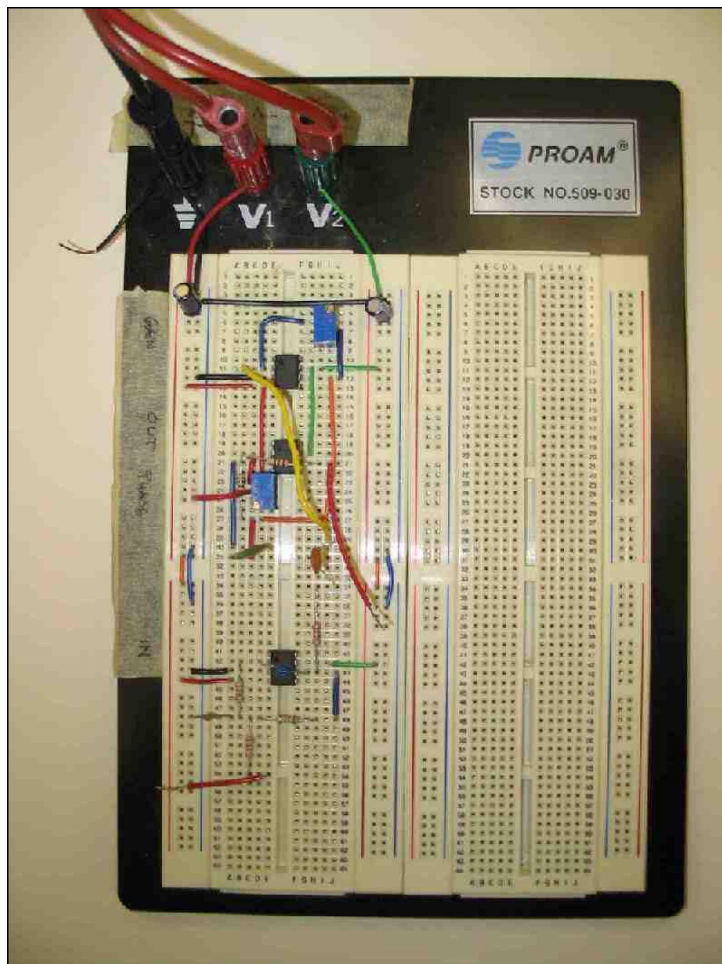

Figure 57. Electrical circuit with separate gain and phase adjustment

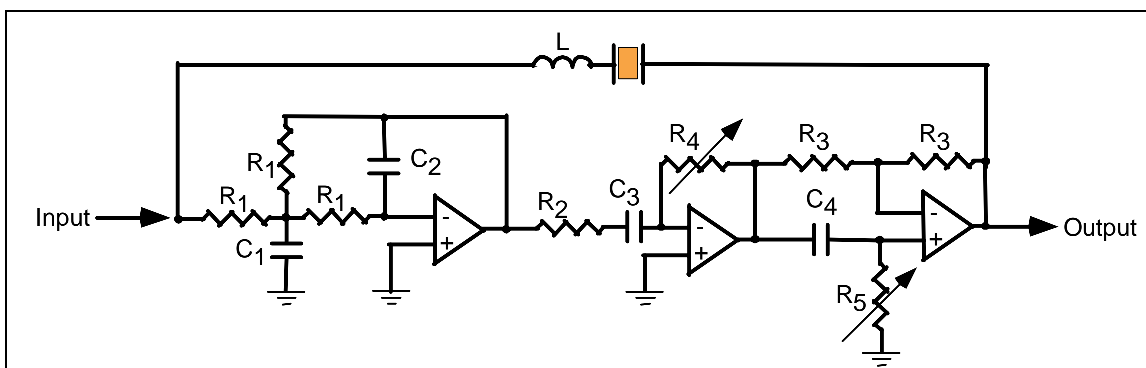

Figure 58. Circuit diagram of the gain and phase adjustable amplifier

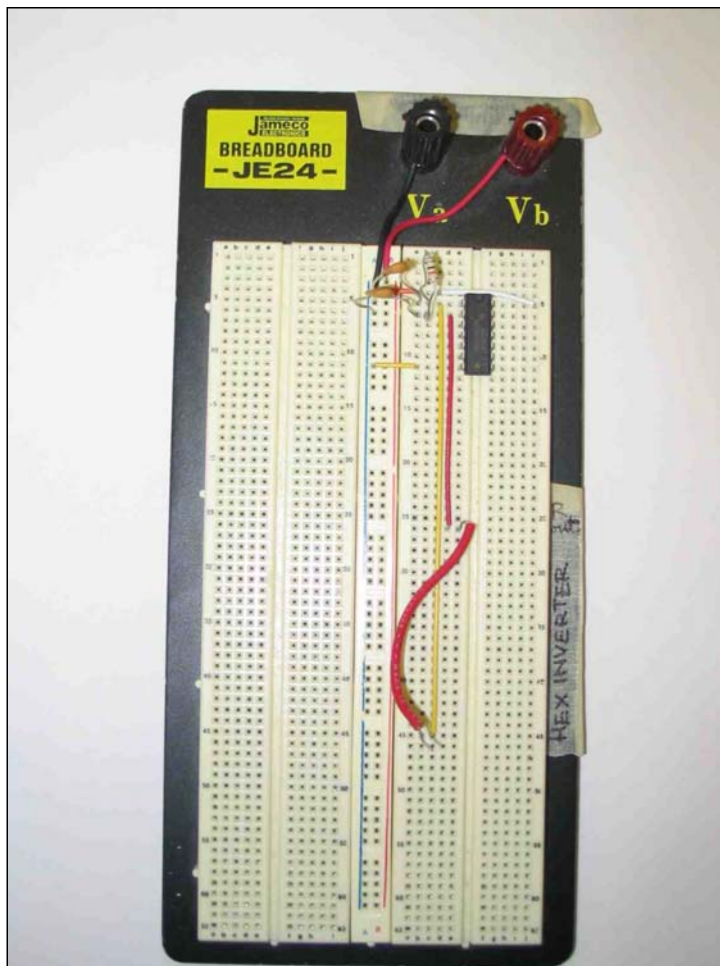

Figure 59. The modified Pierce circuit

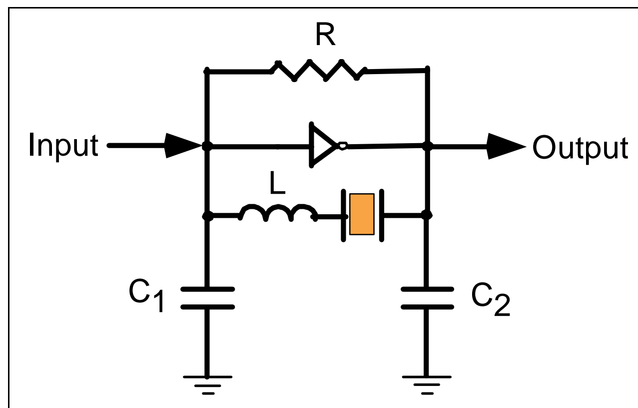

Figure 60. Circuit diagram of the variant of the Pierce circuit used in the experiments

The effect of switching on operational frequency was also observed. The operational frequency of the resonators was found to be above the bandwidth of SigLab. Consequently verification of the tuning range and position of the bending mode had to be obtained by alternate means.

Resonator frequency response data above the maximum frequency of the SigLab analyzer, i.e. 20kHz, was obtained using the output of a Stanford Research Systems DS345 30MHz Synthesized function generator to drive the actuator of the resonator. The sensor and actuator voltages were then measured using an HP54603B–60Mhz digital oscilloscope. Data for various switch conditions was taken and the peaks in the response of the resonators determined using Matlab.

8.3 COMPARISON OF ANALYTICAL AND EXPERIMENTAL RESULTS

8.3.1 Resonator PS VIII

Using the amplifier with separate phase and gain adjustment circuits, the open circuit frequency was 37.693kHz and short circuit frequency varied between 37.684kHz and 37.686kHz. This gives a tuning range between 6Hz and 9Hz. The operating frequency observed when the resonator was driven in the modified Pierce circuit configuration by the inverter is shown in Table 8. The operational frequency indicates that the resonator is operating near bending mode 8.

Table 8. Resonator PS VIII inverter driven tuning and operating frequencies in kHz

Switch Condition	**Series Inductance**		
	4.7mH	**9.4mH**	**82mH**
Open Circuit	37.43-37.46	36.02-36.08	16.58-16.64
25nF Shunt	37.44-37.46	36.01-36.04	16.53-16.61
Short Circuit	37.44-37.45	36.01-36.07	16.51-16.60
Total Tuning	.01-.02	.01-.07	.04-.13

Using the function generator and digital oscilloscope, the open circuit frequency of the mode that the resonator was operating near is 38.21kHz. The 25nF shunt and short circuit frequency was 38.2kHz. This 10Hz tuning is close to what is observed in operation with the modified Pierce circuit as shown in Table 8 and with the amplifier with separate gain and phase adjustment. The experimentally observed tuning (10Hz at the low end, to 70Hz at the high end) is in close agreement with the approximately 16Hz analytically calculated as the tuning expected for bending mode 8 of the resonator. With the 82mH series inductor the resonator is operating close to bending mode 5 and 6 for which the expected tuning is approximately 16Hz and 43Hz respectively. The experimentally observed tuning of between 40Hz and 130Hz is within this range.

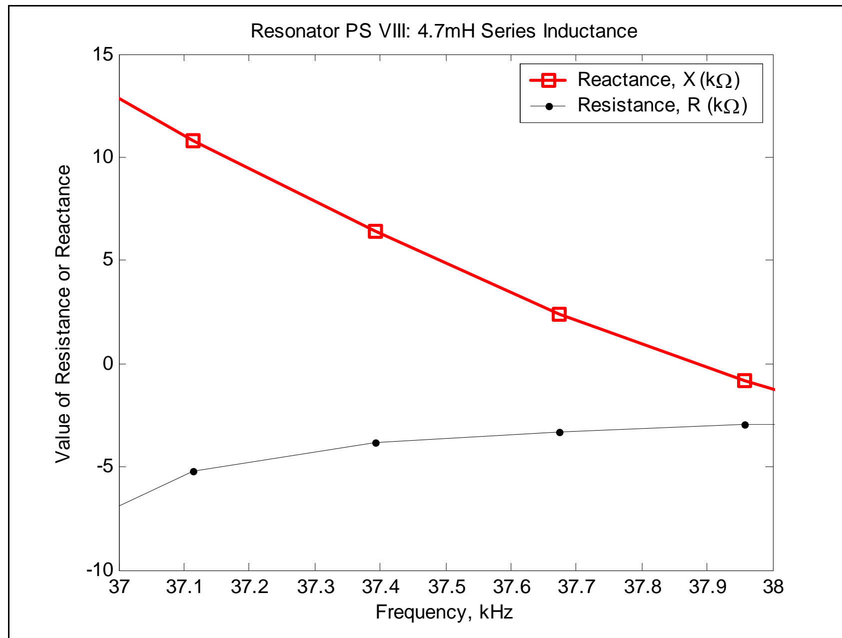

Figure 61. Resistance and Reactance, resonator PS VIII with 4.7mH series inductor

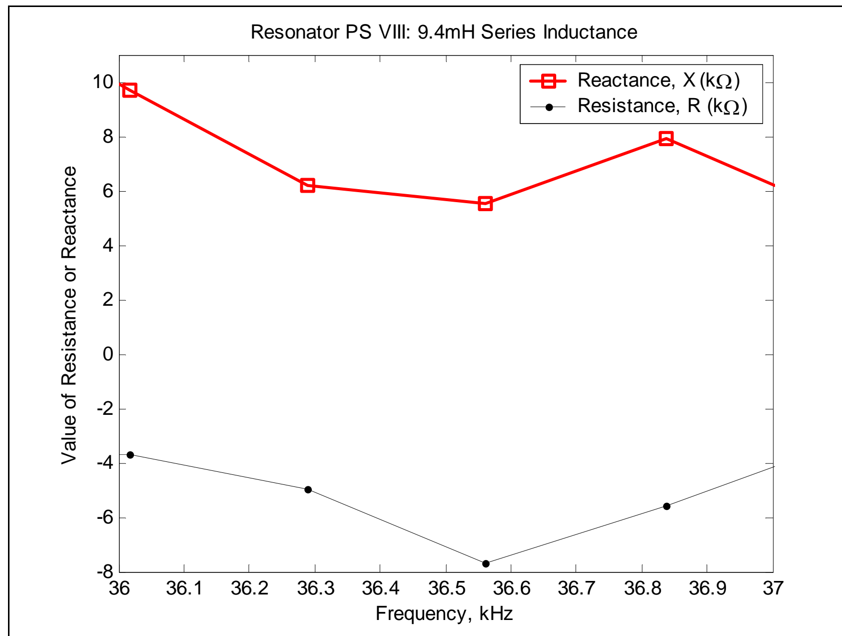

Figure 62. Resistance and Reactance, resonator PS VIII with 9.4mH series inductor

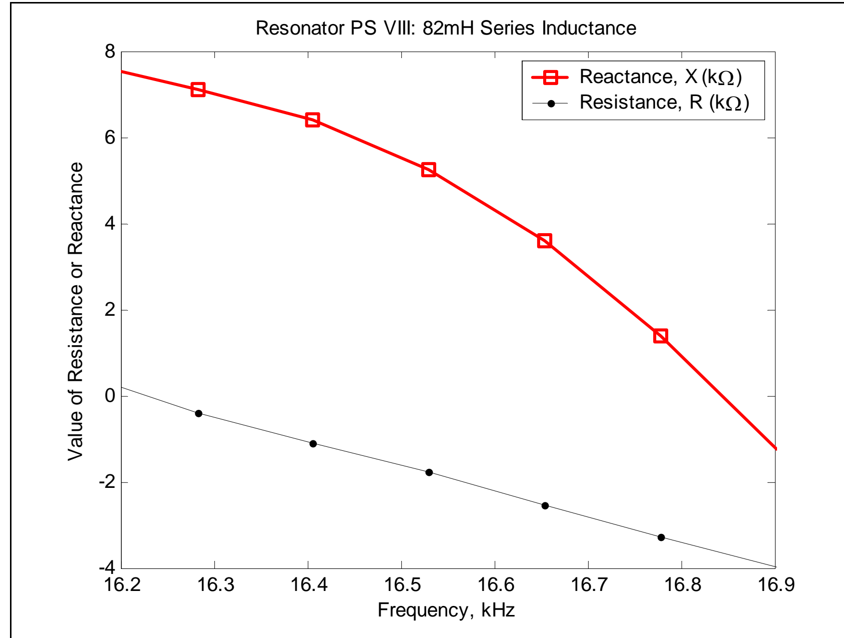

Figure 63. Resistance and Reactance, resonator PS VIII with 82mH series inductor

Figure 61, Figure 62 and Figure 63 show the open circuit reactance and resistance as a function of frequency for resonator PS VIII with a 4.7mH, 9.4mH and 82mH series inductor respectively. From the figures it can be seen that the operational frequency for all the series inductance cases shown in Table 8 are in the positive reactance or inductive region. With the 4.7mH series inductor, the operational frequency was approximately 37.4kHz. From Figure 61, the resistance is approximately 5kΩ and the reactance less than 10kΩ at this frequency. With the 9.4mH series inductor, Figure 62 shows that the resistance and reactance at 36kHz, the operational frequency, are approximately 4kΩ and 10kΩ respectively. With the 82mH series inductor, Figure 63, at the operational frequencies of between 16.51kHz and 16.64kHz the resistance is approximately 2kΩ and the reactance is between approximately 4kΩ and 6kΩ. As will be seen with the other resonators, the resistance at the operational frequency when using the modified Pierce circuit is always below 10kΩ. The reactance at the operational points is also

between a resonance and anti-resonance point on the reactance curve (see data in Figure 64 to Figure 66).

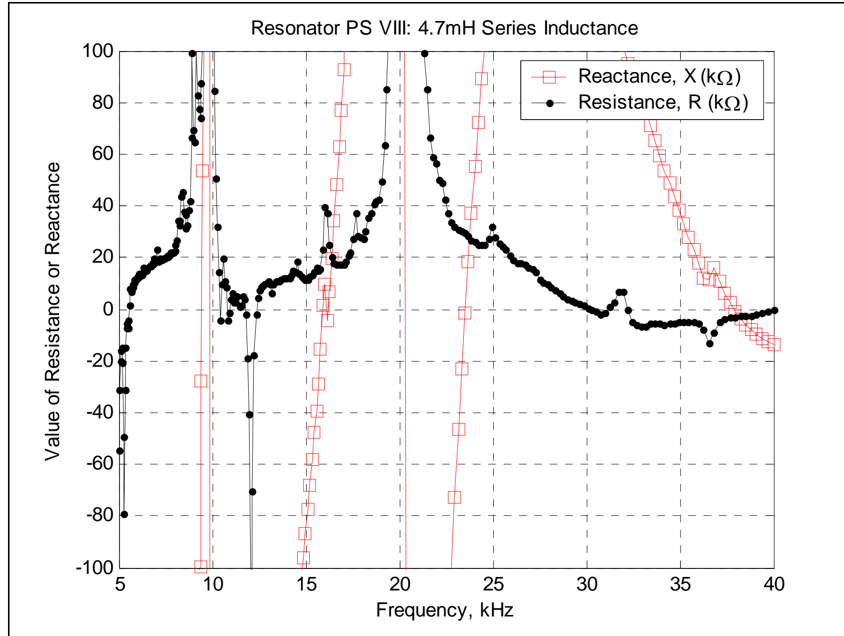

Figure 64. R and X, full range, resonator PS VIII with 4.7mH series inductor

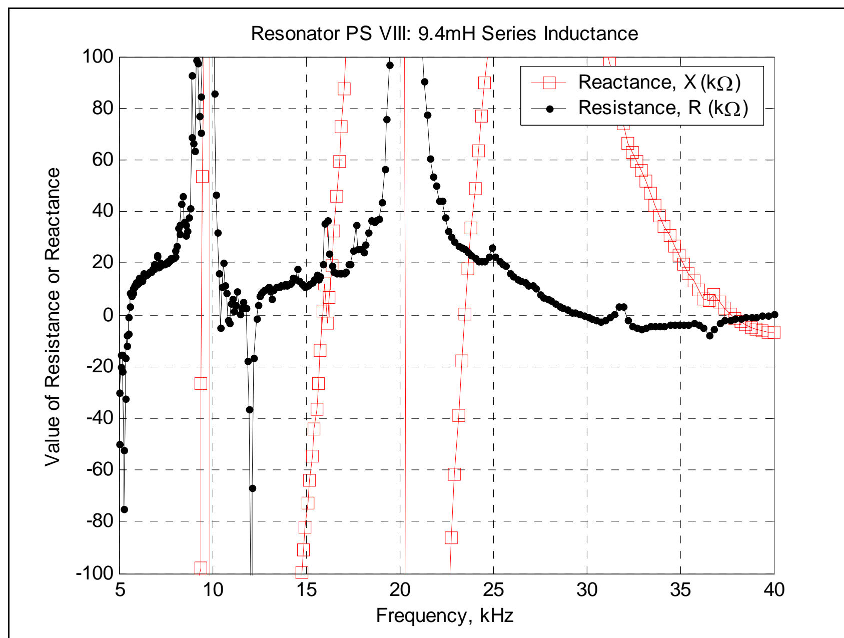

Figure 65. R and X, full range, resonator PS VIII with 9.4mH series inductor

Figure 64 to Figure 66 show the resistance and reactance of resonator PS VIII with various series inductors between 5kΩ and 40kΩ. With the resonator driven by the modified Pierce circuit the operational frequency is expected to be found where the reactance of the resonator is positive or inductive. For a series inductance of 4.7mH and 9.4mH (Figure 64 and Figure 65) the inductive regions of the reactance curves are from approximately 9kHz to 10kHz, 15kHz to 20kHz, and 23kHz and 38kHz. The minimum resistance of the resonator over all the inductive regions, in both cases, is found to be in the last inductive region (between approximately 23kHz and 38kHz) and it is in this region that the resonator operates, as indicated by the data in Table 8. The inductive regions are slightly different for resonator PS VIII with the 82mH series inductor. As can be seen in Figure 66, the inductive regions are between approximately 9kHz and 10kHz, 15kHz and 17kHz, 20kHz and 24kHz, and 37kHz to over 40kHz. The minimum resistance in these inductive regions is found between approximately 15kHz and 17kHz. Again, as seen with the 4.7mH and 9.4mH series inductors, this is the region in which the resonator operates.

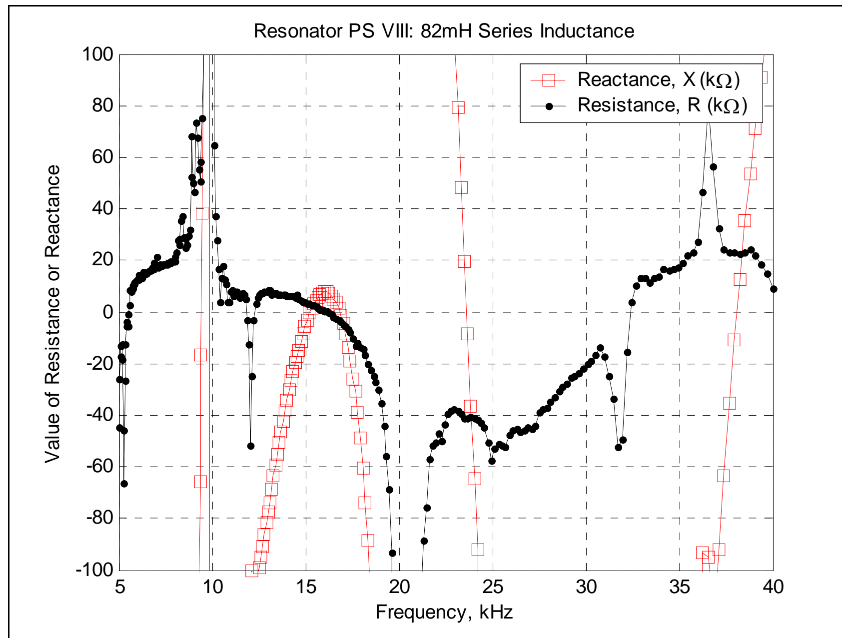

Figure 66. R and X, full range, resonator PS VIII with 82mH series inductor

8.3.2 Resonator PS XII

Table 9. Resonator PS XII inverter driven tuning and operating frequencies in kHz

Switch Condition	Run 1				Run 2			
	Series Inductance				Series Inductance			
	1mH	2mH	4.7mH	9.4mH	1mH	2mH	4.7mH	9.4mH
Open Circuit	33.668	33.654	33.529	32.34-32.4	33.720	33.460	33.325	32.190
25nF Shunt	33.594	33.578	33.453	32.212	33.626	33.372	33.233	32.088
Short Circuit	33.577	33.564	33.434	32.188	33.623	33.357	33.207	32.060
Total Tuning	.091	.09	.095	0.212-0.152	.097	.103	.118	.130

No signal was observed when the amplifier with separate gain and phase adjustment were used to drive the resonator. The tuning and operating frequencies of PS XII using the inverter as the amplifier are summarized in Table 9.

Using the function generator and digital oscilloscope, the open and short circuit frequencies of the mode that the resonator operates on are 34.06kHz and 33.98kHz respectively. This gives a tuning range of 80Hz, which is close to the tuning range when PS XII is operating. The analytically calculated tuning is, as seen before with resonator PS VIII, approximately 16Hz. The tuning observed experimentally when resonator PS XII was driven using the inverter in the modified Pierce circuit is between approximately 90Hz and 212Hz. All the experimentally observed tuning ranges and the analytically calculated tuning range are within an order of magnitude of each other.

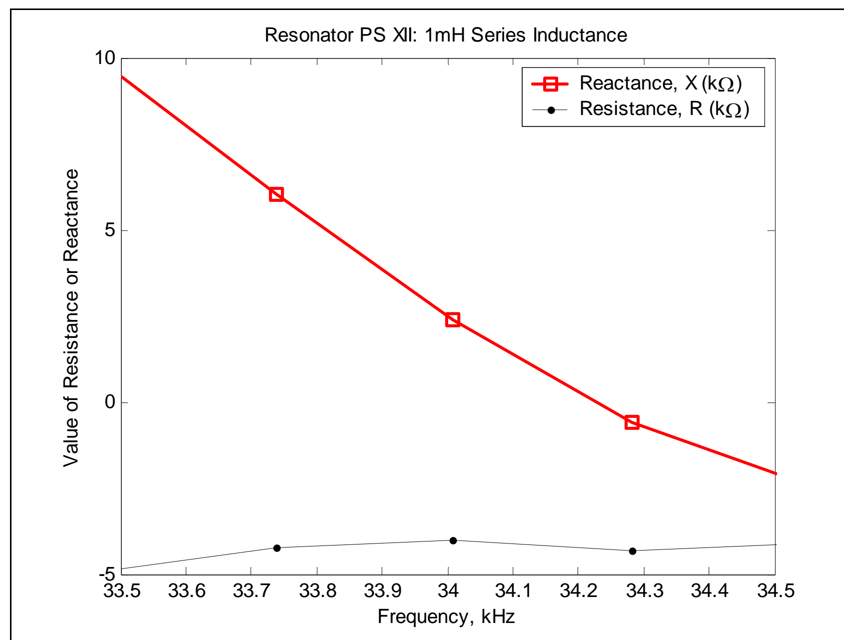

Figure 67. Resistance and Reactance, resonator PS XII with 1mH series inductor

Figure 67 is the reactance and resistance as a function of frequency for resonator PS XII with a 1mH series inductor. The range 33.5kHz to 34.5kHz covers the observed operational frequencies for the 1mH series inductors used in the experiment. As expected the operational frequencies fall in the inductive region of reactance. The maximum resistance at the frequencies of operation of resonator PS XII is approximately 5kΩ at 33.6kHz. The reactance is between 5kΩ and 10kΩ. Figure 68 and Figure 69 show the resistance and reactance data for a 2mH and 4.7mH inductor in series with resonator PS XII. The resistance and reactance values at the operational frequencies of the resonator with the 2mH and 4.7mH series inductors are similar to the values with the 1mH series inductor, i.e. less than 5kΩ for resistance and 10kΩ for reactance.

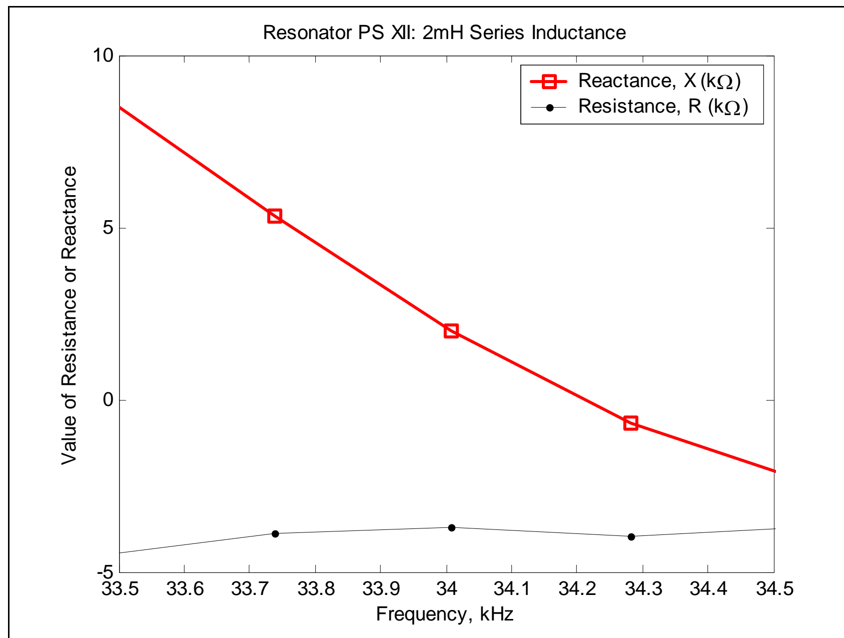

Figure 68. Resistance and Reactance, resonator PS XII with 2mH series inductor

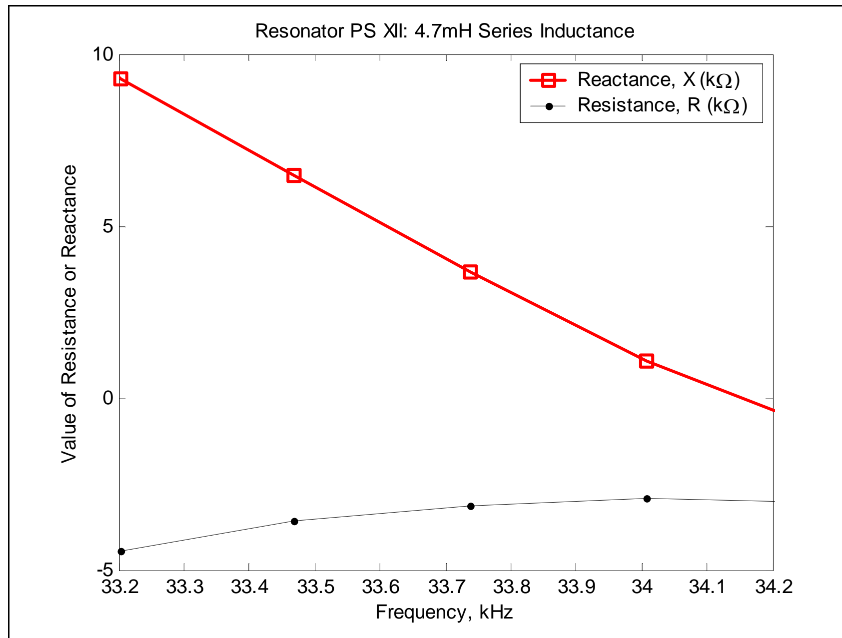

Figure 69. Resistance and Reactance, resonator PS XII with 4.7mH series inductor

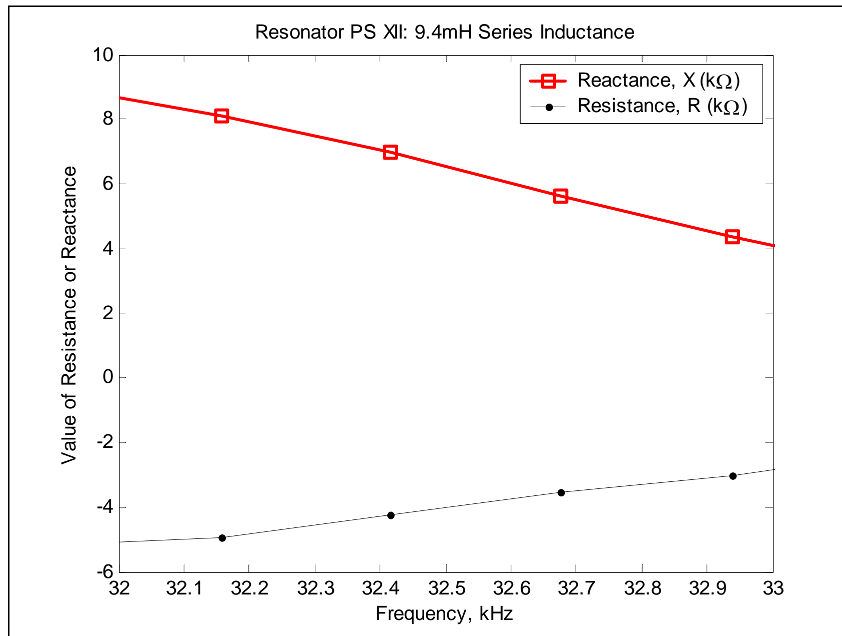

Figure 70. Resistance and Reactance, resonator PS XII with 9.4mH series inductor

The resistance and reactance of resonator PS XII with a 9.4mH series inductor is shown in Figure 70. The resonator is inductive at the operational frequencies with resistance less than

$6k\Omega$ and inductance less than $10k\Omega$. As was seen with resonator PS VIII, the reactance is between a resonance and anti-resonance point in the reactance curve.

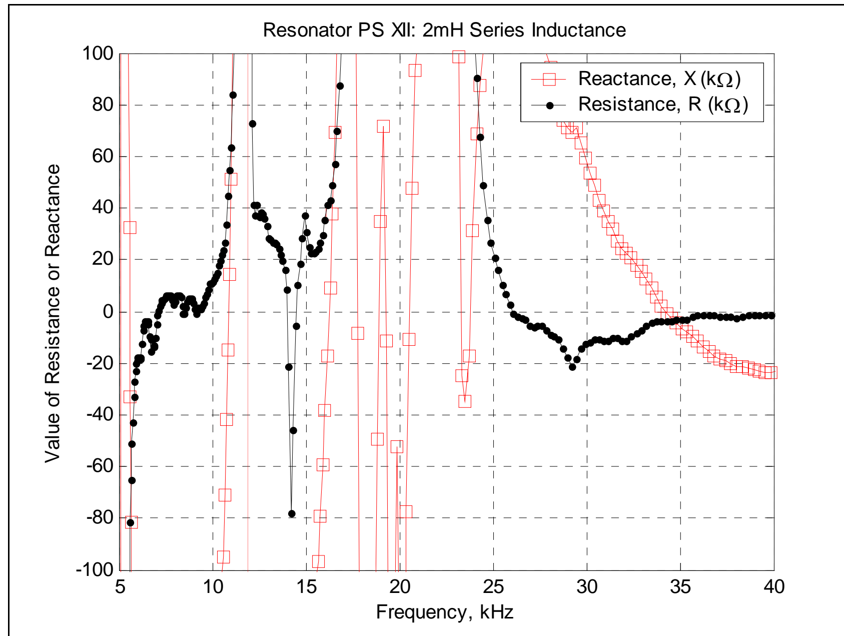

Figure 71. R and X, full range, resonator PS XII with 2mH series inductor

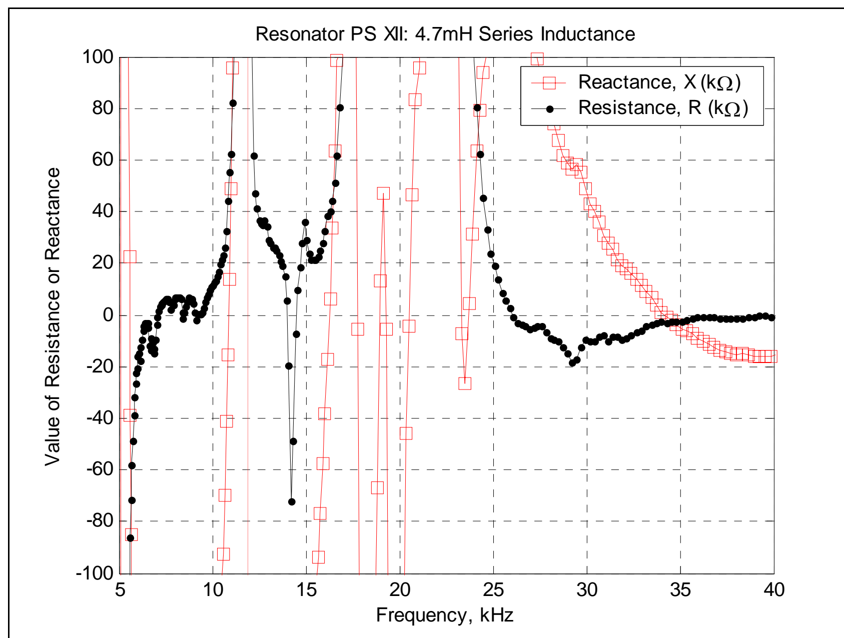

Figure 72. R and X, full range, resonator PS XII with 4.7mH series inductor

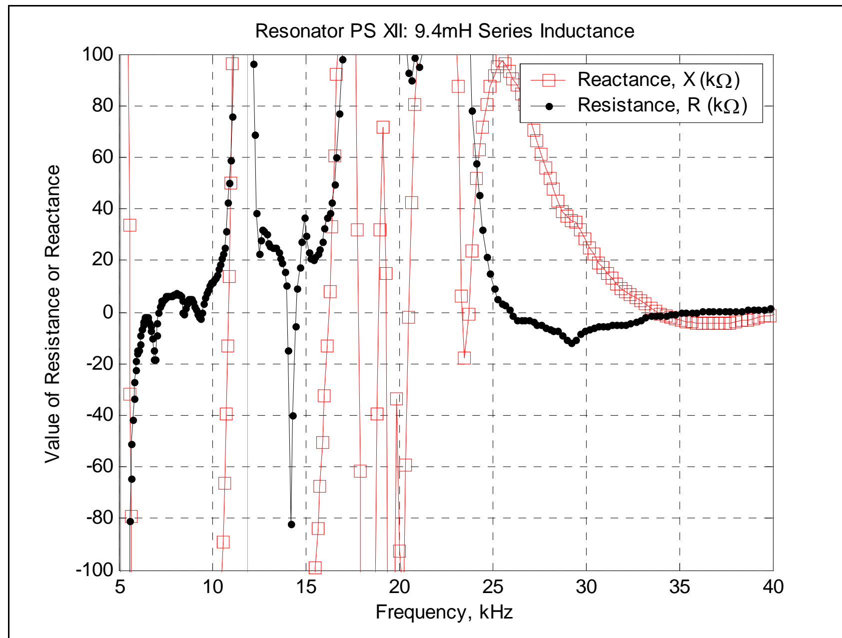

Figure 73. R and X, full range, resonator PS XII with 9.4mH series inductor

The reactance and resistance curves for resonator PS XII with a 2mH, 4.7mH and 9.4mH series inductor are shown in Figure 71, Figure 72 and Figure 73 respectively. The frequency range shown is between 5kHz and 40kHz. The inductive regions of resonator PS XII for these three series inductance are similar: approximately 5kHz to 6kHz, 10kHz to 12kHz, 16kHz to 18kHz, around 19kHz, 20kHz to 23kHz, and 23kHz to 35kHz. The operational frequency of the resonator PS XII (for all the series inductors used) is in between approximately 32kHz and 33.72kHz. This is in the last inductive region (approximately 23kHz to 35kHz). As has been seen previously, this region has the lowest resistance magnitude of all the inductive regions.

8.3.3 Resonator PS XIII

Using the amplifier with separate gain and phase adjustment the open circuit operating frequency was between 34.31kHz and 34.304kHz. Short circuit frequency was between 34.303kHz and 34.309kHz for a tuning range of between 1Hz and 7Hz. The analytically expected tuning range for PS XIII operating at mode 8 is approximately 16Hz. The tuning

observed experimentally using the amplifier with separate gain and phase adjustment was within an order of magnitude of the analytical tuning range.

Table 10 summarizes the operating frequency and tuning shown in operation of resonator PS XIII using an inverter as the amplifier in the modified Pierce circuit. There is no tuning with the 1mH series inductor and a frequency shift of 130Hz with the 2mH inductor. The operational frequency is much higher than observed with the other resonators. Contrary to expectations short circuit frequency is higher than the open circuit frequency.

Table 10. Resonator PS XIII inverter driven tuning and operating frequencies in kHz

Switch Condition	**Series Inductance**	
	1mH	**2mH**
Open Circuit	102.88	102.66
25nF Shunt	102.879	102.70
Short Circuit	102.88	102.79
Total Tuning	0	-.13

The reactance and resistance of resonator PS XIII with a 1mH series inductor is shown in Figure 74. At the operational frequency of the resonator, i.e. approximately 102.9kHz, the reactance and resistance are under $2k\Omega$. As expected the resonator operates inductively with the frequency of vibration between the resonance and anti-resonance frequencies.

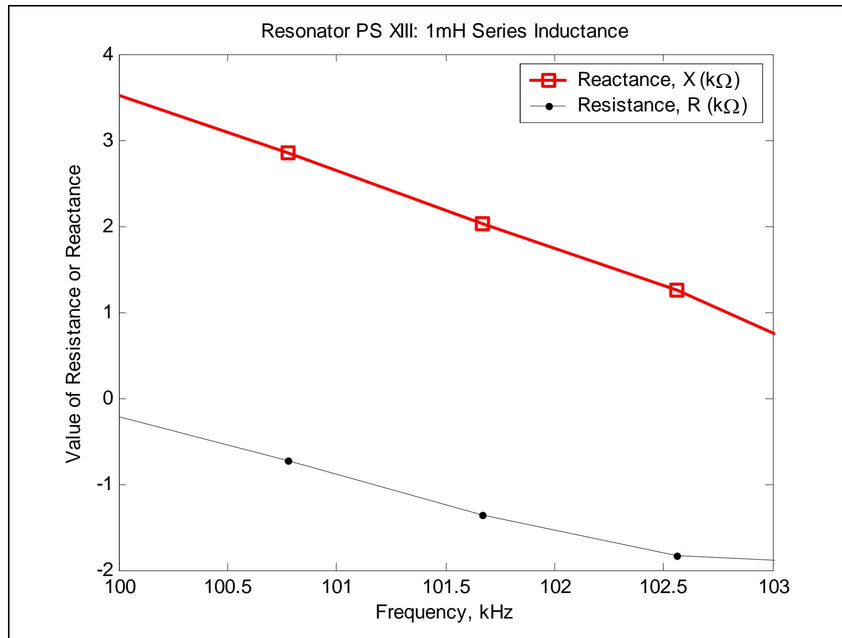

Figure 74. Resistance and Reactance, resonator PS XIII with 1mH series inductor

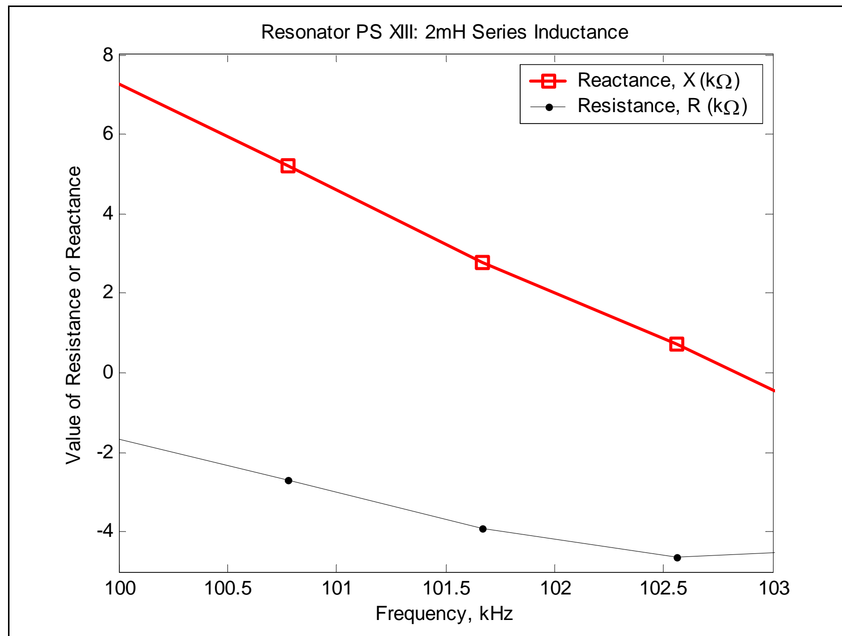

Figure 75. Resistance and Reactance, resonator PS XIII with 2mH series inductor

Figure 75 shows resistance and reactance of resonator PS XIII with a 2mH series inductor. The operational frequency of the resonator is between 102.6kHz and 102.8kHz. The reactance and resistance at these frequencies are below 2kΩ and 5kΩ respectively.

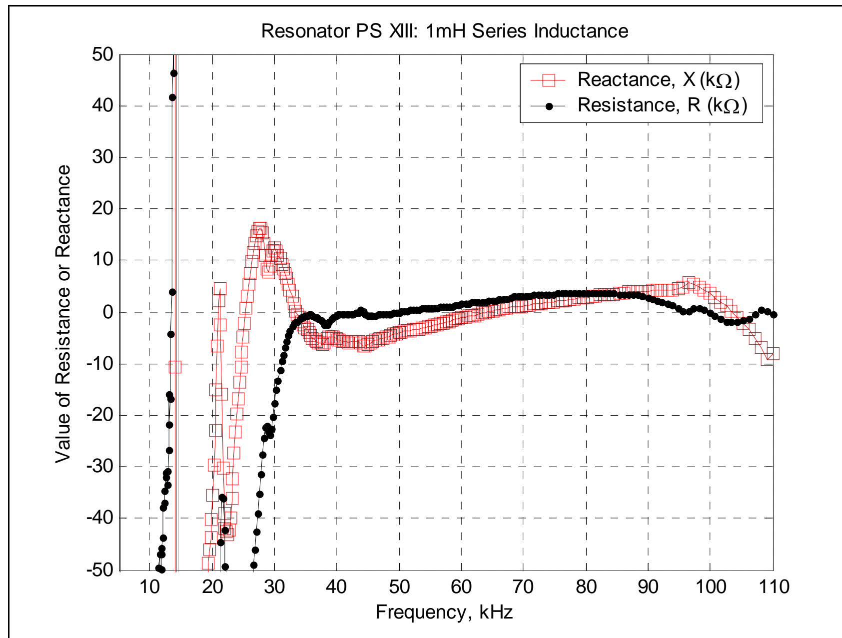

Figure 76. R and X, full range, resonator PS XIII with 1mH series inductor

As can be seen in Figure 76, resonator PS XIII with the 1mH series inductor is inductive in regions near approximately 15kHz, 20kHz, from 25kHz and 35kHz, and from approximately 60kHz to 105kHz. Within these inductive regions, the resistance has the lowest magnitude between 60kHz and 105kHz. This low resistance magnitude region coincides with the operational frequency of the resonator with the 1mH series inductor. Figure 77 shows resistance and reactance curves for resonator PS XIII with a 2mH series inductor. The inductive regions with the 2mH series inductor are the same as was seen with the 1mH inductor with the exception of the last region. PS XIII is inductive from slightly earlier, approximately 40kHz to 105kHz. Again the resistance has the smallest magnitude in this region and the frequency of operation of PS XIII with the modified Pierce circuit is within this region.

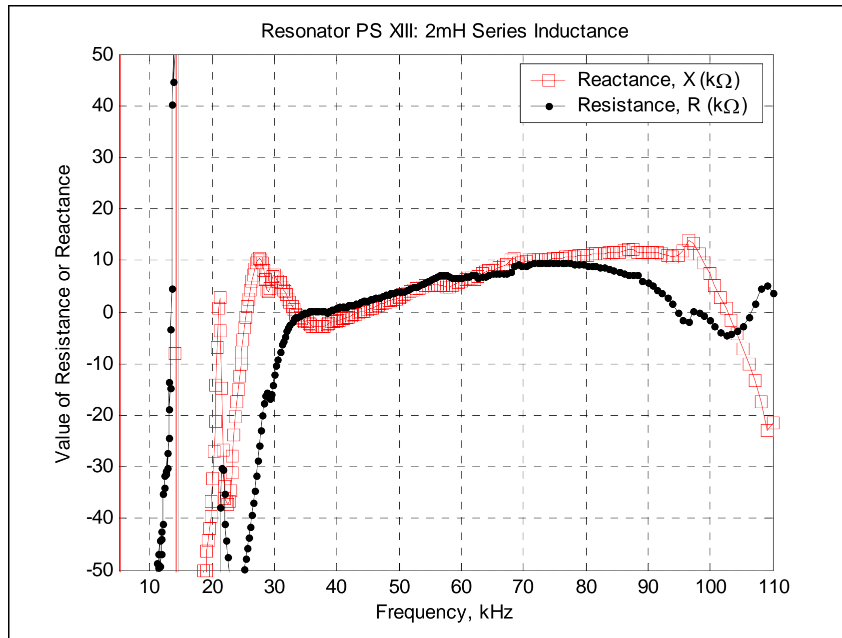

Figure 77. R and X, full range, resonator PS XIII with 2mH series inductor

8.3.4 Resonator PS XIV

Using the amplifier with separate gain and phase adjustment the open circuit frequency was between 37.754kHz and 37.757kHz. The 25nF shunt operating frequency was 37.742kHz and short circuit frequency was 37.741kHz giving a frequency shift of between 13Hz and 16Hz. This gives very good agreement with the analytically calculated tuning range of 16Hz for bending mode 8.

Table 11 summarizes the data obtained when using the inverter in the modified Pierce circuit to drive the resonator. With the 1mH and 2mH series inductors there was very little change in frequency from open to short circuit, 4Hz and –3Hz respectively. There was no frequency change with the 4.7mH and 9.4mH inductors.

Table 11. Resonator PS XIV inverter driven tuning and operating frequencies in kHz

Switch Condition	**Series Inductance**			
	1mH	**2mH**	**4.7mH**	**9.4mH**
Open Circuit	37.691	37.655	37.562	37.204
25nF Shunt	37.687	37.656	37.561	37.203
Short Circuit	37.687	37.658	37.562	37.204
Total Tuning	.004	-.003	0	0

The peak in the open circuit frequency response was found to be at 38.06kHz using the function generator and digital oscilloscope. With the 25nF shunt the peak in the response was at 38.04kHz and short circuit frequency peak was 38kHz. This gives a frequency shift of 60Hz; however, this shift in frequency was not observed in the actual operation of the resonator.

The operational frequency of resonator PS XIV driven by the inverter in the modified Pierce circuit configuration varies from 37.2kHz with a 9.4mH series inductor to approximately 37.7kHz with a 1mH inductor. Figure 78 shows that the resistance of the resonator is approximately 10kΩ at 37.7kHz range and the reactance is positive and approximately 10kΩ as well. The 2mH series inductor data, Figure 79, is similar to the 1mH data; the resistance and reactance are both approximately 10kΩ.

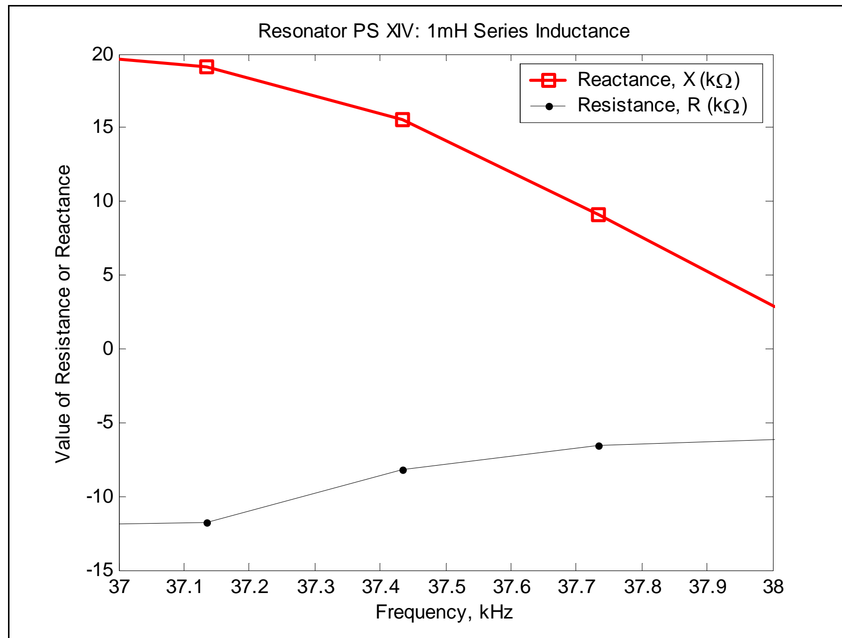

Figure 78. Resistance and Reactance, resonator PS XIV with 1mH series inductor

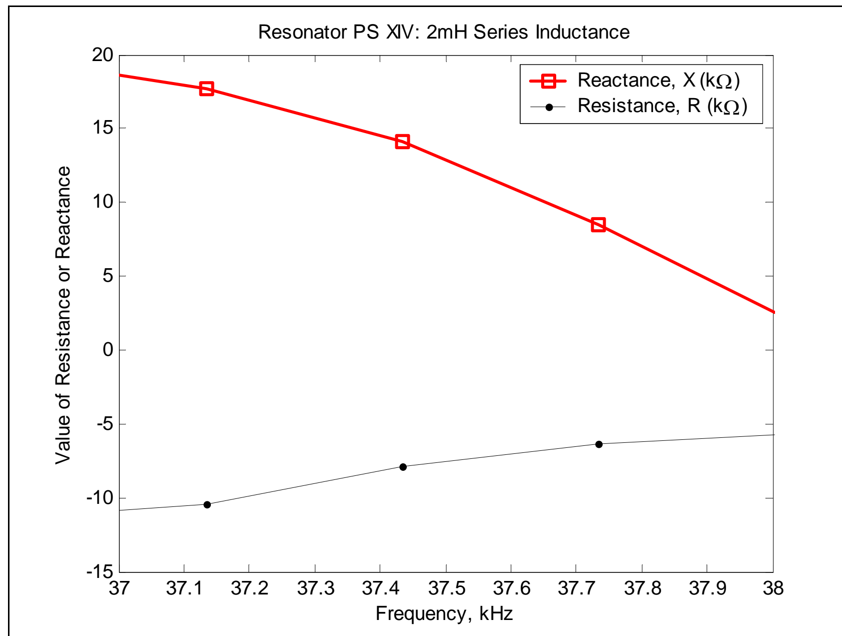

Figure 79. Resistance and Reactance, resonator PS XIV with 2mH series inductor

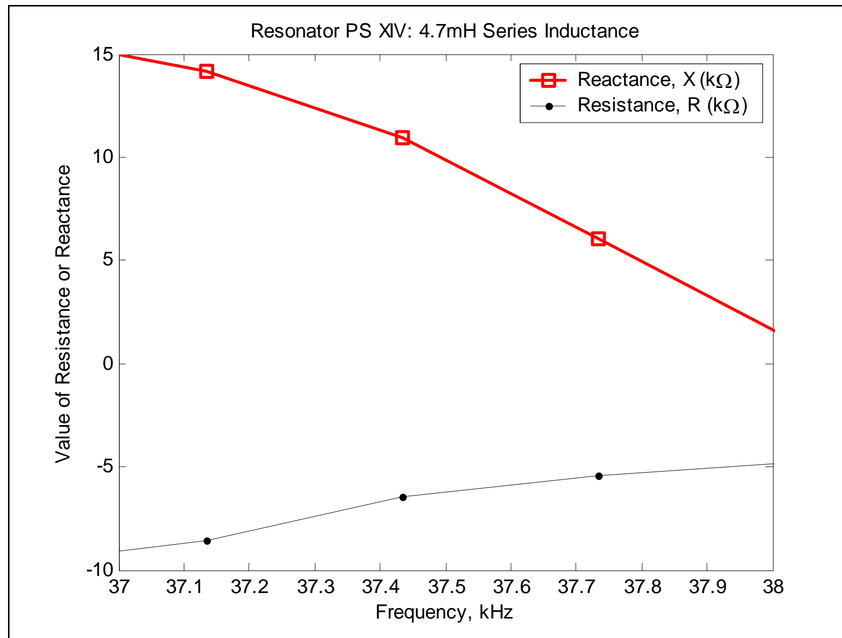

Figure 80. Resistance and Reactance, resonator PS XIV with 4.7mH series inductor

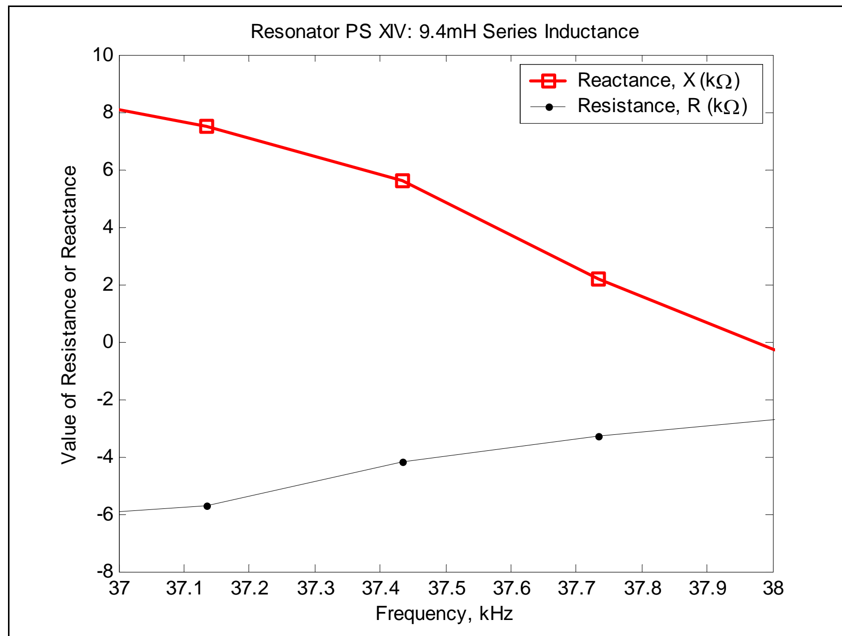

Figure 81. Resistance and Reactance, resonator PS XIV with 9.4mH series inductor

With 4.7mH series inductance, Figure 80, and 9.4mH series inductance, Figure 81, the inductance and resistance at the operational frequencies is approximately 10kΩ. In Figure 78

to Figure 81 it can be seen that increasing the series inductance causes a reduction in the magnitudes of both the reactance and resistance over the frequency range 37kHz to 38kHz. All the operational points of the resonator are in the inductive region between a resonance and anti-resonance point with low resistance.

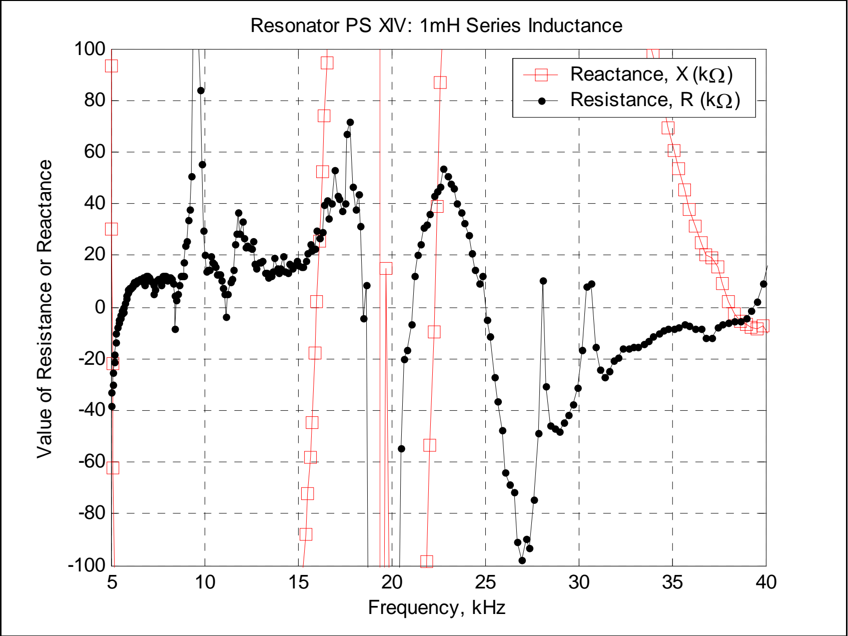

Figure 82. R and X, full range, resonator PS XIV with 1mH series inductor

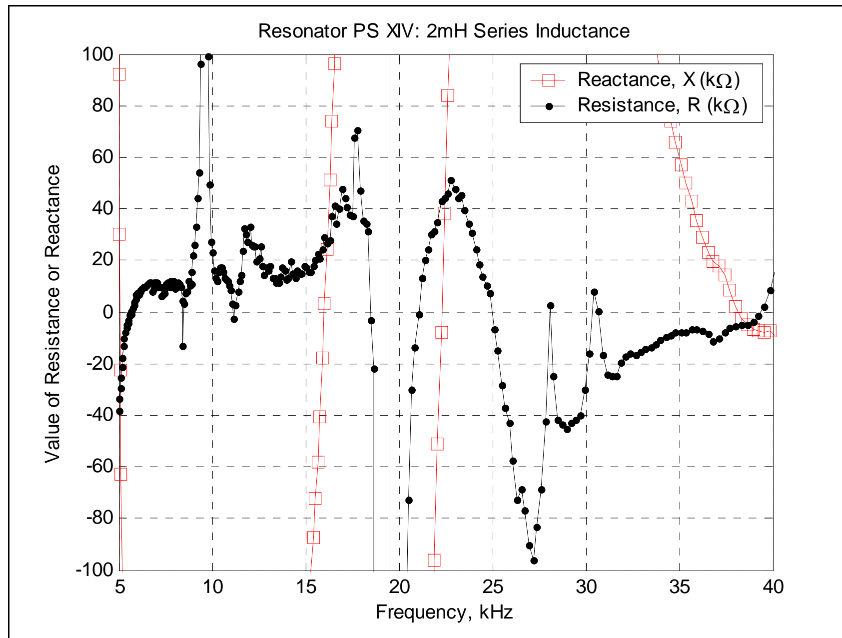

Figure 83. R and X, full range, resonator PS XIV with 2mH series inductor

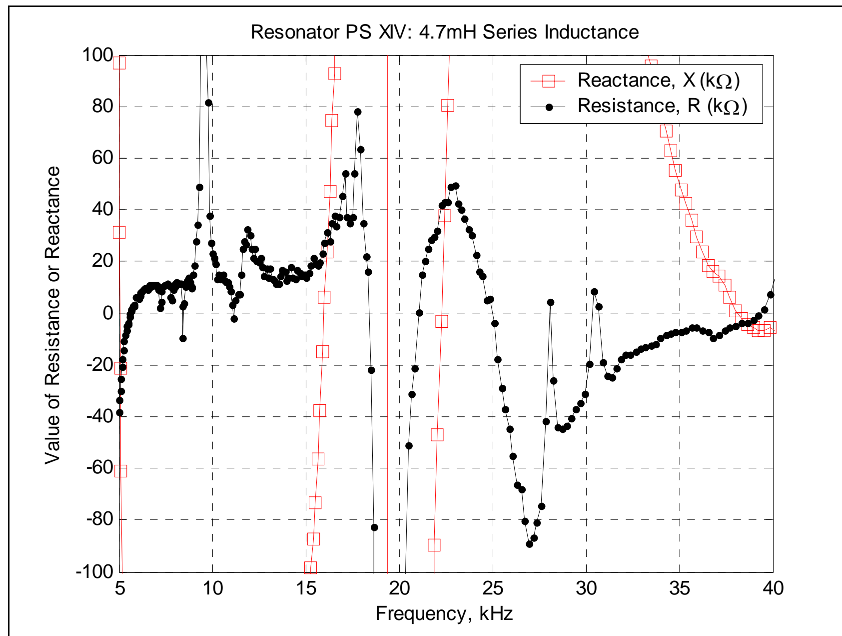

Figure 84. R and X, full range, resonator PS XIV with 4.7mH series inductor

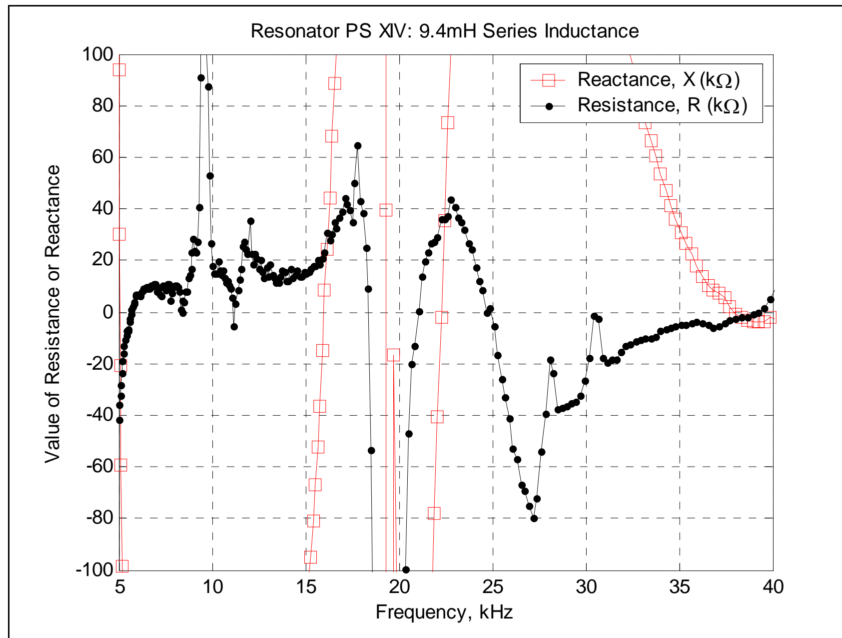

Figure 85. R and X, full range, resonator PS XIV with 9.4mH series inductor

Resonator PS XIV resistance and reactance curves from 5kHz to 40kHz for 1mH, 2mH, 4.7mH and 9.4mH series inductors are shown in Figure 82, Figure 83, Figure 84 and Figure 85 respectively. The inductive regions are the same for all the inductance cases: 16kHz to 19kHz, and 22kHz to 38kHz. The frequency of operation of resonator PS XIV for all inductance cases in the modified Pierce configuration spans the frequencies from approximately 37.2kHz to 37.7kHz. These frequencies are within the higher of the two inductive regions of resonator PS XIV and, as can be seen in Figure 82 to Figure 85 , coincide with the lowest resistance magnitudes.

8.3.5 Resonator PS XV

Using the amplifier with separate gain and phase adjustment the open circuit frequency of operation was 20.505kHz to 20.506kHz. The 25nF shunt operating frequency was 20.492kHz to 20.495kHz. The short circuit frequency of operation was 20.496kHz to 20.498kHz. This gives a total tuning of between 7Hz and 10Hz. Frequencies near 20.5kHz correspond to mode 6

operation of the resonator. The analytically calculated tuning range for bending mode 6 is approximately 43Hz. The experimentally observed tuning range is therefore within an order of magnitude of the analytical tuning value.

The frequency and tuning when the resonator was driven by an inverter in the modified Pierce circuit is summarized in Table 12. The maximum tuning observed was 80Hz with the resonator operating at 312.9kHz. There was little to no tuning with series inductance of 2mH and higher.

Table 12. Resonator PS XV inverter driven tuning and operating frequencies in kHz

Switch Condition	**Series Inductance**			
	1mH	**2mH**	**4.7mH**	**9.4mH**
Open Circuit	312.9	32.428	32.38	32.279
25nF Shunt	312.85	32.427	32.38	32.275
Short Circuit	312.82	32.427	32.38	32.276
Total Tuning	.08	.001	0	.003

With the function generator and digital oscilloscope, the peak open circuit and 25nF shunt responses near the operating frequency of the resonator were at 32.54kHz. The short circuit peak was at 32.535kHz, giving a frequency shift of 5Hz. Operation at 32kHz corresponds to mode 7 vibration and the analytically calculated tuning range is 4Hz. The 5Hz tuning observed using the function generator – oscilloscope combination, and the up to 3Hz observed in the modified Pierce configuration are, consequently, very close to the analytically calculated value.

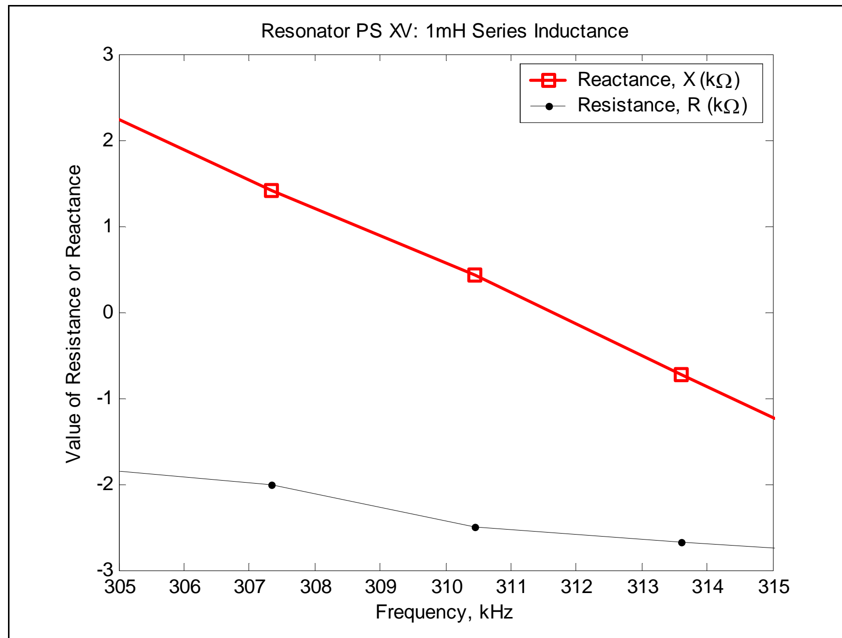

Figure 86. Resistance and Reactance, resonator PS XV with 1mH series inductor

Figure 86 shows that the magnitude of the resistance and reactance is less than 3kΩ at the operating frequency of resonator PS XV with a 1mH series inductor.

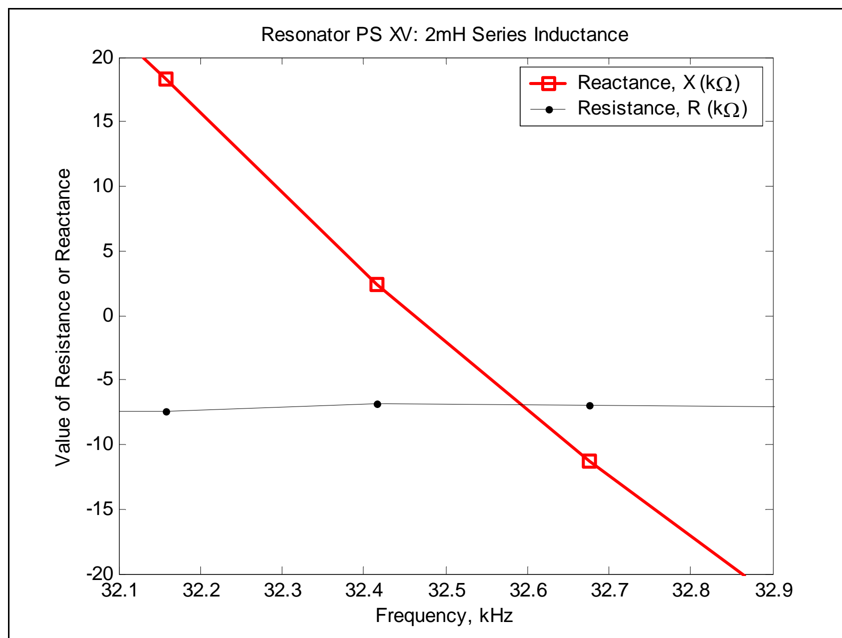

Figure 87. Resistance and Reactance, resonator PS XV with 2mH series inductor

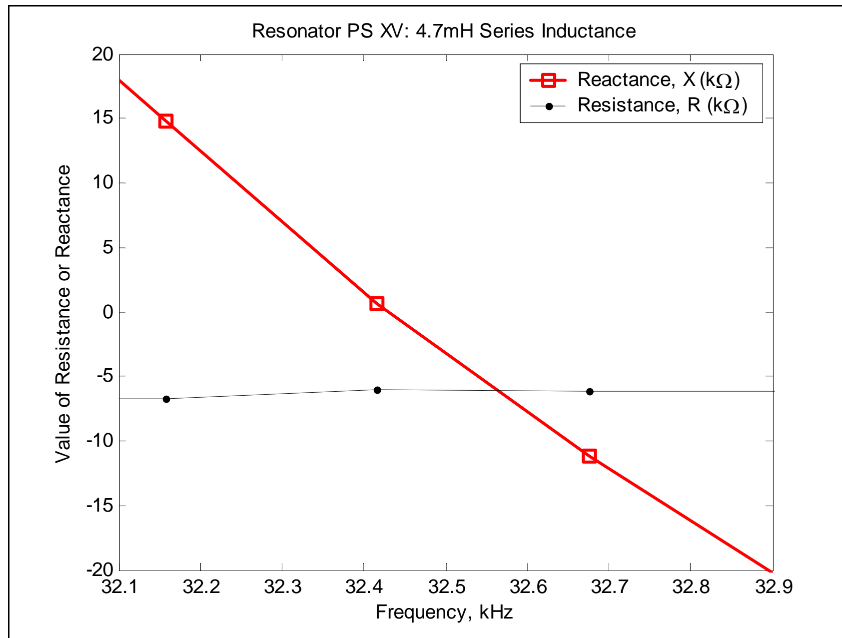

Figure 88. Resistance and Reactance, resonator PS XV with 4.7mH series inductor

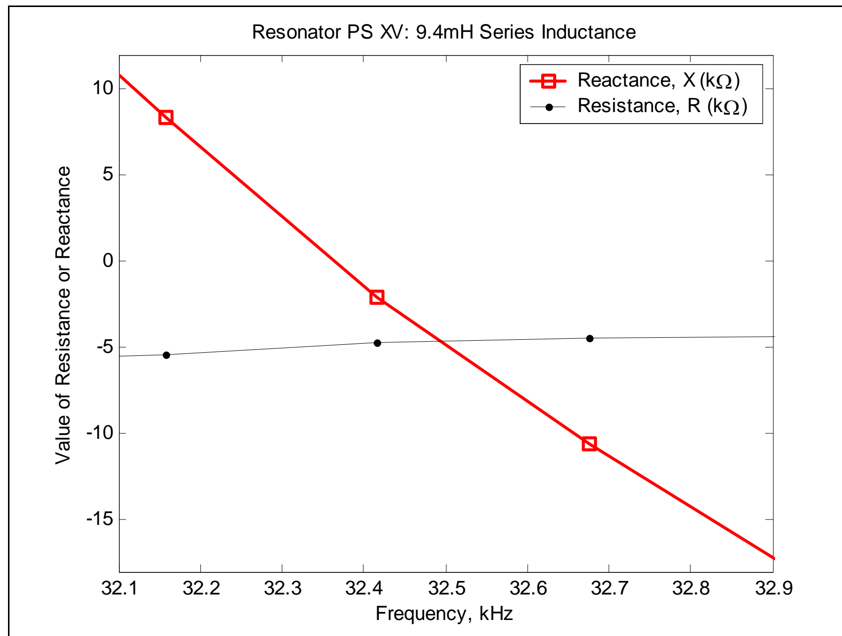

Figure 89. Resistance and Reactance, resonator PS XV with 9.4mH series inductor

The data for resonator PS XV with a 2mH, 4.7mH and 9.4mH series inductor is shown in Figure 87 to Figure 89. The resistance and reactance magnitudes are less than 10kΩ at the frequency of operation. As was seen in the data for resonator PS XIV, increasing the series inductance

causes reductions in the magnitude of both the reactance and resistance. The operational frequencies are all in the inductive region of the impedance curve.

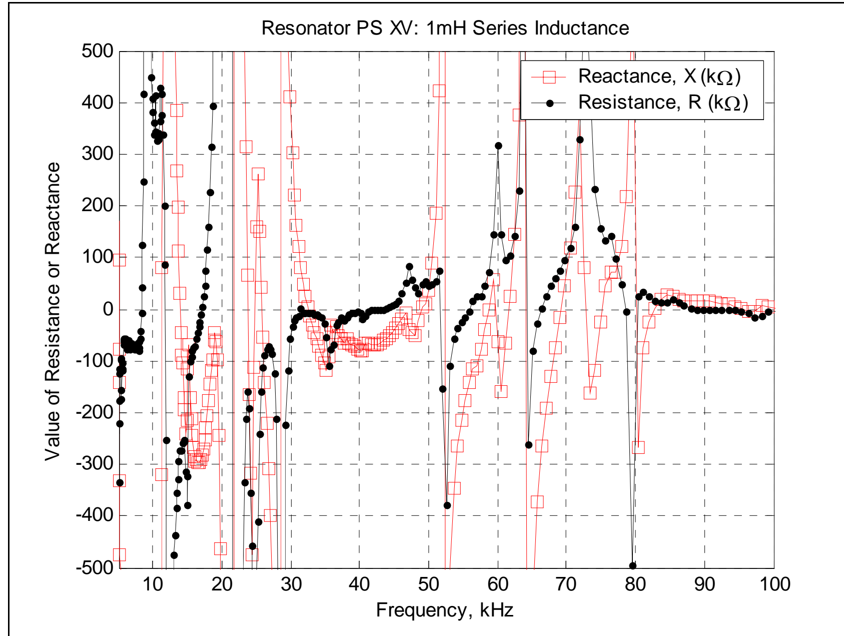

Figure 90. R and X, 5kHz to 100kHz, resonator PS XV with a 1mH series inductor

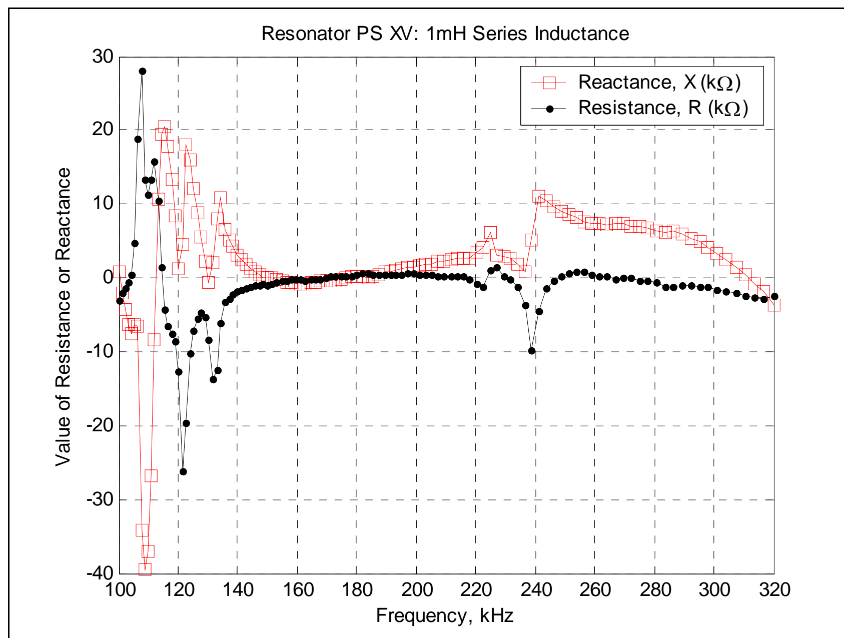

Figure 91. R and X, 100kHz to 320kHz, resonator PS XV with a 1mH series inductor

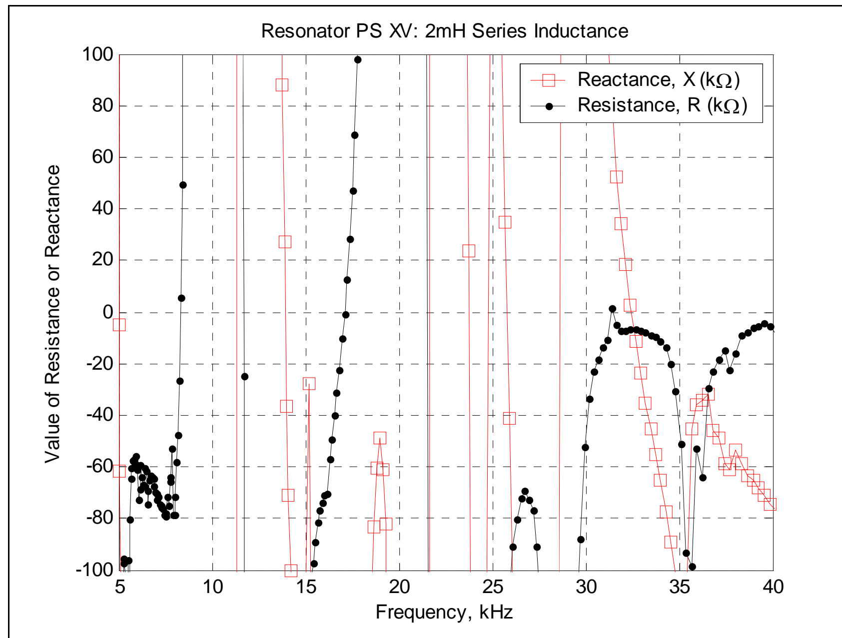

Figure 92. R and X, full range, resonator PS XV with 2mH series inductor

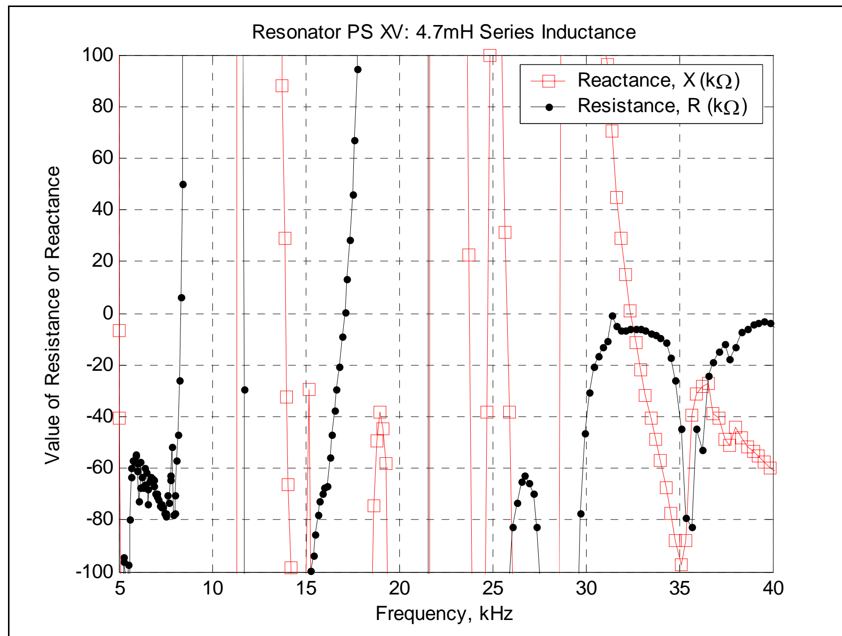

Figure 93. R and X, full range, resonator PS XV with 4.7mH series inductor

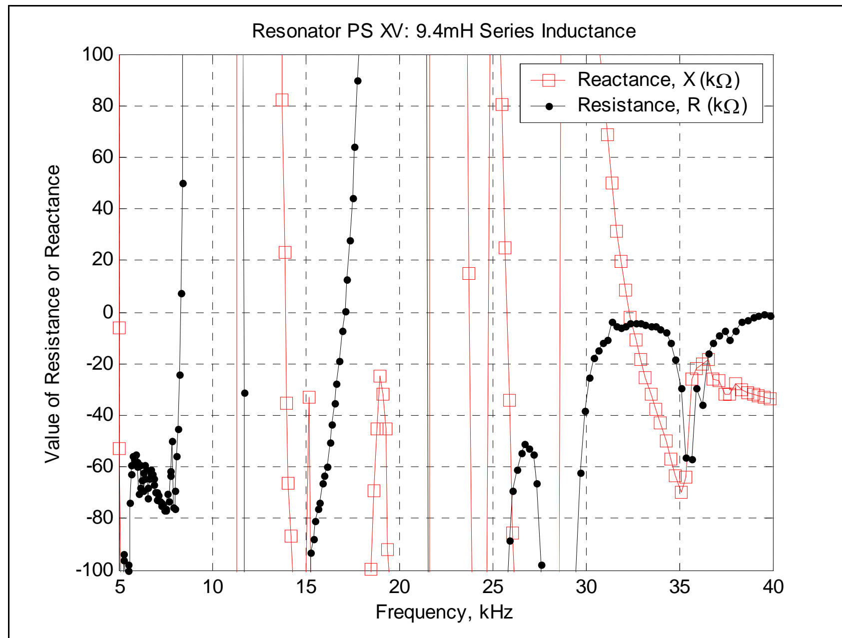

Figure 94. R and X, full range, resonator PS XV with 9.4mH series inductor

The resistance and reactance curves for resonator PS XV in Figure 90 to Figure 94 show several regions of positive reactance. Looking at the curves for the resonator with the 1mH series inductor, Figure 90 and Figure 91, we see that there are a multitude of inductive regions. For frequencies below 100kHz the lowest resistance in an inductive region is between 20kΩ and –18kΩ in the region from 82kHz to 95kHz. Above 100kHz the lowest resistance values in an inductive regions are between 2kΩ and –10kΩ in the region from 170kHz to 310kHz.

For the 2mH, 4.7mH and 9.4mH series inductances, the positive reactance region between approximately 29kHz and 33kHz is where the magnitude of resistance is at a minimum. The operating frequencies of between 32.4kHz and 32.2kHz fall in this region.

8.3.6 Resonator PS XVI

Using the amplifier with separate gain and phase adjustment to drive the resonator the open circuit frequency of operation was 40.227kHz, the 25nF shunt frequency was 40.221kHz and the

short circuit frequency was 40.226kHz. This is a frequency shift of about 1Hz. These frequencies correspond to bending mode 8 operation of resonator PS XVI. The expected tuning range is 16Hz.

The data obtained when driving resonator PS XVI using the inverter driven modified Pierce circuit is shown in Table 13 and Table 14. The frequency shift observed is between 18Hz for switching on mode 6 (18kHz) and 229Hz for mode 8 switching. The analytically calculated tuning range is approximately 43Hz for mode 6 and 16Hz for mode 8. The tuning observed using both amplifier schemes is within an order of magnitude of the expected frequency shift.

Table 13. Resonator PS XVI inverter driven tuning and operating frequencies in kHz, run 1

Switch Condition	**Series Inductance**					
	1mH	**2mH**	**4.7mH**	**9.4mH**	**14.1mH**	**82mH**
Open Circuit	39.535	39.495	39.378	35.749	35.086	18.767
25nF Shunt	39.480	39.439	39.331	35.560	34.940	18.744
Short Circuit	39.470	39.429	39.322	35.520	34.906	18.740
Total Tuning	.065	.066	.056	.229	.180	.027

The open circuit, 25nF shunt and short circuit peaks in frequency response using the digital oscilloscope and frequency generator were 40.115kHz, 40.03kHz and 40.025kHz respectively. This gives a tuning range of 90Hz, which is comparable to the range observed during the operation of the resonator using an inverter as the amplifier and the analytical tuning range.

Table 14. Resonator PS XVI inverter driven tuning and operating frequencies in kHz, run 2

Switch Condition	Series Inductance					
	1mH	**2mH**	**4.7mH**	**9.4mH**	**14.1mH**	**82mH**
Open Circuit	39.617	39.568	39.446	35.823	35.212	18.802-18.793
25nF Shunt	39.556	39.513	39.398	35.634	35.060	18.771-18.781
Short Circuit	39.545	39.501	39.389	35.597	35.025	18.765-18.775
Total Tuning	.072	.067	.057	.226	.187	.018-.037

Figure 95 and Figure 96 show the measured resistance and reactance as a function of frequency for resonator PS XVI with a 1mH and 2mH series inductor, respectively, between 39kHz and 40kHz. The operational frequency with the 1mH inductor is between approximately 39.47kHz and 39.62kHz. Over this range, the maximum reactance and resistance of resonator PS XVI is just less than $10k\Omega$. The operational frequency, reactance and resistance ranges of the resonator with the 2mH inductor are approximately 39.43kHz to 39.57kHz and $5k\Omega$ to $10k\Omega$ for both resistance and reactance.

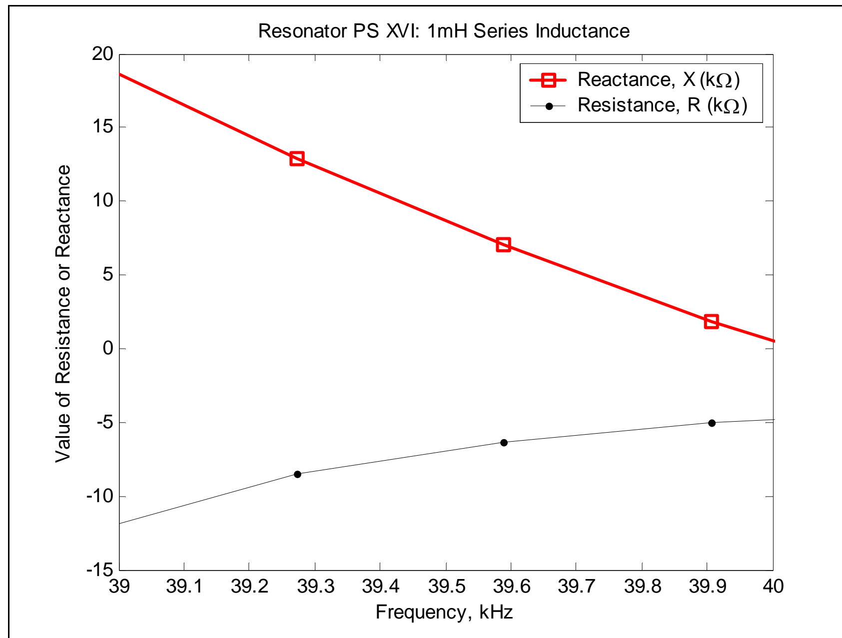

Figure 95. Resistance and Reactance, resonator PS XVI with 1mH series inductor

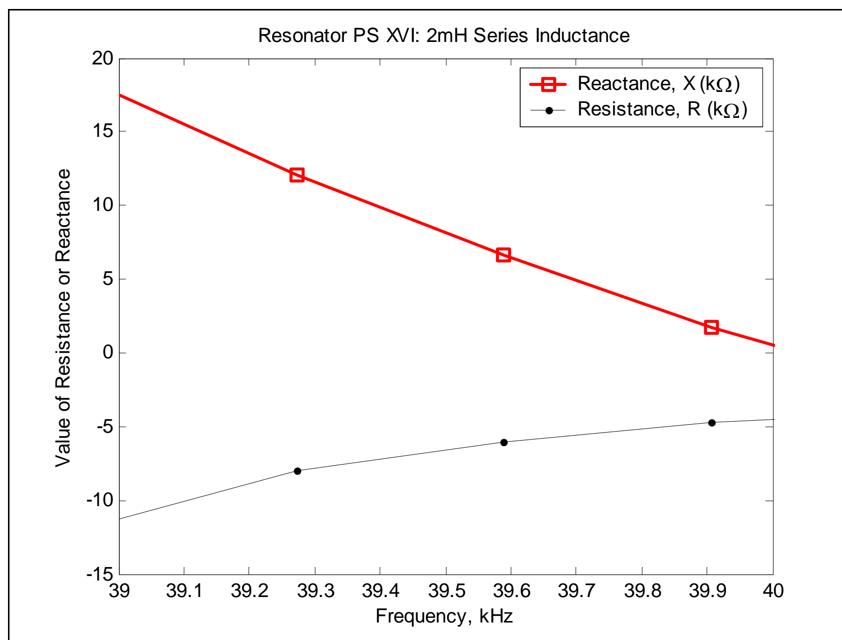

Figure 96. Resistance and Reactance, resonator PS XVI with 2mH series inductor

The measured resistance and reactance with 4.7mH and 9.4mH series inductors is shown in Figure 97 and Figure 98 respectively. The 4.7mH series inductor operational frequency range is 39.32kHz to 39.45kHz. The reactance is between 5kΩ and 10kΩ over this range. The resistance is approximately 5kΩ. With the 9.4mH series inductor the operational frequency range of resonator PS XVI over the two test runs and different switch conditions is between 35.52kHz and 35.82kHz. The measured resistance, as can be seen in Figure 98, is less than 5kΩ and does not change much between 39kHz and 40kHz. The measured reactance is between 5kΩ and 10kΩ.

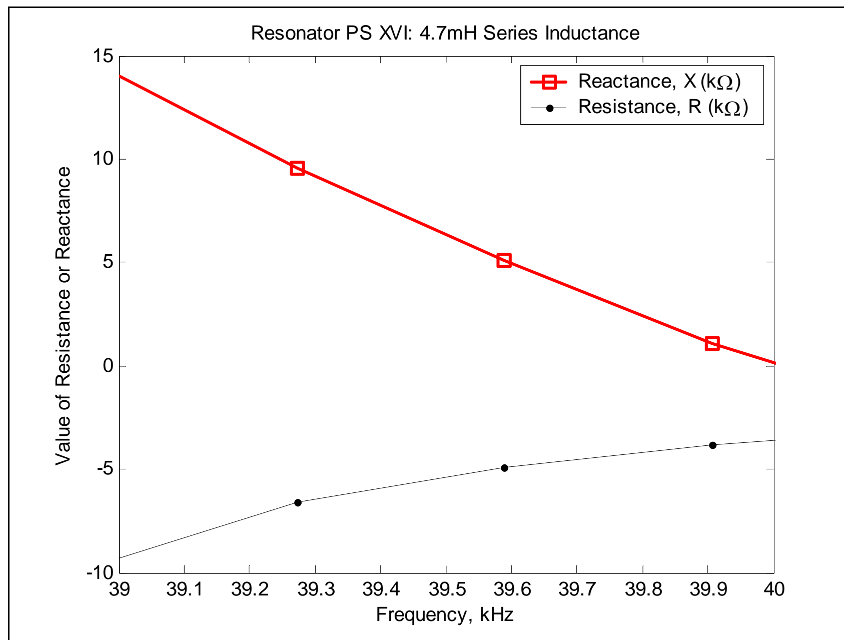

Figure 97. Resistance and Reactance, resonator PS XVI with 4.7mH series inductor

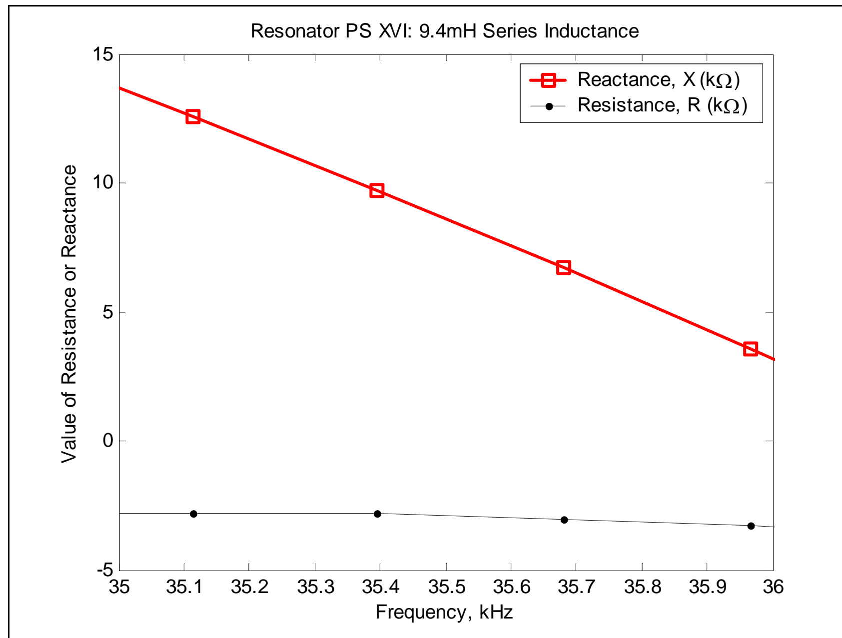

Figure 98. Resistance and Reactance, resonator PS XVI with 9.4mH series inductor

Figure 99 is the 14.1mH series inductor measured resistance and reactance data. During the data acquisition the measurement bridge in the impedance analyzer was unbalanced producing data in MΩ (three orders of magnitude different than the other data obtained); the data may not be valid. In general, the same trend in the data is observed. The reactance data is at a higher value at 39kHz gradually reducing in value to 40kHz. Over the same range the resistance approaches zero from below.

In the data in Figure 95 to Figure 98 the data follows the same trends that were seen in data from resonators PS XIV and PS XV. As the series inductance is increased, the magnitude of the resistance and reactance reduces over the frequency range shown, which is near the operational frequency. In addition, all the operational points are inductive (positive reactance) between a resonance and anti-resonance point with low resistance and reactance magnitudes.

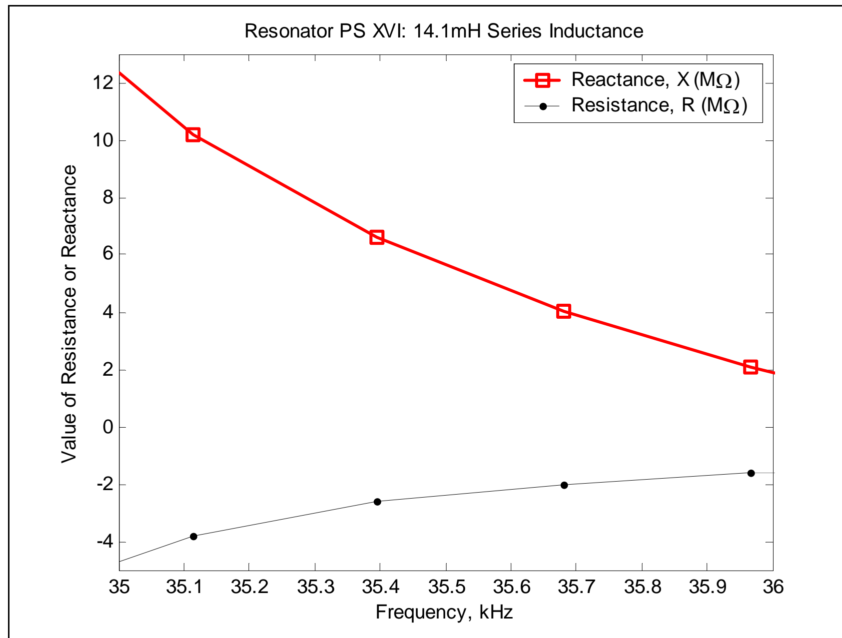

Figure 99. Resistance and Reactance, resonator PS XVI with 14.1mH series inductor

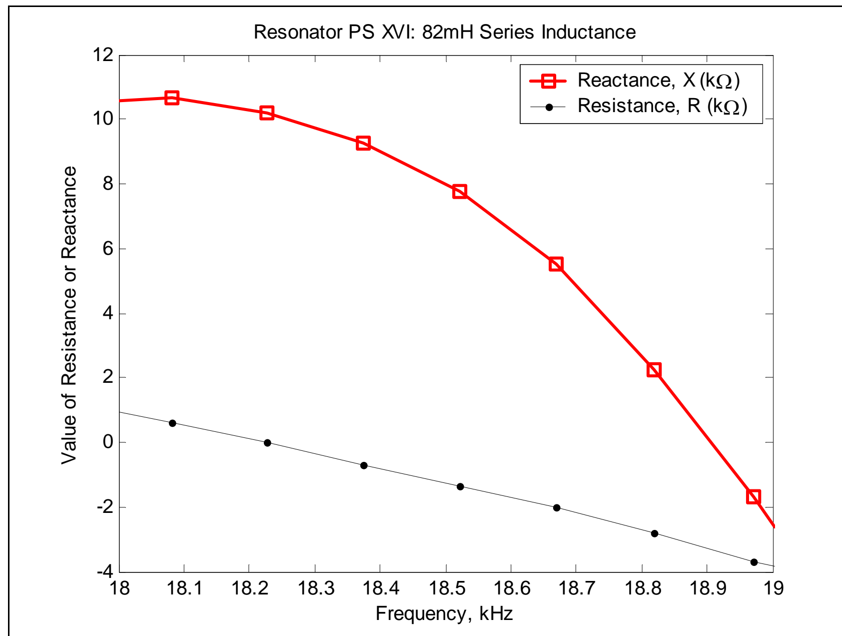

Figure 100. Resistance and Reactance, resonator PS XVI with 82mH series inductor

With the 82mH series inductor the frequency of operation of the resonator ranged from 18.74kHz to approximately 18.80kHz. As can be seen in Figure 100, the resistance at these frequencies is approximately 2kΩ. The reactance is less than 4kΩ.

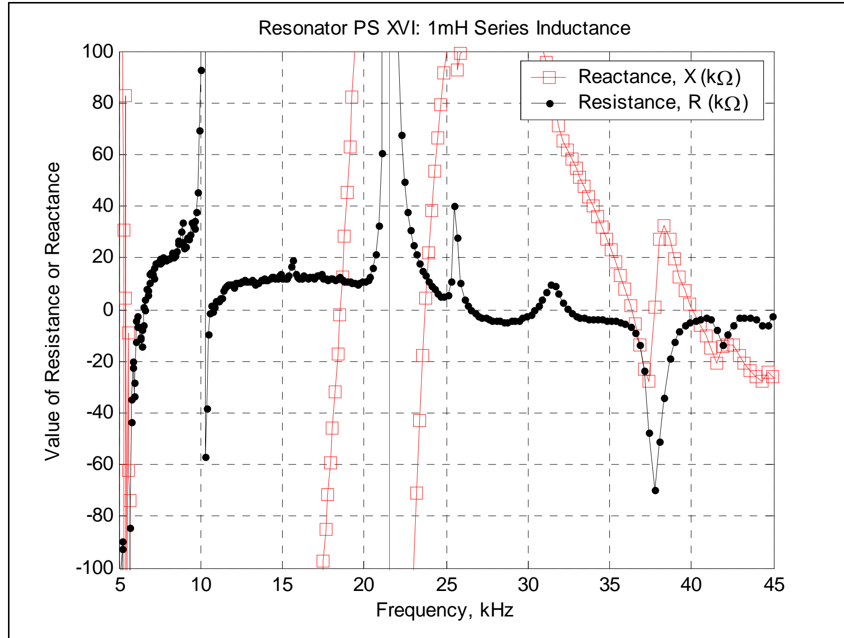

Figure 101. R and X, full range, resonator PS XVI with 1mH series inductor

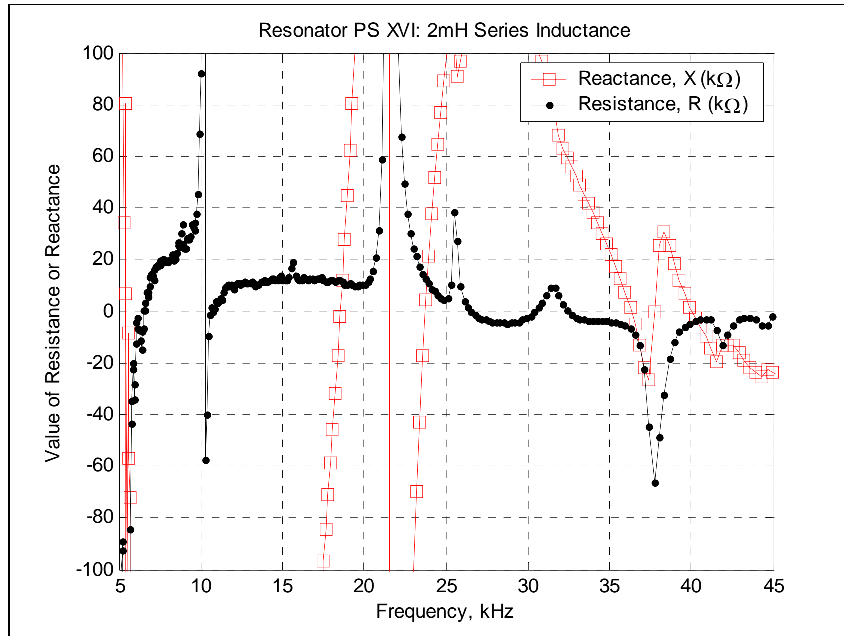

Figure 102. R and X, full range, resonator PS XVI with 2mH series inductor

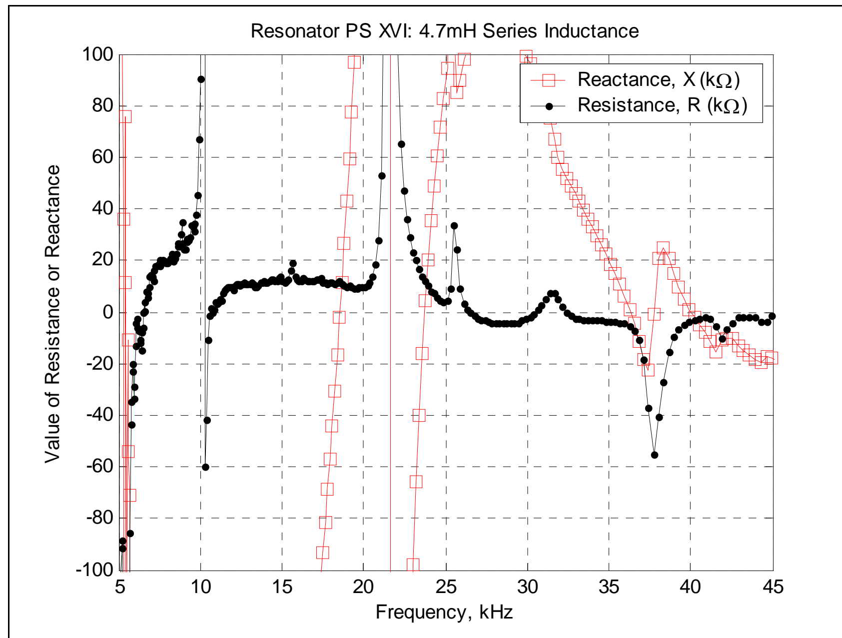

Figure 103. R and X, full range, resonator PS XVI with 4.7mH series inductor

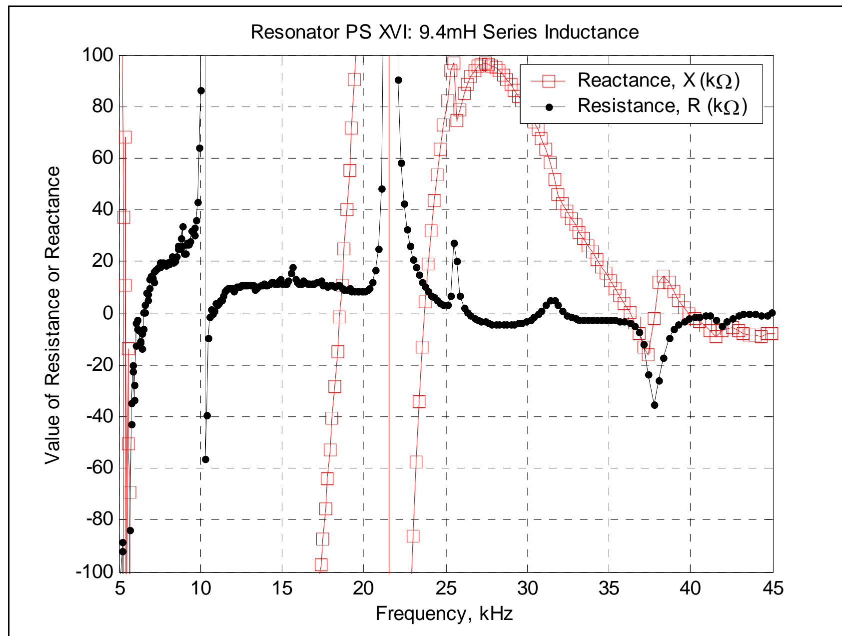

Figure 104. R and X, full range, resonator PS XVI with 9.4mH series inductor

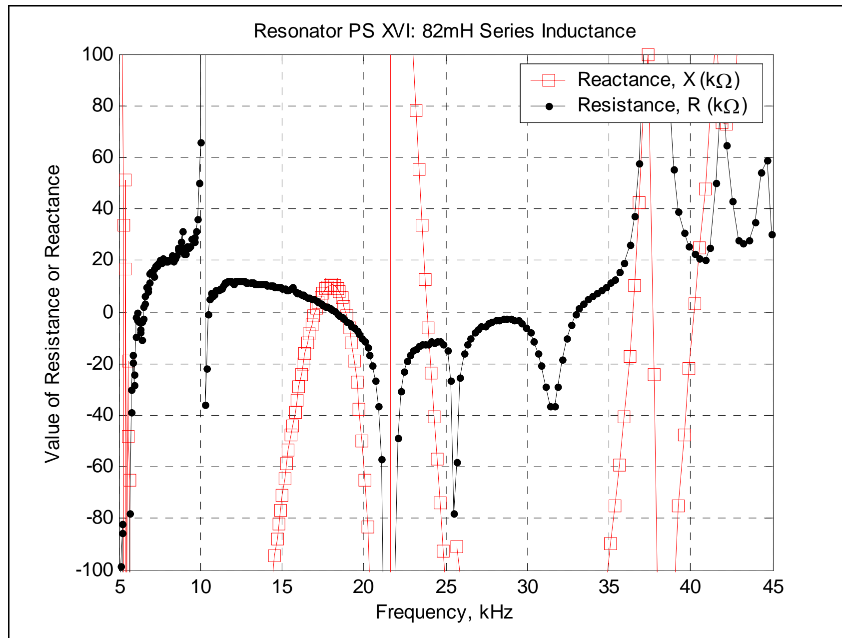

Figure 105. R and X, full range, resonator PS XVI with 82mH series inductor

Figure 101 to Figure 105 show the resistance and reactance of resonator PS XVI from 5kHz to 45kHz with 1mH, 2mH, 4.7mH, 9.4mH and 82mH series inductors. Data for the resonator with 14.1mH series inductance is not shown due to the lack of validity of the values for reactance and resistance obtained from the impedance analyzer. In Figure 101, Figure 102, Figure 103 and Figure 104 the resonator is inductive over the same frequency ranges: approximately 18kHz to 21kHz, 23kHz to 36kHz, and 37 to 40kHz. Over these inductive ranges there are two regions with low resistance magnitudes. These are near 36kHz and 40kHz. The magnitude of the resistance near 36kHz is slightly lower than that at 40kHz – about 1kΩ less - but the resonator does not operate at the lower resistance operating point until the series inductance is at least 9.4mH. Figure 105 shows the resistance and reactance of resonator PS XVI with an 82mH series inductor. The inductive regions are approximately between 17kHz and 19kHz, 21kHz and 24kHz, 36kHz and 37kHz, and above 40kHz. The resistance has the lowest magnitude in the region between 17kHz and 19kHz, which contains the operating point of resonator PS XVI with an 82mH series inductor.

8.4 SUMMARY

The amplifier circuit with the separate gain and phase adjustment was able to drive five out of six of the resonators. Of those five that were successfully driven, two operated at a different mode than was observed with the modified Pierce circuit. When the resonators operated at the same mode using both amplifier schemes, the frequency was always higher when the driver was the amplifier circuit with separate gain and phase adjustment. The differences in frequencies were 60Hz (resonator PS XIV), 250Hz (resonator VIII), and 700Hz (resonator PS XVI).

The resonators were all driven by an inverter in the modified Pierce circuit at frequencies (in most cases) above 30kHz. The reactance at the operational frequencies was always positive. Positive reactance corresponds to a point between a resonance and anti-resonance frequency. With the inverter in the Pierce configuration this is the region in which the resonator is expected to operate. The magnitude of the resistance and reactance at the operational point of the resonators in all cases was below $10\text{k}\Omega$. The operational frequency was also found to be not only in a region of positive reactance but also in the one region that had the lowest overall resistance. The shunt tuning concept was found to be compatible with our modified Pierce amplifier configuration with tuning ranges that were of the same magnitude as that observed through SigLab, the frequency generator-oscilloscope combination (for frequencies above 20kHz) and the other resonator operational configuration.

9.0 CONCLUSIONS AND FUTURE WORK

9.1 CONCLUSIONS

This work investigated tunable piezoelectric resonators. Firstly, the techniques used in the implementation of resonators in general were introduced. The importance of piezoelectricity and piezoelectric materials to the area of resonators was illustrated. The results of a survey of various crystalline and non-crystalline piezoelectric materials were given. The piezoelectric material classes were then introduced and the influence of the piezoelectric strain matrices, by which the materials are classified, on material strain illustrated. Next the characteristics used in measuring the performance of resonators were given. The different resonators were then categorized according to type; then according to resonance mode used. The resonator design used in the work was then introduced and a single degree-of-freedom model developed. The model was developed using the Hamiltonian of the electromechanical system and the bending mode shape functions for a cantilever beam. This analytical model was then used in conjunction with experiment to look at our design from the standpoint of frequency of vibration; tuning; and feedback gain; and implementation. From these four aspects of the design the following conclusions can be drawn:

1. Tuning

The analytical model showed that there would be differences, for a particular electrode pattern, in the tuning range of the various bending modes. This was borne out by the experimental data obtained. Experimental tuning data was obtained from SigLab; the resonator driven by a frequency generator with the response observed on a digital oscilloscope; and from the

observed change in operational frequency in the various implementation configurations employed. The maximum difference between experimental and analytical tuning was, at most, one order of magnitude. Lastly and most importantly, it has been demonstrated that the shunt tuning technique is compatible with classical resonator techniques, in particular, the Pierce circuit configuration.

2. Frequency of Vibration

In general, there was very good agreement between the analytically calculated bending frequency and the frequency of vibration observed in the resonators used in experiment: approximately three quarters of the experimental frequencies of vibration are within 10% of the analytical value. There were resonator-to-resonator differences in the experimentally observed frequency of vibration; attributable to the difficulties encountered in the manufacturing process.

3. Feedback Gain

The analytical model was used to show that the feedback gain is a function of sensor and actuator electrode dimension; and that the function is different for each of the bending modes looked at. Bands of high feedback gain were shown to exist at points where the electromechanical coupling approaches zero. This is an intuitive result since low coupling would mean that the sensor signal would be small; and that the ability of the actuator to drive that particular mode would be low; therefore, the feedback gain would need to be high to overcome the effects of the low coupling. The high feedback gain bands were seen to be a function of the actuator dimension. These results from the analytical model were used in the design process to determine the dimensions of the sensor and actuator.

4. Implementation

Two implementations of the resonator were shown. These implementations were successful to varying degrees. The more successful implementation of the resonator was in the modified

Pierce configuration. In this configuration, using an inverter as the logic gate, all the resonators were driven at the higher bending modes (bending mode 5 and higher). The operational frequency point in the Pierce configuration was found to be determined by the reactance and resistance of the resonator. The operational frequency, in all cases, was in a region of positive reactance where the resonator operates inductively. The frequency of operation was in the inductive region that had the smallest resistance magnitude. Less successful were the implementations using the amplifier which had separate gain and phase adjustment. In all the implementations there was varying success at using the switching technique to change the frequency of vibration. The tuning range in the implementations varied from implementation-to-implementation, resonator-to-resonator, and for the different series inductances applied to a single resonator (Table 15and Table 16). In Table 15 and Table 16, the shaded cells indicate experiments that produced no signal.

Table 15. Comparison of tuning range from Pierce circuit operation and analytical data

Series Inductance (mH)	**Experimental and Analytical Changes in Frequency (Hz)**					
	PS VIII	**PS XII**	**PS XIII**	**PS XIV**	**PS XV**	**PS XVI**
1		91, 97 (16)	0	4 (16)	8	65, 72 (16)
2		90, 103 (16)	-130	-3 (16)	1 (4)	66, 67 (16)
4.7	10-20 (16)	95, 118 (16)		0	0 (4)	56, 57 (16)
9.4	10-70 (16)	152-212, 130 (16)		0	3 (4)	229, 226 (16)
14.1						180, 187 (16)
82	40-130 (43)					27, 18-37 (43)

Table 16. Comparison of tuning range from operation with circuit with separate gain and phase adjustment, and analytical data

	Experimental and Analytical Changes in Frequency (Hz)					
	PS VIII	PS XII	PS XIII	PS XIV	PS XV	PS XVI
Experimental	6-9		1-7	13-16	7-10	1
Analytical	16	N/A	16	16	43	16

9.2 FUTURE WORK

For the tunable piezoelectric resonators to be useful in applications, the variability that was observed in the tuning range and frequency of operation of the resonators needs to be reduced. The variability was identified as being due to the difficulties encountered in the manufacturing process. New manufacturing techniques that would produce resonators that have closer characteristics need to be developed. The problems with the current techniques are two: cutting the materials accurately, and aligning the layers during gluing. At present, only the aluminum substrate is cut with any precision. A method to cut the PZT layer more accurately needs to be developed. Cutting the PZT by hand gave resonators that were adequately similar but higher frequency resonators would, of necessity, need to be dimensionally smaller which would only exacerbate the disparity in the performance of the resonators. In addition, during the gluing phase of manufacturing, a method to align the layers accurately and join them under pressure needs to be formulated. Currently two plexiglass plates, between which the resonator is sandwiched, are forced together using four machine screws tightened by hand. Some movement of the plates relative to each other is inescapable and produces some misalignment of the resonator layers.

The other issue that needs to be addressed is pre-selection of the frequency of operation during the design stage. As has been seen, the resonator in the Pierce configuration operates in a positive reactance region with the smallest resistance magnitude. For pre-selection of the operational frequency to be successful; therefore, we need to be able to manipulate the magnitude of the resistance near the bending mode that has been identified as the frequency of operation of the resonator. The manipulation would involve ensuring that the lowest resistance magnitude while the resonator is inductive is at frequencies near the selected bending mode. Addressing the problems in manufacture and frequency pre-selection will have great influence on maturing the tunable piezoelectric resonator technology.

BIBLIOGRAPHY

1. J. Ahn, S. Jun, D. Kim, G.Y. Yeom, J.B. Yoo, J. Lee and T. Sands, "Fabrication of Piezoelectrically Driven Micro-Cantilever using Pb(ZrTi)O_3 Films", *Proceedings of the 12th IEEE International Symposium on Applications of Ferroelectrics, 2000,* Vol. 2, pp 721-724, 2001.

2. R.A. Bale, J.D. Maines and K.J. Palmer, "Frequency Hopping using SAW Oscillators", *Ultrasonics Symposium Proceedings,* pp 248-250, 1975.

3. S. Ballandras, S. Brasrour, N. Griffaton, J.F. Gelly and F. Lanteri, "Experimental and Theoretical Analysis of Silicon-Based Piezoelectric Transducers for Ultrasound Imaging", *1st Annual International IEEE-EMBS Special Topic Conference on Microtechnologies in Medicine & Biology,* pp 97-100, 2000.

4. A. Baz and J. Ro, "Vibration control of plates with active constrained layer damping", *Smart Materials and Structures*, Vol. 5, No. 3, pp 272-280, 1996.

5. S.P. Beeby, N. Ross and N.M. White, "Thick film PZT/Micromachined Silicon Accelerometer", *Electronics Letters*, Vol. 35, No. 23, pp 2060-2062, 1999.

6. S.P. Beeby and N.M. White, "Thick-film PZT-Silicon Micromechanical Resonator", *Electronics Letters*, Vol. 36, No. 19, pp 1661-1662, 2000.

7. F.P. Beer and E.R. Johnston, Jr., *Mechanics of Materials,* 2nd Edition; McGraw-Hill, Inc., 1992.

8. H. Benaroya, *Mechanical Vibration: Analysis, Uncertainties and Control*, Prentice-Hall, Inc., 1998.

9. J.J. Bernstein, S.L. Finberg, K. Houston, L.C. Niles, H.D. Chen, L.E. Cross, K.K. Li and K. Udayakumar, "Micromachined High Frequency Ferroelectric Sonar Transducers", *IEEE Transactions on Ultrasonics, Ferroelectrics and Frequency Control*, Vol. 44, No. 5, pp 960-969, 1997.

10. A.R. Brown, G.M. Rebiez, "A Varactor-Tuned RF Filter", *IEEE Transactions on Microwave Theory and Techniques*, Vol. 48, No. 7, pp 1157-1160, 2000.

11. I. Browning, J. Crabb and M.F. Lewis, "A SAW Frequency Synthesizer", *Ultrasonics Symposium Proceedings*, pp.245-247, 1975.

12. I. Browning and M.F. Lewis, "Theory of Multimoding in SAW Oscillators", *Ultrasonics Symposium Proceedings,* pp 256-259, 1976.

13. H.D. Chen, K.R. Udayakumar and L.E. Cross, "Development and Electrical Characterization of Lead Zirconate Titanate Thick Films on Silicon Substrates", *Proceedings of the 9th IEEE International Symposium on Applications of Ferroelectrics, 1994*, pp 495-498, 1994.

14. S. Chen, K. A. Zaki and R. G. West, "Tunable, Temperature-Compensated Dielectric Resonators and Filters", *IEEE Transactions on Microwave Theory and Techniques,* Vol. 38, No. 8, pp 1046-1052, 1990.

15. D.L. DeVoe, "Piezoelectric thin film micromechanical beam resonators", *Sensor and Acutators A: Physical,* Vol. 88, pp. 263-272, 2001.

16. A. Dubey, G.S. Tyagi and G.P. Srivastava, "Magnetically Tunable Microstrip Resonator based on Polycrystalline Ferrite", *Electronics Letters*, Vol. 37, No. 21, pp 1296-1297, 2001.

17. M.-A. Dubois, P. Muralt, H. Matsumoto, V. Plessky, "Solidly Mounted Resonator Based on Aluminum Nitride Thin Film", *Proceedings of the IEEE Ultrasonics Symposium, 1998*, Vol. 1, pp. 909- 912, 1998.

18. M.E. Frerking, *Crystal Oscillator Design and Temperature Compensation,* Van Nostrand Reinhold Company, 1978.

19. G. Gautschi, *Piezoelectric Sensorics,* Springer-Verlag, 2002.

20. E.A. Gerber and A. Ballato (eds.), *Precision Frequency Control,* Vols. 1 and 2, Academic Press Inc., 1985.

21. *H.C. Materials Corporation: Piezoelectric Crystal Properties*. Retrieved on the 16th of October 2002 from http://www.hcmat.com/Piezo/Property/pro-table.htm.

22. W. Hackenberger, *Ferroelectric Materials for Actuation and Energy Storage,* TRS Ceramics, Inc. Retrieved on the 5th of November 2002 from, http://www.darpa.mil/dso/thrust/md/Exoskeletons/presentations/mar_01_2000/hackenberger2.pdf.

23. N.W. Hagood, W.H. Chun and A. von Flotow, "Modelling of Piezoelectric Actuator Dynamics for Active Structural Control", *Proceedings AIAA/ASME/ASCE/ASC 31st Structures, Structural Dynamics and Material Conference, AIAA-90-1097-CP*, pp. 2242-2256, 1990.

24. N.W. Hagood and A. von Flotow, "Damping of Structural Vibrations with Piezoelectric Materials and Passive Electrical Networks", *Journal of Sound and Vibration,* Vol. 146, No. 2, pp. 243-268, 1991.

25. E. Hammerstad and O. Jensen, "Accurate Models for Microstrip Computer-aided Design", *IEEE MTT-S International Microwave Symposium Digest*, pp 407-409, 1980.

26. M.J. Hill, R.W. Ziolkowski and J. Papapolymerou, "A High-*Q* Reconfigurable Planar EBG Cavity Resonator", *IEEE Microwave and Wireless Components Letters*, Vol. 11, No. 6, pp 255-257, 2001.

27. M. Hoffmann, H. Kuppers, T. Schnelller, U. Bottger, U. Schnakenberg, W. Mokwa and R. Waser, "A New Concept and First Development Results of a PZT Thin Film Actuator", *Proceedings of the 12th IEEE International Symposium on Applications of Ferroelectrics, 2000,* Vol. 1, pp 519-524, 2001.

28. IEEE Std 176-1987, *IEEE Standard on Piezoelectricity*, The Institute of Electrical and Electronics Engineers, 1987.

29. W.S. Ishak, K. Chang, W.E. Kunz and G. Miccoli, "Tunable Microwave Resonators and Oscillators Using Magnetostatic Waves", *IEEE Transactions on Ultrasonics, Ferroelectrics and Frequency Control*, Vol. 35, No. 3, pp 396-405, 1988.

30. W.E. Kingery, E. Lense (eds), *Ceramics and Civilization, Vol. III: High-Technology Ceramics – Past, Present and Future,* American Ceramic Society, Inc., 1987

31. M. Koch, N. Harris, A.G.R. Evans, N.M. White and A. Brunnschweiler, "Screen Printing of Thick Piezoelectric PZT Layers onto Silicon Micromachined Membranes", *IEEE Colloquium Recent Advances in Micromachining Techniques*, Digest No. 1997/081, pp 2/1-2/3, 1997.

32. M. Koch, N. Harris, A.G.R. Evans, N.M. White and A. Brunnschweiler, "A Novel Micromachined Pump based on Thick-Film Piezoelectric Actuation", *International Conference on Solid-State Sensors and Actuators, Transducers '97*, pp 353-356, 1997.

33. S.S. Lee and R.M. White, "Self-Excited Piezoelectric Cantilever Oscillators", *8th International Conference on Solid-State Sensors and Actuators, and Eurosensors IX*, Vol. 1, pp 417-420, 1995.

34. A. Mahdi, A. Khanifar and D.P. Howson, “Digital Switching of Mobile Radio Transmitter Cavity Resonators”, *Microwaves, Antennas and Propagation, IEE Proceedings H*, Vol. 137, No. 5, pp 321-324, 1990.

35. W.P. Mason and R.N. Thurston (eds.), *Physical Acoustics,* Vol. XIII, pp 115-181, Academic Press, 1977.

36. MIL-PRF-3098H. *Performance Specification: Crystal Units, Quartz, General Specifications for,* 1997.

37. F.A. Miranda, G. Subramanyam, F.W. Van Keuls, R.R. Romanofsky, J.D. Warner and C.H. Mueller, “Design and Development of Ferroelectric Tunable Microwave Components for *Ku*- and *K*-Band Satellite Communication Systems”, *IEEE Transactions on Microwave Theory and Techniques*, Vol. 48, No. 7, pp 1181-1189, 2000.

38. P. Muralt, D. Schmitt, N. Ledermann, J. Baborowski, P.K. Weber, W. Steichen, S. Petitgrand, A. Bosseboeuf, N. Setter and P. Gaucher, “Study of PZT Coated Membrane Structures for Micromachined Ultrasonic Transducers”, *2001 IEEE Ultrasonics Symposium*, Vol. 2, pp 907-911, 2001.

39. C.T.-C. Nguyen, “Frequency-Selective MEMS for Miniaturized Low-Power Communication Devices”, *IEEE Transactions on Microwave Theory and Techniques*, Vol. 47, No. 8, pp 1486-1503, 1999.

40. D.E. Oates and G.F. Dionne, “Magnetically Tunable Superconducting Resonators and Filters”, *IEEE Transactions on Applied Superconductivity*, Vol. 9, No. 2, pp 4170-4175, 1999.

41. T.E. Parker and J.P. Sage, “A SAW Oscillator using Two Acoustic Paths”, *Ultrasonics Symposium Proceedings,* pp 243-247, 1976.

42. B. Parzen, A. Ballato, *Design of Crystal and Other Harmonic Oscillators*, J. Wiley & Sons, Inc., 1983.

43. P.K. Petrov and N. M. Alford, “Tunable Dielectric Resonator with Ferroelectric Element”, *Electronics Letters*, Vol. 37, No. 17, pp 1066-1067, 2001.

44. B. Piekarski, D. DeVoe, M. Dubey, R. Kaul and J. Conrad, “Surface micromachined piezoelectric resonant beam filters, *Sensors and Actuators A: Physical*, Vol. 91, pp 313-320, 2001.

45. Y.M. Poplavko, Y.V. Prokopenko, V.I. Molchanov and A. Dogan, "Frequency-Tunable Microwave Dielectric Resonator", *IEEE Transactions on Microwave Theory and Techniques*, Vol. 49, No. 6, pp 1020-1026, 2001.

46. G.A. Racine, P. Muralt and M.A. Dubois, "Flexural-standing-wave elastic force motor using ZnO and PZT thin film on Micromachined silicon membranes for wristwatch applications", *Smart Materials and Structures*, Vol. 7, No. 3, pp 404-416, 1998.

47. S.S. Rao, *Mechanical Vibrations,* 2nd Edition; Addison-Wesley, 1990.

48. C.Z. Rosen, B. V. Hiremath and R. Newnham (eds.), *Piezoelectricity,* American Institute of Physics, 1992.

49. B. Satish, K. Sridevi and M.S. Vijaya, "Study of piezoelectric and dielectric properties of ferroelectric PZT-polymer composites prepared by hot-press technique", *Journal of Physics D: Applied Physics*, Vol. 35, No. 16, pp 2048-2050, 2002.

50. C.B. Saw, P.M. Smith, P.J. Edmonson and C.K. Campbell, "Mode Selection in a Multimode SAW Oscillator using FM Chirp Mixing Signal Injection", *IEEE Transactions on Ultrasonics, Ferroelectrics, and Frequency Control*, Vol. 35, No. 3, pp 390-395, 1988.

51. R.C. Smythe, R. C. Helmbold, G.E. Hague and K. A. Snow, "Langasite, Langanite, and Langatate Bulk-Wave Y-Cut Resonators", *IEEE Transactions on Ultrasonics, Ferroelectric,s and Frequency Control,* Vol. 47, No. 2, pp 355-360, 2000.

52. Q. Su, P. Kirby, E. Komuro, M. Imura, Q. Zhang and R. Whatmore, "Thin-Film Bulk Acoustic Resonators and Filters Using ZnO and Lead-Zirconium-Titanate Thin Films", *IEEE Transactions on Microwave Theory and Techniques,* Vo. 49, No. 4, pp 769-778, 2001.

53. W.C. Tang, T-C. H. Nguyen and R.T. Howe, "Laterally Driven Polysilicon Resonant Microstructures", *IEEE Proceedings on Micro Electro Mechanical Systems, 'An Investigation of Micro Structures, Sensors, Actuators, Machines and Robots'*, pp 53-59, 1989.

54. E. Venkatragavaraj, B. Satish, P.R. Vinod and M. S. Vijaya, "Piezoelectric properties of ferroelectric PZT-polymer composites", *Journal of Physics D: Applied Physics*, Vol. 34, No. 4, pp 487-492, 2001.

55. J.R. Vig, "Quartz Crystal Resonators and Oscillators for Frequency Control and Timing Applications: A Tutorial", Rev. 8.5.1.2, AD-M0001251, 2001.

56. F.J. von Preissig, H. Zeng, E.S. Kim, "Measurement of piezoelectric strength of ZnO thin films for MEMS applications", *Smart Materials and Structures*, Vol. 7, No. 3, pp. 396-403, 1998.

57. H. Xu, E. Gao and Q.Y. Ma, "Active Tuning of High Frequency Resonators and Filters", *IEEE Transactions on Applied Superconductivity*, Vol. 11, No. 1, pp 353-356, 2001.

58. M. Yamaguchi, K. Hashimoto, R. Nanjo, N. Hanazawa, S. Ttsutsumi and T. Yonezawa, "Ultrasonic Properties of PZT Thin Films in UHF-SHF Ranges Prepared by Sol Gel Method", *IEEE International Frequency Control Symposium*, pp 544-551, 1997.

59. J.H. Yoo, S.M. Hwang, H.S. Yoon, H.S. Jeong, J.S. Kim and C.S. Yoo, "Piezoelectric Properties of PNW-PMN-PZT Ceramics for High Power Piezoelectric Transformer", *Proceedings of the IEEE Symposium on Applications of Ferroelectrics, 2000*, Vol. 1, pp 495-498, 2001.

60. J. Yoon and C.T.-C. Nguyen, "A High-Q Tunable Micromechanical Capacitor with Movable Dielectric for RF Applications", *International Electron Devices Meeting Technical Digest*, pp 489-492, 2000.

61. T. Yun, K. Chang and R.S. Tahim, "A Wideband Voltage-Tunable Dielectric Resonator Oscillator Controlled by a Piezoelectric Transducer", *Microwave Symposium Digest, IEEE MTT-S International*, Vol. 3, pp 1435-1437, 2001.